QUANTIFICATION OF GREENHOUSE GAS EMISSION RATES FOR POINT SOURCES AND CITIES VIA AIRBORNE MEASUREMENTS

A Dissertation

Submitted to the Faculty

of

Purdue University

by

Kristian D. Hajny

In Partial Fulfillment of the

Requirements for the Degree

of

Doctor of Philosophy

December 2020

Purdue University

West Lafayette, Indiana

THE PURDUE UNIVERSITY GRADUATE SCHOOL
STATEMENT OF DISSERTATION APPROVAL

Dr. Paul B. Shepson, Co-Chair

Department of Chemistry

Department of Earth, Atmospheric, and Planetary Sciences

Stonybrook University School of Marine and Atmospheric Sciences

Dr. Gregory Michalski, Co-Chair

Department of Earth, Atmospheric, and Planetary Sciences

Dr. Scott McLuckey

Department of Chemistry

Dr. Alexander Laskin

Department of Chemistry

Approved by:

Dr. Christine A. Hrycyna

Head of the Graduate Program

ACKNOWLEDGMENTS

I would like to thank the friends and coworkers at Purdue and beyond who have helped make my work possible. I am grateful to my Ph.D. advisor Dr. Paul Shepson for his mentorship and significant involvement in my development as a scientist and in my career. I would also like to thank Cody Floerchinger from Harvard University, a colleague and friend who helped make my year as a visiting scholar at Harvard and the research I did while there possible along with continuous support throughout my research. I would similarly like to thank Dr. Wofsy from Harvard for allowing me to join his research group and welcomed and supported me during my stay.

The Shepson Research Group, past and present, at Purdue also deserves significant thanks for their support both scientific and personal. Particularly, Dr. Olivia Salmon and Dr. Tegan Lavoie who mentored me in data analysis and flying as a mission scientist in the research aircraft and continued to support me in my research as it progressed. I would also like to thank Brian Stirm for his significant efforts in maintaining the research aircraft. The Jonathan Amy Facility for Chemical Instrumentation's Jim Zimmerman, Mark Carlsen, and Phil Wyss have also devoted large amounts of time to support us in maintaining and troubleshooting the instrumentation aboard the aircraft. I am also thankful to our pilots, particularly Robert (Bob) Kaeser and Andy Armstrong who have flown the majority of my research flights and my first campaign respectively, for their consistent expertise as fantastic pilots even in unfavorable conditions and unconventional flight plans. Similarly, I would like to thank the many Air Traffic Control operators that have supported us and allowed us to continue our complex flight plans safely while managing the often busy commercial traffic.

I am thankful for the financial support that I have received from the National Institute of Standards and Technology, and Environmental Defense Fund. I am also appreciative of the mentoring that both organizations have provided me throughout my research, specifically Israel Lopez-Coto and Anna Karion of the National Institute of Standards and Technology and Joseph Rudek and David Lyon of the Environmental Defense Fund.

In closing I would like to acknowledge my family and friends for their continuous faith in my abilities and acceptance of the time and effort needed for me to accomplish reaching this goal.

TABLE OF CONTENTS

Page

LIST OF TABLES

LIST OF FIGURES

Figure Page

Figure Page

Figure Page

Figure Page

Figure Page

Figure Page

ABSTRACT

Hajny, Kristian D. Ph.D., Purdue University, December 2020. Quantification of Greenhouse Gas Emission Rates for Point Sources and Cities via Airborne Measurements. Major Professors: Paul B. Shepson, Gregory Michalski.

Urban greenhouse gas emissions and urbanization are both expected to continue to increase in coming years. Accordingly, many cities have passed legislation or set goals for specific greenhouse gas reductions. However, high precision monitoring techniques are necessary to act on this legislation and to quantify the impact of effective mitigation strategies. Here we use the airborne mass balance technique to address this need.

Chapter 3 focuses on 23 flights at 14 natural gas-fired power plants (NGPPs) using an aircraft-based mass balance technique and methane/carbon dioxide enhancement ratios ($\Delta CH_4/\Delta CO_2$) measured from stack plumes to quantify the unburned fuel. Current research efforts on the atmospheric impacts of natural gas (NG) have focused heavily on the production, storage/transmission, and processing sectors, with less attention paid to the distribution and end use sectors. By comparing the $\Delta CH_4/\Delta CO_2$ ratio measured in stack plumes to that measured downwind, we determined that, within uncertainty of the measurement, all observed CH_4 emissions were stack-based, that is, uncombusted NG from the stack rather than fugitive sources. Measured CH_4 emission rates (ER) ranged from 8 ($\pm$ 5) to 135 ($\pm$ 27) kg CH_4/h ($\pm$ 1σ), with the fractional CH_4 throughput lost (loss rate) ranging from -0.039% ($\pm$0.076%) to 0.204% ($\pm$0.054%). We attribute negative values to partial combustion of ambient CH_4 in the power plant. The average calculated emission factor (EF) of 5.4 (+10/-5.4) g CH_4/million British thermal units (MMBTU) is within uncertainty of the En-

vironmental Protection Agency (EPA) EFs. However, one facility measured during startup exhibited substantially larger stack emissions with an EF of 440 (+660/-440) g CH_4/MMBTU and a loss rate of 2.5% (+3.8/-2.5%).

Chapter 4 uses a slightly larger set of power plant flights, including most of those in Chapter 3, to assess the airborne mass balance technique. GHG quantification techniques must be highly precise to effectively monitor changes in GHG emissions to inform effective mitigation strategies and act on already existing goals and legislation towards reductions. Power plants are required to measure their CO_2 emissions using continuous emissions monitoring systems (CEMS), providing an effective "known" emission rate to compare against those measured downwind using the airborne mass balance approach. The mean absolute error between measured and CEMS emission rates was calculated as 20% $\pm$ 13 and the slope of measured emission rates against CEMS emission rates was 0.871 $\pm$ 0.033. Additionally, power plants generally have consistent production/emission profiles through the typical midday hours of the experiments. This allows us to consider back to back experiments at the same facility as replicate experiments to assess the precision of the mass balance technique too. Across the campaign, the average relative standard deviation (1σ/mean) was 25% $\pm$ 16.

Chapter 5 focuses on measurements of greenhouse gases around New York City with 7 non-growing season research aircraft flights in 2018-2020 and used dispersion modelling to estimate CO_2 emissions from New York City with a simple scaling factor approach. Cities are leading efforts to reduce greenhouse gas emissions. New York City has passed a suite of legislation outlining aggressive reduction targets, which has been supplemented by similar legislation covering New York State. However, appropriate techniques to quantify emission reductions over time are necessary to monitor the progress of such legislation and effectively inform continuing mitigation efforts. The average calculated CO_2 emission rate for New York City, representative of afternoons in the non-growing season, was 67 kmol/s. By using a variety of priors, calculation methods, and meteorology products we also investigate the variability of

the estimation introduced by each of these sources. Variability across flight days proved to be larger than the combined variability of all other sources, as seen in previous works. This work uses a pre-COVID dataset to introduce a scaling factor approach that can account for and isolate multiple sources of variability and that can be used for long term emission trend analyses, including analyses of emissions during and after shut-down conditions.

1. INTRODUCTION

1.1 Atmosphere Structure

The atmosphere is divided into the troposphere, stratosphere, mesosphere, thermosphere, and ionosphere in ascending altitude order. The troposphere is the ∼10 km layer in direct contact with the surface making it the most heavily-impacted by surface emissions and accordingly, the focus of this work. As it is heavily influenced by incoming solar radiation ("insolation"), at the surface, the troposphere's structure also shows a strong diurnal cycle as shown in Figure 1.1. This also shows that the troposphere can be subdivided into the surface layer, a convective boundary layer (CBL) that is topped with an entrainment layer, and the free troposphere. During the day the sun heats the surface warming the air in direct contact with the surface, which causes it to expand, become less dense, and thus rise. As this warm air rises it displaces denser air parcels downward to replace it in circular motions called eddies. This buoyant circulation of air keeps the CBL generally well mixed. This diurnal cycle in mixing has a significant impact on the diurnal cycle of the concentration of gases emitted at the surface. The CBL grows during the early morning after sunrise as warm air climbs above the entrainment layer and mixes free tropospheric air into the CBL in a process called entrainment [1]. At night mechanical turbulence typically dominates over convective mixing. Mechanical turbulence creates eddies via wind flow over surface features and from wind-shear from air flow in different wind directions between vertically neighboring air parcels. With less vertical motion, the boundary layer settles into a stable residual layer, where air from the previous day's boundary layer remains with little turbulence, since it is disconnected from mechanical mixing

near the surface, and a nocturnal boundary layer that is typically much shallower. Because the solid surface cools faster than the air above it, the surface layer often exhibits a temperature inversion, with the coolest air at the surface, greatly inhibiting mixing. Such inversion layers have created notorious pollution events, e.g. the event in Donora, PA, in 1948 [2]. With rougher surfaces, relatively high winds, and/or lower insolation (e.g. heavy cloud cover) mechanical turbulence can be an important driver of mixing during the day as well [1].

The top of the CBL is capped by an entrainment zone where water vapor condenses into water droplets releasing heat into the surrounding air and causing a temperature inversion. This release of heat due to a phase change (i.e., without a change in temperature for the material itself, in this case H_2O) is defined as latent heat [1]. Having warm air (less dense) above cold air (more dense) is stable, so it will not readily mix. Figure 1.2 is an airborne photo that shows the CBL height in a real-world scenario. Lastly the surface layer is defined as the lowest 10% of the CBL which is most heavily influenced by surface roughness.

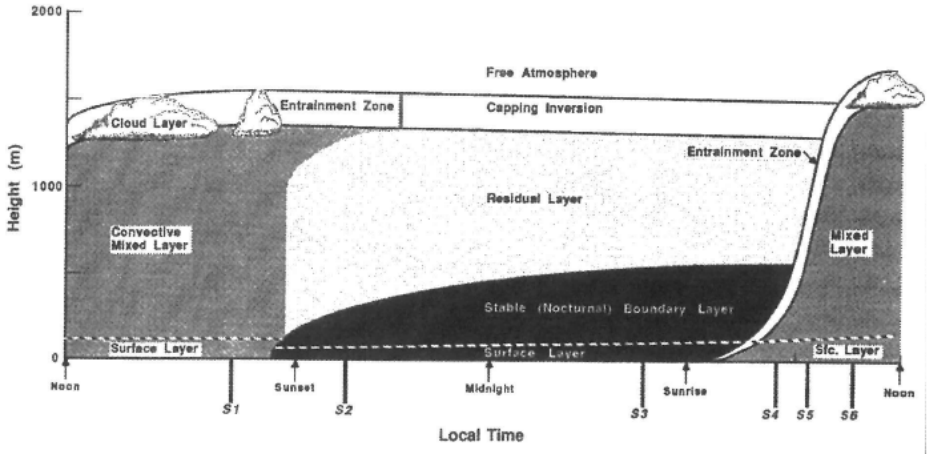

Figure 1.1. Idealized depiction of layering in the troposphere, figure from Stull [1].

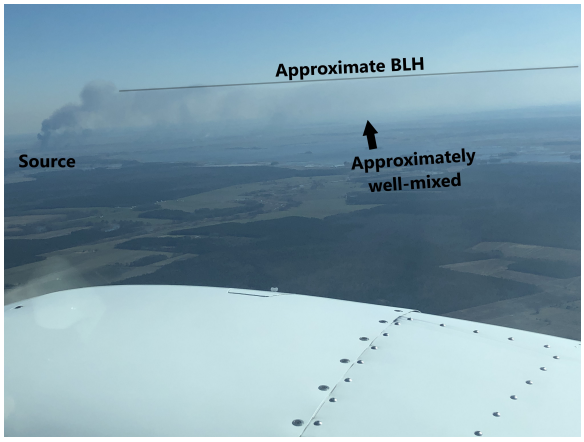

Figure 1.2. An airborne photo of a small brush fire releasing black smoke that provides a visualization of the CBL. The hot, buoyant smoke rises quickly, seeming to penetrate slightly above the CBL, before slowly mixing within the CBL, providing a clear visual of the BLH (marked) and becoming ∼well-mixed in the vertical further downwind.

The CBL can vary between a few hundred meters to a few kilometers depending on the conditions. Generally, warm weather and high winds lead to significant buoyant turbulence that help create a larger boundary layer. Given the depth of the CBL defines the volume that surface emissions are able to mix into, it is important to know the boundary layer height (BLH), or the altitude of the top of the CBL. Given the CBL is capped by a temperature inversion, one of the clearest ways to identify it is by identifying the altitude of this inversion. Potential temperature, the temperature corrected for the impact of adiabatic expansion as the pressure decreases with altitude, is typically used for this purpose. It is calculated as shown in Equation 1.1.

$$\theta = T \times \left(\frac{1000}{P}\right)^{\frac{R}{C_p}} \tag{1.1}$$

Here θ represents potential temperature (K), T is temperature (K), P is pressure (mbar), 1000 is a reference pressure (mbar), R is the gas constant (287.04 J $K^{-1}kg^{-1}$) and C_p is the specific heat capacity of air at constant pressure (1004.67 J $K^{-1}kg^{-1}$). Concentrations of species emitted from the surface (particles, CO_2, CH_4, etc.) also

change sharply at the BLH as the CBL is much more heavily influenced by surface emissions. Figure 1.3 shows idealized vertical profiles in the CBL.

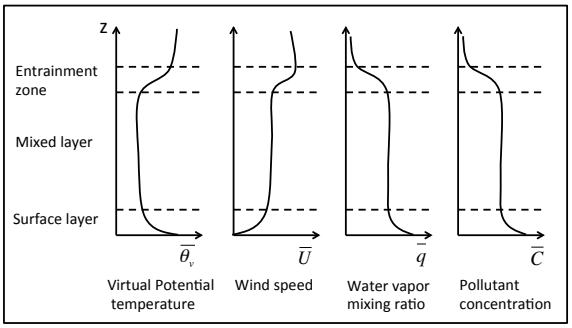

Figure 1.3. Idealized vertical profiles in the CBL for selected variables. Figure adapted from Stull [1]

1.2 Climate Change

The atmosphere provides a very important cleaning function, contributing to a habitable Earth. It does so by oxidizing water-insoluble, often toxic, gases to water soluble products that can then be removed via rain. This happens largely involving oxidation by the hydroxyl radical, OH. OH is produced as shown below [3]. It oxidizes species such as SO_2 and NO to H_2SO_4 and HNO_3, as shown in reactions 1-7 below. However, some gases, such as N_2O, CF_2CL_2, CH_4, and CO_2 react only very slowly, if at all, with OH, and also not at all with the other important oxidants, O_3 and NO_3. Since the concentration of a gas in the atmosphere is proportional to its emission rate divided by its removal rate, the concentration of these gases have been increasing throughout the atmosphere.

1. $O_3 + h\nu \rightarrow O(^1D) + O_2$
2. $O(^1D) + H_2O \rightarrow 2OH$
3. $OH + SO2 \rightarrow HSO_3$

4. $HSO_3 + O_2 \rightarrow H_2SO_4 + HO_2$

5. $O_3 + NO \rightarrow NO_2 + O_2$

6. $OH + NO_2 \rightarrow HNO_3$

Climate change is defined as a change in the average weather conditions (e.g. rainfall, temperature, etc.) or their variability for an extended period. The United Nations Framework Convention on Climate Change (UNFCCC) adds that it is only changes due to human impact (anthropogenic) rather than natural variability [4, 5]. Anthropogenic climate change is due to the emission of greenhouse gases (GHG) that contribute to an increased greenhouse effect and warming, which has been partially offset by emissions of aerosols and their precursors which generally lead to increased reflectivity and cooling as described in Figure 1.4.

GHGs are gases that absorb infrared (IR) radiation but do not absorb ultraviolet or visible (UV-vis) radiation, allowing them to absorb the IR emitted from the Earth's surface and then re-emit it omnidirectionally. This then causes a net increase in the radiative flux at the surface, from the component of the re-radiation that is downward, as summarized quantitatively in Figure 1.4, with the complete radiation budget of the planet shown in Figure 1.5. The greenhouse effect is the increase in temperature caused by GHGs absorbing the infrared radiation (IR) emitted by the Earth and re-radiating it omnidirectionally, resulting in a net increase in radiative flux at the surface due to the component of re-radiation that is downward. This is summarized quantitatively in Figure 1.4. Earths equilibrium temperature in the absence of the greenhouse effect can be estimated by assuming the Earth emits as a black body according to Equation 1.2.

$$S = \sigma T_e^4 \tag{1.2}$$

Here S is the amount of absorbed solar radiation, or the irradiance of a black body, σ is the Stefan-Boltzmann constant, and T_e is the equilibrium temperature. The Earth

absorbs about 240 W/m^2 averaged over the surface and all seasons, resulting in a T_e of about 255 K or -18°C [6]. As the global mean surface temperature is 288 K, the greenhouse effect is responsible for about 33 K of surface warming.

Global warming due to an increasing greenhouse effect was first suggested by Arrhenius as summarized in Rodhe et al. [8], based solely on changing CO_2 concentrations. There is now significant evidence across multiple lines of data, as shown in Figure 1.6, that the global temperature is rising. However, this warming is occurring primarily in the oceans, with the land and atmosphere seeing only a small fraction of the total heating caused by the enhanced greenhouse effect as quantitatively shown in Figure 1.7 [9]. GHGs are gases that absorb infrared (IR) radiation but do not absorb ultraviolet or visible (UV-vis) radiation, allowing them to absorb the IR emitted from the Earth's surface and then re-emit it resulting in a net increase in the radiative flux at the surface. If the downward irradiance increases, the surface must re-radiate more IR radiation upward, to achieve a radiation balance. According to Equation 1.2, it does so at a higher temperature. The GHGs are all transparent to the downward UV and visible radiation from the sun, but all effectively absorb the outgoing black body IR radiation from the Earth, as shown in Figure 1.8. It is important to note that, based on satellite observations, changes in the incoming solar radiation are known to be quantitatively insignificant. In fact, the combination of all natural variations in the Earth's climate system, including variability in incoming solar radiation, large-scale climate phenomena such as El-Niño/La Niña, and volcanic eruptions (e.g. the 1991 Mt. Pinatubo eruption, which injected 5 km^3 of ash up to 35 km high, into the stratosphere [10]) to name a few, cannot explain the current trends in temperature with current models. As shown using an ensemble of model runs using the Coupled Model Intercomparison Project Phase 5 (CMIP5) inf Figure 1.9, the modeled temperature variations only match modeled results when incorporating the human-induced changes to GHGs and aerosols [7].

The primary GHGs are H_2O, CO_2, CH_4, O_3, N_2O and halocarbons (CFCs, HCFCs, etc.). The concentrations of these "radiatively active" gases are increasing due to hu-

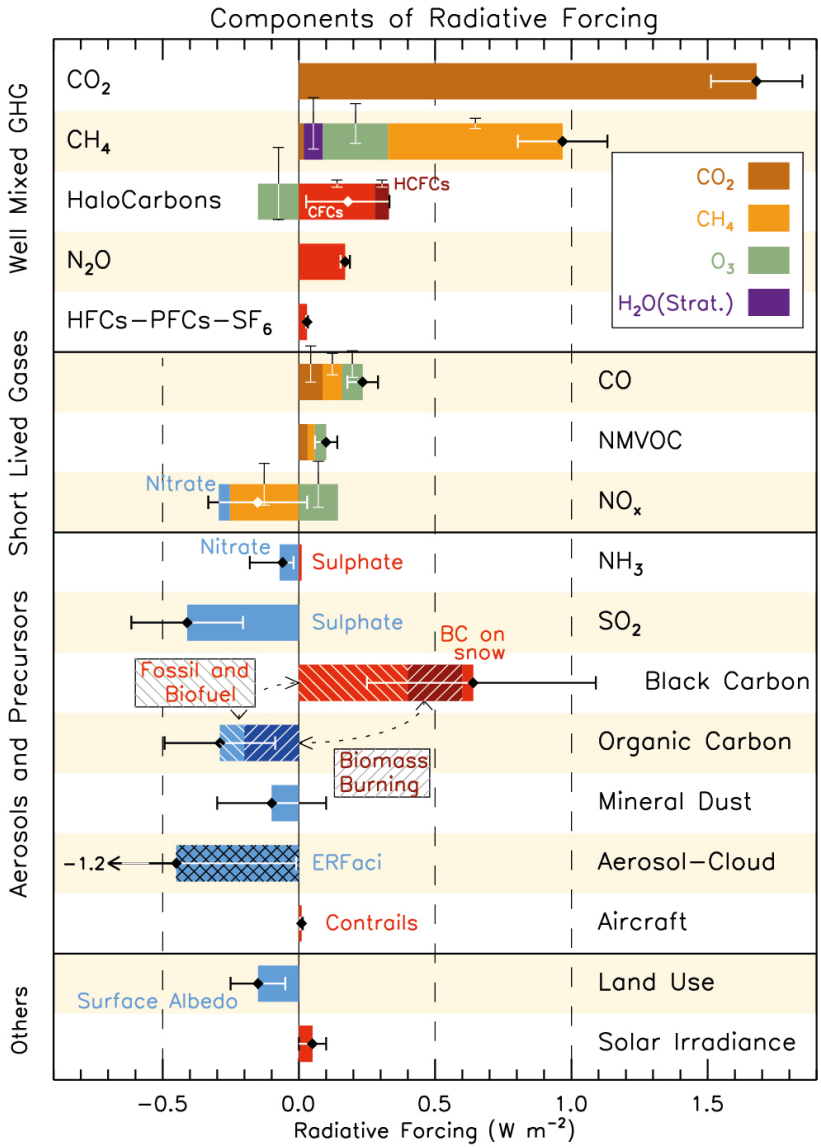

Figure 1.4. RF bar chart based on emitted gas/process for 1750-2011. Red (positive) and blue (negative) are used for components which affect few forcing agents, the inset indicates colors for those impacting several. Vertical bars indicate the relative uncertainty of each component where the length is proportional to the thickness of the bar i.e., a length equal to the bar thickness is equal to a $\pm 50\%$ uncertainty. Net impacts are shown by diamond symbols with 95% confidence intervals given by the horizontal bars. ERFaci is ERF from aerosol-cloud interactions. Secondary organic Aerosol are excluded due to insufficient information. Figure 8.17 from IPCC Fifth Assessment Report: The Physical Science Basis [7]

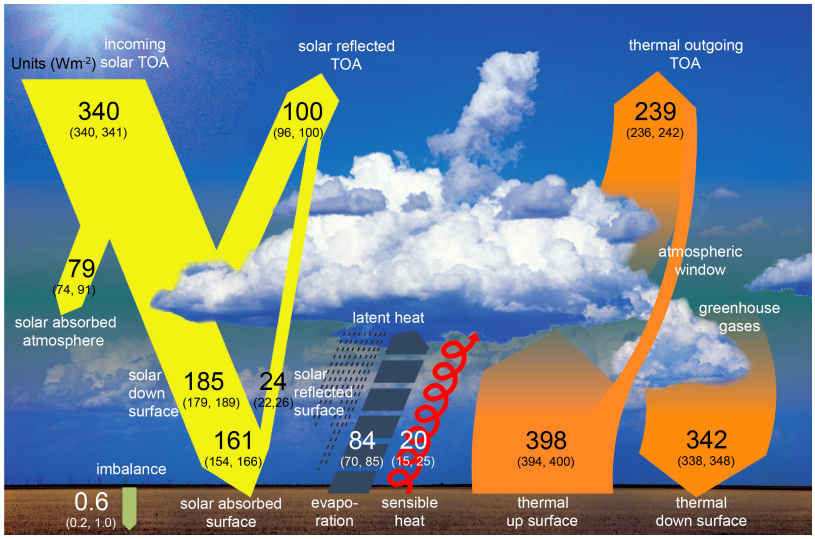

Figure 1.5. Global mean energy budget under present-day climate conditions. Numbers represent individual energy fluxes in Wm^{-2} adjusted within their uncertainty ranges to balance the energy budget. Numbers in parentheses cover the range of values within observational constraints. Sensible heat is any heat transfer that results in direct temperature changes, as opposed to latent heat. Figure 2.11 from IPCC Fifth Assessment Report: The Physical Science Basis [7].

man activities. Table 1.1 describes the current atmospheric concentrations and global warming potentials (GWP) of a selection of these gases. The GWP of a gas is defined as the increased RF induced by a pulse emission of the species relative to the RF of the same mass of CO_2. Radiative forcing is externally imposed perturbations in the radiative energy budget of the Earth's climate system (due to changes in the concentrations of radiatively active species, changes in the incoming solar radiation, etc.). These perturbations introduce an imbalance in the radiation budget, which has the potential to lead to changes in climate parameters and thus result in a new equilibrium state of the climate system. Figure 1.10 shows the increasing concentration over time for the three most important GHGs (based on GWP and abundance), and Figure 1.11 shows the increasing radiative forcing (RF) of these gases over time.

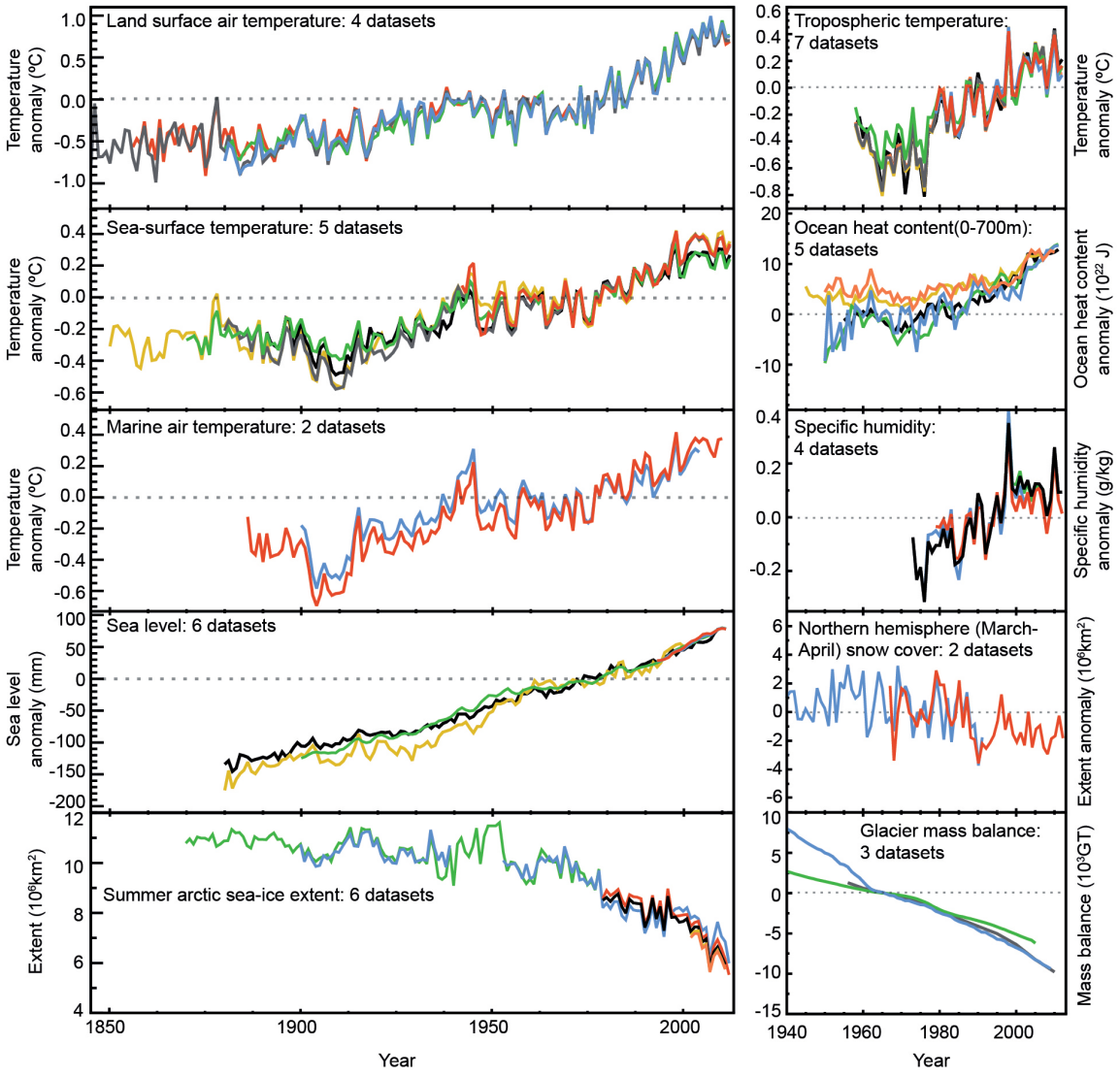

Figure 1.6. Various independent indicators of a changing global climate where each line represents an independently derived estimate of change. Figure 2 from FAQ 2.1 in the IPCC Fifth Assessment Report: The Physical Science Basis [7].

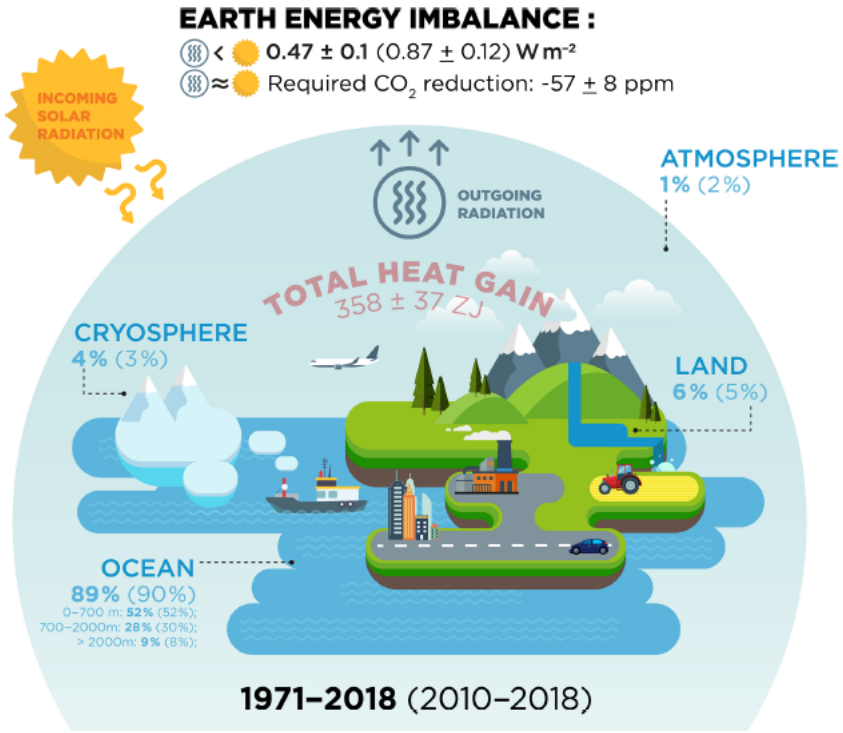

Figure 1.7. Schematic of the Earth heat inventory for the current anthropogenically driven imbalance at the top of the atmosphere. Percentage values describe the amount of heat partitioned to each component with values representing 1971-2018 and parenthetical values representing 2010-2018. The total heat gain is provided in red. The imbalance for both time periods and the CO_2 reductions required to reduce the energy imbalance to $\sim$0 (based on the 2010-2018 value of 0.87 W/m^2) are listed at the top. Figure from Shuckmann et al. [9]

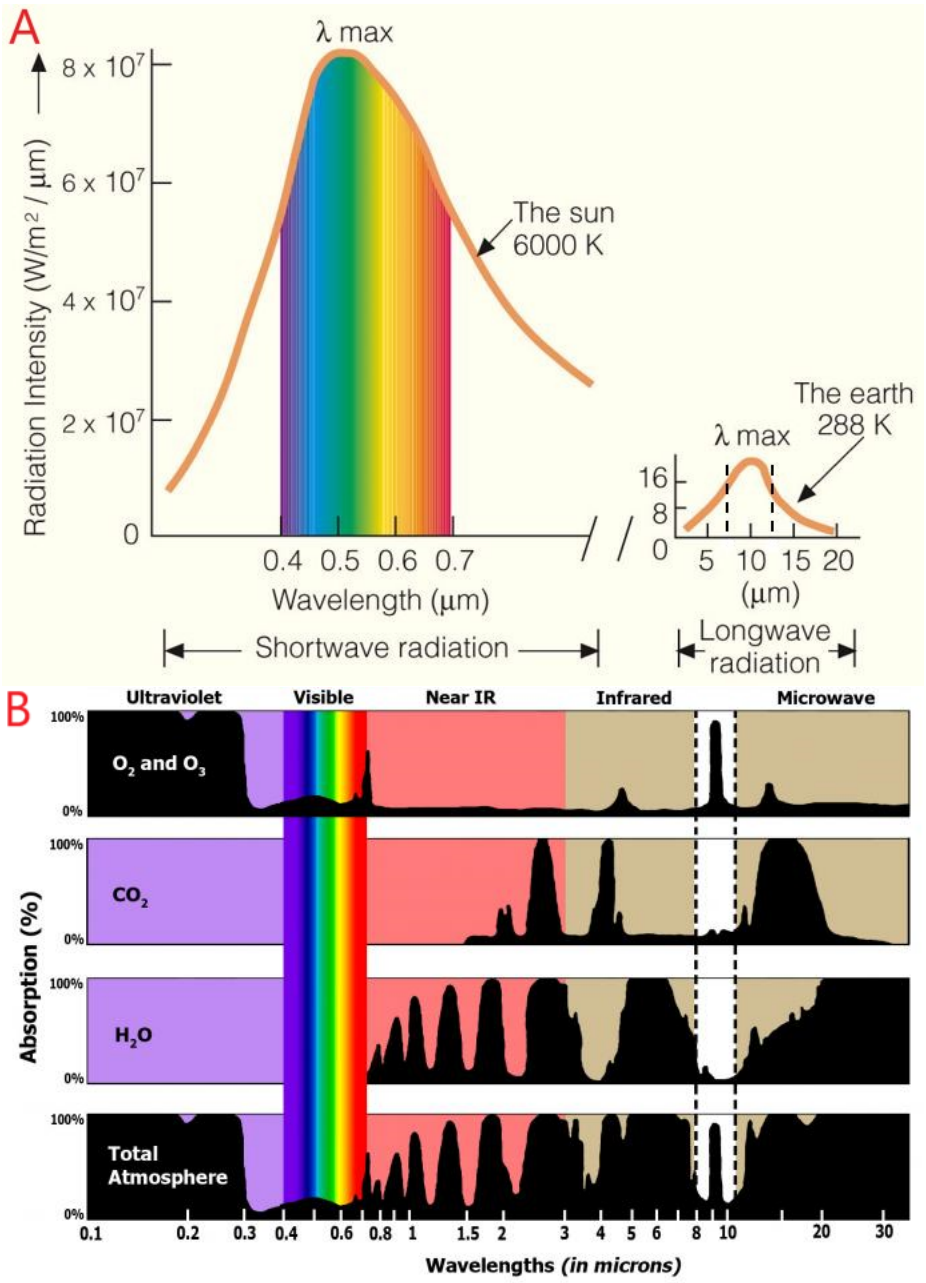

Figure 1.8. A) Emissions from both the sun and the Earth's surface, note the significantly different axes between the two. B) The absorption spectrum across the total atmosphere and that of certain important greenhouse gases. Figures from The Essentials of Meteorology [11] and `http://www.ces.fau.edu/nasa` [12].

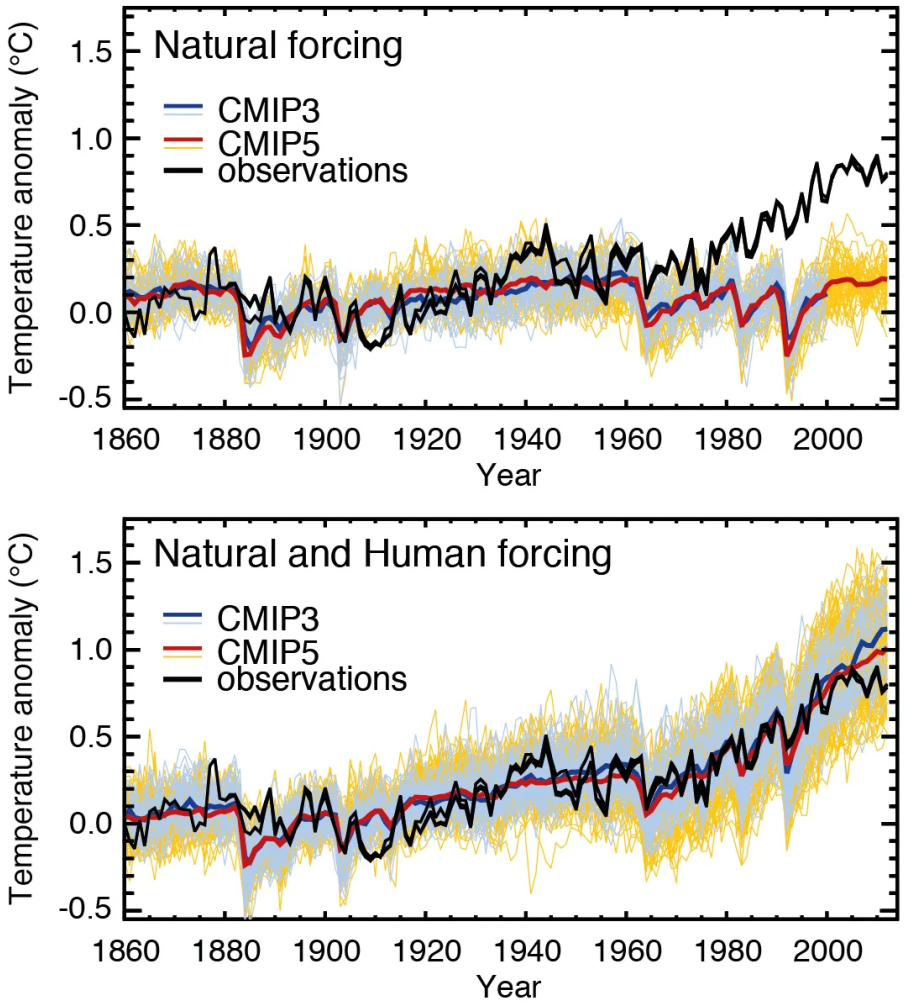

Figure 1.9. Time series of global, annually-averaged surface temperature change. The top panel shows results using only natural forcing while the bottom shows simulations from the same models, but driven with both natural forcing and human-induced changes in GHGs and aerosols. Thin blue and yellow lines represent the large ensemble of climate models run and the ensemble averages are shown as thick blue and red lines. Adapted from FAQ 10.1 from IPCC Fifth Assessment Report: The Physical Science Basis [7].

Although H_2O is the most significant GHG given its atmospheric concentration and absorption spectrum, it is typically not considered when discussing anthropogenic climate change as its atmospheric concentration is governed primarily by positive feed-

backs related to warming of the land and ocean surfaces (evaporation, condensation, and rain) [6, 7]. Stratospheric H_2O, however, is heavily influenced by anthropogenic emissions through increased atmospheric concentrations of CH_4, which has a long enough atmospheric lifetime to mix to the stratosphere, and which produces H_2O as it oxidizes to CO_2 [7]. Positive climate feedbacks are natural processes that reinforce a change (e.g. increased atmospheric H_2O due to increasing temperature and evaporation leads to further warming) and negative climate feedbacks are natural processes that return a system to an equilibrium (e.g. increased cloud cover due to increased temperature and atmospheric H_2O results in greater surface albedo, and thus more solar radiation being reflected away from the surface, leading to cooling).

Table 1.1.
2011 atmospheric concentrations and GWPs of select GHGs. Adapted from Tables 8.A.1 and 8.2 from IPCC Fifth Assessment Report: The Physical Science Basis [7]

Acronym/Name	Chemical Formula	Lifetime (Years)	Concentration (%)	GWP (20-year)	GWP (100-year)
Carbon dioxide	CO_2	see[a]	3.91E-2	1	1
Methane	CH_4	12.4	1.803E-4	84	28
Nitrous oxide	N_2O	121	3.24E-5	264	265
Carbon tetrachloride	$CHCl_4$	0.4	8.58E-9	60	16
CFC-113	CCl_2FCClF_2	85	7.43E-9	6,490	5,820
HCFC-22	$CHClF_2$	11.9	2.13E-8	5,280	1,760
HFC-125	CHF_2CF_3	28.2	9.58E-10	6,090	3,170
Sulphur hexafluoride	SF_6	3,200	7.28E-10	17,500	23,500

[a]see Joos et al. [13].

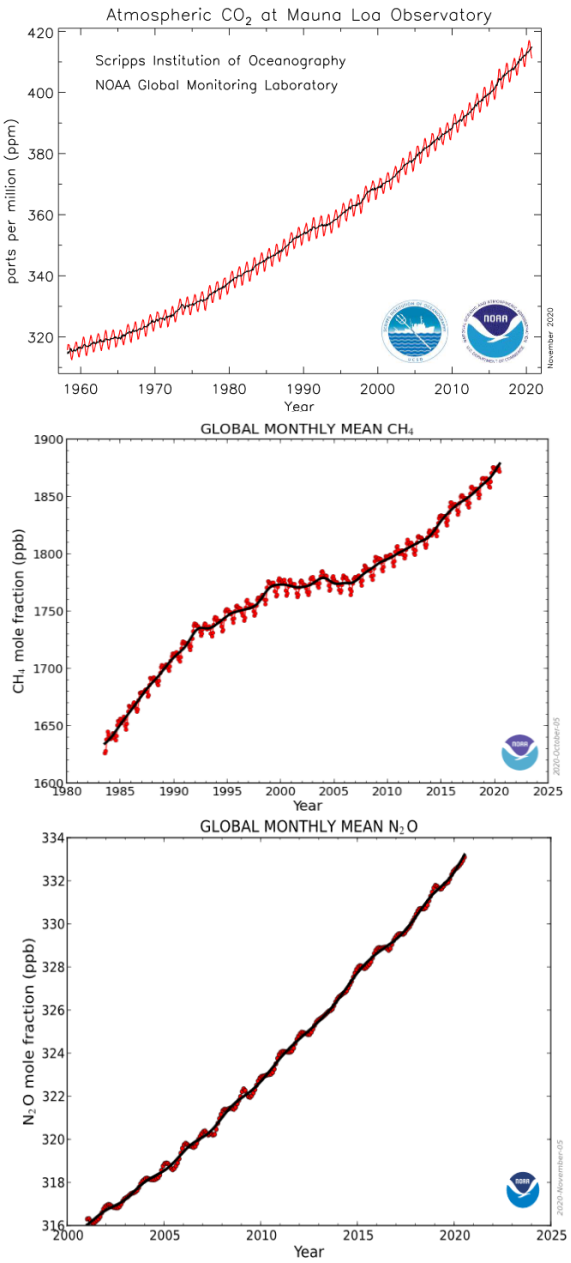

Figure 1.10. The graphs show atmospheric concentrations of CO_2, CH_4, and N_2O over time based on measurements. CO_2 is based on measurements from the Mauna Loa observatory while CH_4 and N_2O are globally averaged, monthly means determined from marine surface sites. Red lines represent monthly mean values and black lines represent the same after correction for the average seasonal cycle, i.e. the long-term trend. Figures from [14].

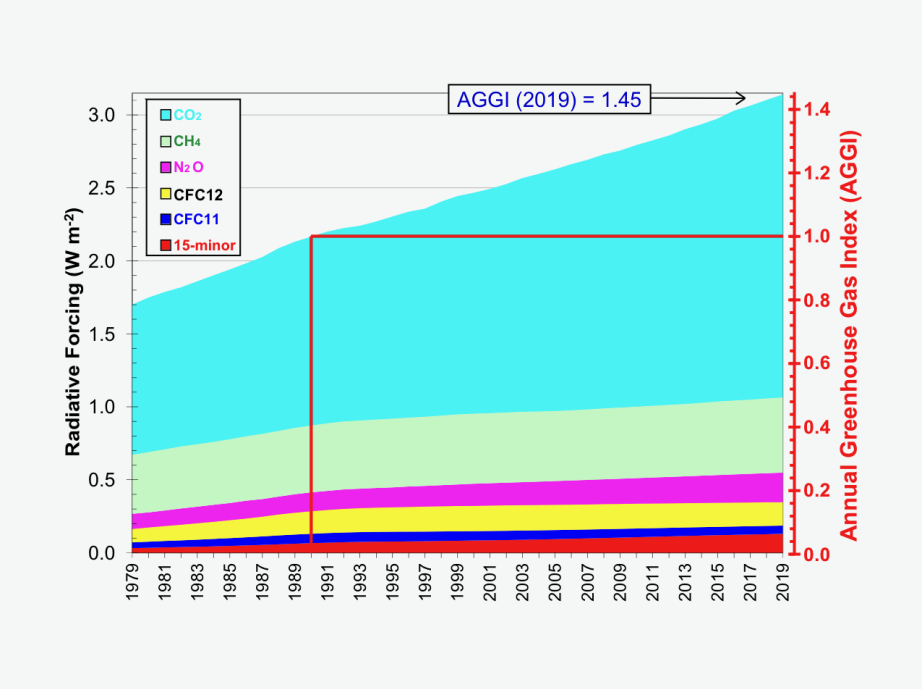

Figure 1.11. Radiative forcing relative to 1750 of major long-lived GHGs. The NOAA Annual Greenhouse Gas Index (AGGI) is shown on the right. It is set to 0 for 1750 and 1 for 1990 as that was the baseline year for the Kyoto Protocol. Figure from `https://www.esrl.noaa.gov/gmd/aggi/aggi.html` [15]

1.2.1 Sources & Sinks of CO_2 & CH_4

Since the industrial revolution (∼1750) the atmospheric concentration of CO_2 has increased from 278 ppm to ∼410 ppm [7,16]. Figure 1.12 shows the annual emissions and sinks of CO_2 in Pg/yr while Figure 1.13 shows the level of CO_2 in the atmosphere over the past 800,000 years. Although atmospheric concentrations have increased, anthropogenic CO_2 emissions far outweigh this atmospheric increase as emissions partition between the ocean, atmosphere, and land sinks. Indeed, only about 44% of the emissions of CO_2 have stayed in the atmosphere. Total emissions from concrete production and fossil fuel combustion between 1750 and 2011 are estimated at 375 ± 30 PgC (90% confidence interval) with land use change, primarily deforestation, contributing an additional 180 ± 80 PgC for a total of 555 ± 85 PgC. Approximately 28% (155 ± 30) has partitioned to the ocean (dissolution), another 28% (160 ± 90) to the land (carbon uptake by plants), and the remainder (240 ± 10) has resulted in an atmospheric increase in CO_2. $^{14}CO_2$ measurements show that the increased atmospheric concentration derives from fossil fuels [17,18]. The increasing land sink is likely caused by enhanced photosynthesis, related to increased atmospheric CO_2 and nitrogen deposition along with increased growing seasons in higher latitudes [7].

CH_4 emissions have also caused an increase in its global atmospheric concentration, from 715 ± 4 ppb in 1750 [19] to 1803 ± 2 ppb in 2011 [7]. There are three general types of sources and only one primary sink for CH_4, which is reaction with the hydroxyl radical. Emissions can be either biogenic, resulting from organic matter decaying in anaerobic conditions (stomachs of ruminants and termites, landfills, sewage, fresh waters, wetlands, rice paddies), thermogenic, i.e. fossil fuels, or pyrogenic, being formed from incomplete combustion of organic matter (biomass or biofuel burning) [7].

Total CH_4 emissions for 2000-2009 are estimated at between 553 (526-569) $Tg(CH_4)yr^{-1}$ based on top down (atmospheric observations) approaches and 678 (542-852) $Tg(CH_4)yr^{-1}$ based on bottom-up (emission accounting inventories) approaches, with values in

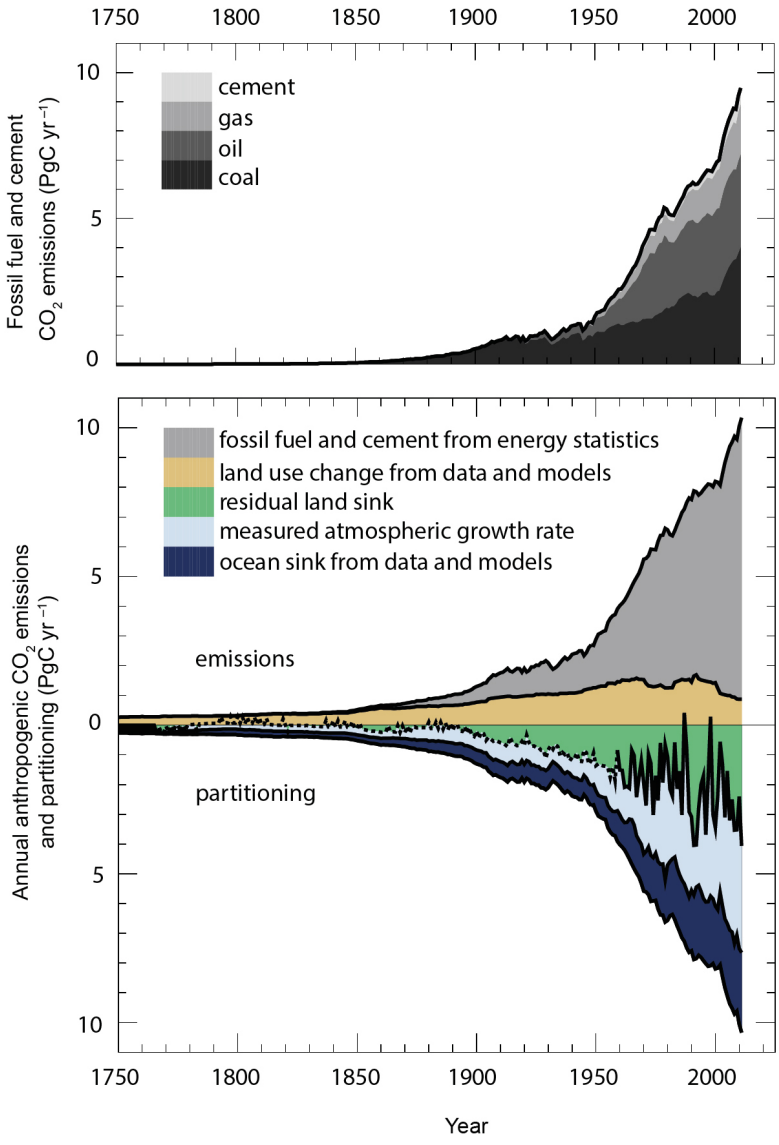

Figure 1.12. Annual anthropogenic emissions and sinks in PgCyr^{-1} from 1750 to 2011. Emissions are estimated based on UN energy statistics for fossil fuel combustion and U.S. Geological Survey estimates for cement production. Sinks are estimated based on a combination of modeling, ice core data, and atmospheric measurements. Magnitudes are based solely on changes since 1750 and natural movement of CO_2 through these sinks (lake outgassing, atmospheric uptake through weathering) are not included. The residual land sink is calculated as the residual of all other terms. Figure 6.8 from IPCC Fifth Assessment Report: The Physical Science Basis [7]

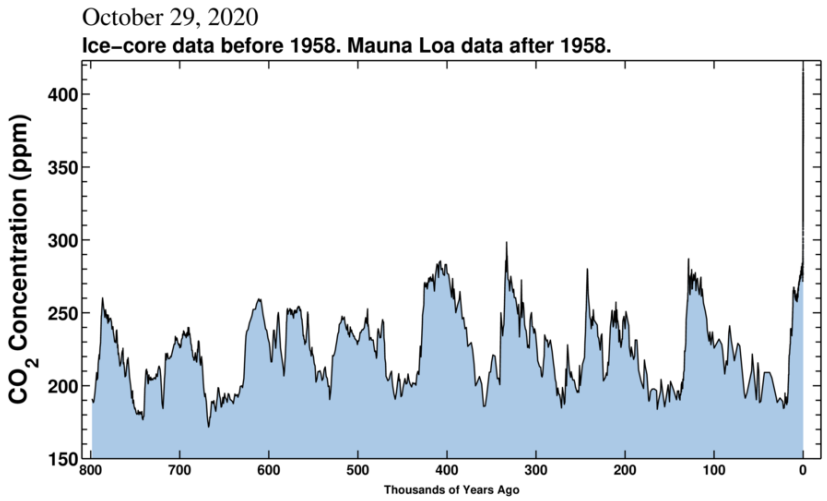

Figure 1.13. Long-term concentrations of CO_2 using measurements and ice-core data. For context, current measurements are ∼410 ppm, 1960 measurements were ∼320 ppm, and 1750 concentrations were measured via ice-core data to be ∼280 ppm. Concentrations did not surpass 300 ppm during this timeframe until recent years. Figure from the Scripps Institution of Oceanography [16].

parentheses representing the range across studies used [7]. Total sinks, primarily the reaction with the hydroxyl radical, are estimated at 550 (514-560) $Tg(CH_4)yr^{-1}$ for top down approaches and 632 (592-785) $Tg(CH_4)yr^{-1}$ for bottom-up approaches, leaving atmospheric growth rates (the imbalance of sources and sinks) of 3 (-4-19) $Tg(CH_4)yr^{-1}$ for top down and about 45 $Tg(CH_4)yr^{-1}$ for bottom-up as compared to the actual current (clearly variable through time, see Figure 1.10) measured growth rate of 6 $Tg(CH_4)yr^{-1}$ [7]. These emissions are detailed in Table 1.2. Bottom-up approaches involve modeling or scaling factor approximations (e.g. average emissions/ruminant based on case studies x cattle count estimates from the United States Department of Agriculture) for individual source sectors that are combined to estimate total emissions. Top down approaches begin with direct measurements of emissions from atmospheric measurements (e.g. ambient concentration measurements

made from rooftops and radio/cell towers, or via mobile platforms like cars or aircraft), and use them to estimate regional emissions. As such, top down approaches intrinsically provide a net emissions estimate based on all sources and sinks while bottom-up approaches can only account for those processes assessed. Uncertainties are also more difficult to determine with bottom-up approaches, but top down approaches cannot easily distinguish between the relative contribution of different sources like bottom-up approaches do [7, 20].

Anthropogenic emissions, including increased agriculture and ruminants, account for between 50 - 65% of these CH_4 emissions with top down approaches suggesting a larger fraction. Globally, this is primarily through agriculture and waste emissions with ruminants and landfills being responsible for 89 $Tg(CH_4)yr^{-1}$ and 75 $Tg(CH_4)yr^{-1}$ respectively. Fossil fuel emissions, primarily through fugitive emissions (leaks, venting, etc.) of natural gas ($\sim$90% CH_4), are 96 $Tg(CH_4)yr^{-1}$ and rice cultivation and biomass burning are both estimated at 35 $Tg(CH_4)yr^{-1}$. Natural emissions are dominated by wetlands, although uncertainties remain high due to high variability across models and limited observations. However, these emissions vary widely by region e.g., 90% of global rice emissions come from Asia. For the United States (U.S.) total anthropogenic emissions are estimated at 26 $Tg(CH_4)yr^{-1}$ for 2018, broken down as shown by Figure 1.14 [21]. Agricultural emissions, through both manure management and enteric fermentation (ruminant digestive emissions), are the largest source responsible for 38% of emissions. The energy industry is the next largest emitter at 28%, due to losses throughout the life cycle of natural gas and crude oil. Then landfills and wastewater treatment plants are the third largest source with 17% of U.S. emissions [21].

However, there have been a large number of studies focusing on natural gas CH_4 emissions in recent years, many of which suggest considerable underestimation of emissions from the EPA bottom-up inventory. The recent works were summarized and aggregated by Alvarez et al. [22]. They saw general agreement between bottom-up and top down approaches that suggested supply chain emissions (i.e. production,

Table 1.2.
2000-2009 global CH_4 budget. Reported values correspond to the mean and ranges [in brackets] represent minimum and maximum values across studies used. Adapted from Table 6.8 from IPCC Fifth Assessment Report: The Physical Science Basis [7]

$Tg(CH_4)yr^{-1}$	Top down	bottom-up
Natural Sources	218 [179-273]	347 [238-484]
Wetlands	175[142-208]	217[177-284]
Other sources	43 [37-65]	130[61-200]
Anthropogenic Sources	335 [273-409]	331 [304-368]
Agriculture and waste	209 [180-241]	200 [187-224]
Rice		36 [33-40]
Ruminants		89 [87-94]
Landfills and waste		75 [67-90]
Biomass burning	30 [24-45]	35 [32-39]
Fossil fuels	96 [77-123]	96 [85-105]
Chemical sinks	518 [510-538]	604 [483-738]
Tropospheric OH		528 [454-617]
Stratospheric OH		51 [16-84]
Tropospheric Cl		25 [13-37]
Emissions	553 [526-569]	678 [542-852]
Sinks	550 [514-560]	632 [592-785]
Imbalance	3 [-4-19]	46

processing, transport) of 13 $\pm$ 2 Tg/yr (95% confidence interval) or 2.3% of gross production in 2015, $\sim$60% larger than the U.S. EPA inventory estimate. The production sector represents the largest difference with $\sim$ 4 Tg CH_4/yr and this difference is attributed primarily to missed emissions during certain types of operating conditions (e.g. malfunctions). The recent studies suggest "heavy-tail" distribution functions that show a small number of facilities producing a large fraction of total emissions,

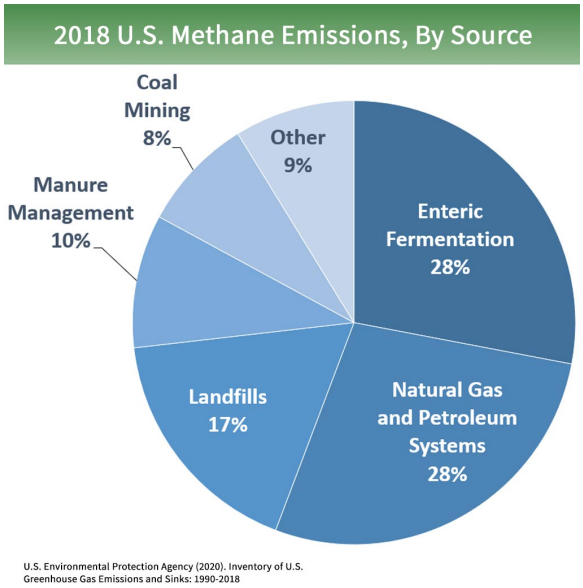

Figure 1.14. Breakdown of U.S. anthropogenic CH_4 emissions. Figure from `https://www.epa.gov/ghgemissions/overview-greenhouse-gases` [7]

attributed to events such as venting, e.g. manual liquid unloadings, which are intentional diversion of gas/fluids from a well to an atmospheric vent rather than a pressurized tank to increase flow temporarily to remove the much more valuable liquid fuels, and condensate/water [22, 23]. EPA component-based inventories would likely miss such large emission events due to the challenges associated with access to representative operating conditions.

1.2.2 Climate Change Impacts

Climate change impacts a large number of environmental and human systems with varying associated costs and hazards. A brief summary of some of the key hazards associated with climate change is provided in Table 1.3. Ocean acidification for example, results from the dissolution of CO_2 to produce carbonic acid, as shown in Equation 1.3 and has implications for all marine life, but particularly those that form

$CaCO_3$ for shells, such as corals. The partial pressure of dissolved CO_2 and pH during the same timeframe is shown in Figure 1.15. This is, however, not a complete list. For example, the Environmental Protection Agency (EPA) and Centers for Disease Control (CDC) discuss how increased temperatures can impact vector-borne diseases such as Lyme disease [24]. One can see in Figure 1.16 that not only have cases increased, but northern states like Vermont and Maine have seen a more significant increase. Although the number of cases is governed by multiple factors, there is evidence that climate change has increased the range of ticks and could impact their activity as winter seasons shrink and/or warm [24]. The World Health Organization states more generally that climate change affects many determinants of health (clean air, safe drinking water, food/shelter), likely lengthens vector-borne disease transmission seasons and alters their range, and some contributors to climate change are also contributors to health hazards (fossil fuel emissions contain health and climate-relevant compounds, land-use change modifies organism abundance and interactions leading to new opportunities for transmission, etc.) [25, 26]. The majority of these climate change impacts have large potential financial, health, and humanitarian costs that can be avoided. This is a large part of the driving force for climate change mitigation efforts.

$$\begin{aligned} &1) CO_2 + H_2O \rightleftharpoons H_2CO_3 \\ &2) H_2CO_3 + H_2O \rightleftharpoons H_3O^+ + HCO_3^- \\ &3) HCO_3^- + H_2O \rightleftharpoons 2H_3O^+ + CO_3^{2-} \end{aligned} \tag{1.3}$$

To discuss an example hazard, recent modeling efforts have investigated tropical cyclone intensity and frequency using CMIP5 with an assumed 2° C warming (consistent with ∼2055 warming based on the largest emissions scenario used by the IPCC, often considered business as usual) [29]. Overall tropical cyclone occurrence is expected to decline with a median estimate of -14% across investigated studies with a range from -28 to 22, with 87% of the 140 estimates suggesting ≤0%, although the physical basis is still being investigated. However, the proportion of cyclones that

Table 1.3.
A selection of hazards, risks, and vulnerabilities associated with climate change. Adapted from Table 19-4 from IPCC Fifth Assessment Report: Impacts, Adaptation, and Vulnerability. [27]

Hazard	Risks	Vulnerabilities
Sea level rise, coastal flooding	Death, injury, and disruption to economy and food/water supplies	High exposure of people, economic activity, and infrastructure in low-lying coastal zones and small islands
Extreme precipitation and inland flooding	Death, injury, and disruption of human security, particularly for vulnerable populations (elderly, children, etc.)	People exposed in urban areas to flooding. Overwhelmed, aging, and inadequate urban drainage infrastructure
Increasing frequency and intensity of extreme heat	Increased mortality and morbidity during periods of extreme heat, potential overloading of health and emergency services	increasing urban population of vulnerable groups (elderly, very young, those with chronic health problems) in areas subject to higher temperatures
Warming, drought, and precipitation variability	Risk of harm and loss of life due to malnutrition, insufficient water supply for people and industry resulting in significant health and economic impacts, loss of agricultural productivity and/or income of rural people. Risk of food insecurity	Poorer populations susceptible to resulting food insecurity, water shortages, constraints on increasing water supplies. Farmers in drylands or pastoralists with insufficient access to drinking and/or irrigation water.
Rising ocean temperature, ocean acidification, and loss of Arctic sea ice	Loss of coral cover, Arctic species, and associated ecosystems. Interactions of stressors such as warming and acidification on shell-forming organisms enhancing risk	High susceptibility of warm water coral reefs and the ecosystems they support, coastal communities dependent on these ecosystems (fishing, tourism, mitigation of storm flooding, etc.), high susceptibility of polar systems

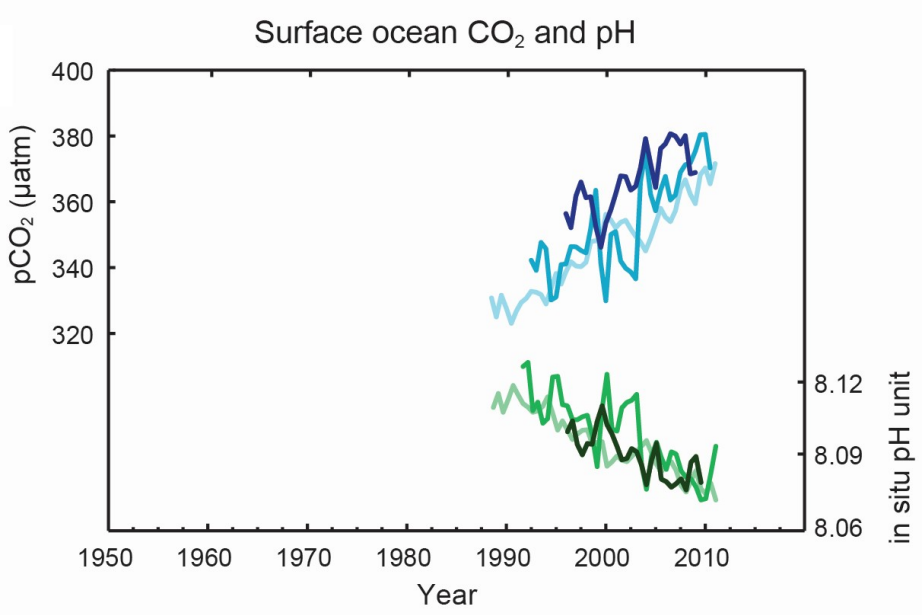

Figure 1.15. Partial pressure of dissolved CO_2 at the ocean surface (blue) and in-situ pH (green) measured from three stations (the two darker shades are from the Atlantic Ocean and the lightest shades are from the Pacific Ocean). The pH of ocean surface water has decreased by 0.1 since the beginning of the industrial era, corresponding to a 26% increase in hydrogen ion concentration. Figure 4 from the IPCC Fifth Assessment Report: Summary for Policymakers [28].

reach category 4-5 intensity, estimated to account for almost half of normalized economic damage from tropical cyclones, is expected to increase by 13% based on the median result across studies [29]. Sea level rise is also confidently expected to increase storm surge levels for tropical storms, leading to more significant economic damage. This is based solely on modeling studies, however, as the current data do not provide evidence of a statistically significant trend [29].

Given the large GWP and shorter lifetime of CH_4 relative to CO_2, it can be considered an important target for climate mitigation. Reductions in CH_4 have a more significant impact on short-term radiative forcing than comparable CO_2 emissions reductions, often making it more financially sensible to target CH_4 or similar non-CO_2 GHGs [30]. There are also relatively cheap reduction approaches available for

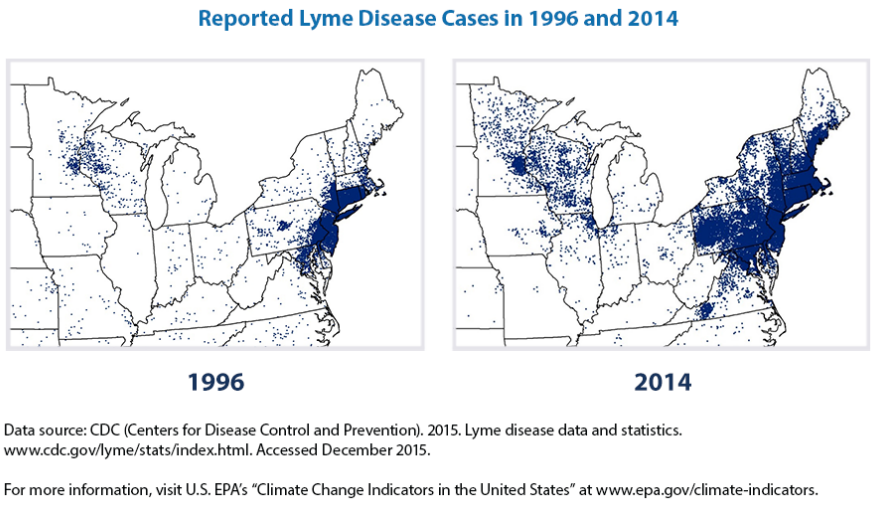

Figure 1.16. Reported cases of Lyme disease in 1996 and 2014 where each dot represents a case in that county. Figure from `https://www.epa.gov/climate-indicators/climate-change-indicators-lyme-disease`

non-CO_2 GHGs as compared to those available for CO_2. For example, landfill CH_4 can be captured and utilized as an energy source. Expanding these already existing technologies for landfills was estimated to reduce associated emissions as much as 70% at costs estimated at 10\$/ton CO_2 equivalent or less [30]. Alternatively, organic waste can be diverted from landfills and utilized through incineration in so-called waste to energy power plants, or through composting programs which can avoid emissions through aerobic treatment of the waste [30].

There are a number of agreements and policies in place to address climate change on scales ranging from individual cities to global agreements. The development of the United Nations Framework Convention on Climate Change in 1992 was followed shortly by the first of these global agreements, the Kyoto Protocol, in 1997 [5]. This document sets legal requirements for countries to monitor and report certain GHGs, adopt policies toward mitigation of GHG emissions, and worked to develop individualized targets for emission reductions. 37 industrialized countries and the European Community committed to reduce GHG emissions to an average of 5% less than 1990

levels by 2012 [5]. More recently the Paris Agreement effectively replaced the Kyoto Protocol in 2015 with the goal of keeping temperature rises this century well below 2°C with efforts to limit warming to 1.5°C. The agreement required members to prepare and maintain national commitments (Intended Nationally Determined Contributions; `https://unfccc.int/process-and-meetings/the-paris-agreement/the-paris-agreement/nationally-determined-contributions-ndcs`) and pursue measures towards them with stocktaking meetings planned every 5 years to communicate and reassess plans [5]. For the United States, at the time, the Intended Nationally Determined Contributions were an economy-wide reduction of GHG emissions by 26%-28% below its 2005 level by 2025 and to make best efforts to reduce its emissions by 28%.

1.3 Research Objectives

The research described in this thesis will focus on the development and application of methods for quantifying GHG emissions, determination of the uncertainties in these quantifications, and the performance of the methods used. An aircraft platform was used to investigate GHG emissions from the New York City (NYC) urban center and for an extensive sampling of U.S. power plants, which act as large, often isolated point sources of GHGs. The airborne platform enabled easy access to otherwise remote point sources that would be difficult to access from the ground and provided measurements representative of large spatial areas, which is difficult for ground/tower based instruments as they are more heavily influenced by nearby emissions [31]. The first study discussed here (Chapter 3) involved the sampling of natural gas-fired power plants (NGPP) primarily through sampling stack-based emissions near the source, to investigate the potential emissions of the fuel gas as uncombusted CH_4 or as site-wide emissions from leaks across the facility. This was part of a larger project by the Environmental Defense Fund (EDF) to improve confidence in emissions estimates from the end uses of natural gas. Building a large dataset of such flights enabled a

study (Chapter 4) investigating the accuracy of the quantification method since CO_2 emissions must be measured and reported to the EPA by power plant operators. Taking these reported emissions as near-true-values, with some estimated uncertainties, allowed us to thoroughly investigate the accuracy and precision of the quantification technique. Finally, emissions from the 5 boroughs of NYC were quantified (Chapter 5) using a combination of modeling and airborne measurements. Although beyond the scope of this work, this is part of a larger project focused on directly comparing results across methods for NYC. Additionally, although unintended, this dataset was collected shortly before the COVID-19 outbreak and will serve as a valuable baseline for airborne campaigns in the area looking to investigate changes to emissions during shutdown conditions. Potential improvements in data analysis and quantification will be discussed in the conclusions, Chapter 6.

2. EXPERIMENTAL

2.1 Instrumentation

Purdue's Airborne Laboratory for Atmospheric Research (ALAR) is a modified twin-engine Beechcraft Duchess designed to study air quality and greenhouse gas emissions. A Garmin global positioning system/inertial navigation system (GPS/INS) is used for 50 Hz geopositional coordinates (latitude, longitude, altitude). A Best Air Turbulence (BAT) probe [32, 33] is attached to the nose of the plane for 50 Hz 3-dimensional wind measurements. Two independent 50 Hz ambient temperature probes are used, 1) a Fast Ultra-Sensitive Temperature (FUST) probe (thermocouple) attached underneath the BAT probe [34] and 2) a microbead thermistor installed in the center port of the BAT probe. The 2 rear seats have also been removed to make a $\sim$1 m^3 volume for chemical instruments. In this space there is a Picarro model G2301-m cavity ring down spectrometer [35] for 0.5 Hz measurements of CO_2, CH_4, and H_2O_v concentrations, a 2B model 202 ozone monitor for 0.1 Hz O_3 measurements, a Grimm aerosol spectrometer model 1.109 for measurements of particle concentrations at 6 second intervals and 3 compressed gas calibration standards prepared by the National Oceanic and Atmospheric Administration (NOAA) according to World Meteorological Organization (WMO) standards. When necessary, 2 of the calibration standards can be removed to allow space for larger/heavier instruments as well. In several flights discussed in Chapter 3 this space was used for a direct absorption ethane (C_2H_6) spectrometer designed by Aerodyne Research and modified at Harvard University. The instruments focused on in this work are shown in Figure 2.1.

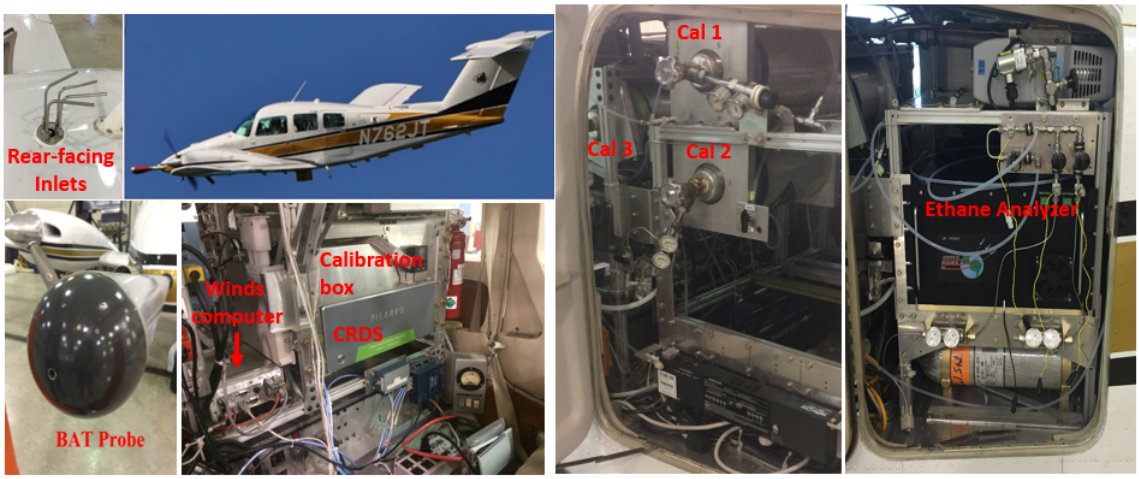

Figure 2.1. Purdue's Airborne Laboratory for Atmospheric Research (ALAR) with specific instruments labelled. The roof inlets are used rather than the large front-facing inlets as there was some evidence of leaking air in the large manifold.

2.1.1 Ethane Analyzer

The ratio of $\Delta C_2H_6/\Delta CH_4$ is useful to identify NG-derived CH_4 signals in complex regions where there are other CH_4 sources, since natural gas contains a small percent C_2H_6 while most other CH_4 sources (e.g. landfills and waste-water treatment facilities) will not emit C_2H_6 [36]. The C_2H_6 spectrometer is a tunable diode laser spectrometer, operated by passing a mid-infrared light source through a multi-pass Harriot cell [37] with an effective path length of 76 m, the schematic of which is shown in Figure 2.2. Recent advances in inter-band laser technology have led to lasers that can now be used to investigate the ro-vibrational infrared absorption of C_2H_6 at the 2997 cm^{-1} q-branch shown in Figure 2.3. Spectra are fit based on experimentally determined absorption parameters [38]. In flight, the precision of the C_2H_6 signal is approximately 30 ppt when the spectra are averaged to 1 Hz while the atmospheric background C_2H_6 concentration in the Northern Hemisphere typically ranges from 500 to 2,200 ppt [39]. The C_2H_6 mixing ratio is calibrated using periodic injections

of ultra-zero air to account for possible drift in the background as well as periodic injections of a known concentration standard traceable to WMO and NOAA standard scales [40].

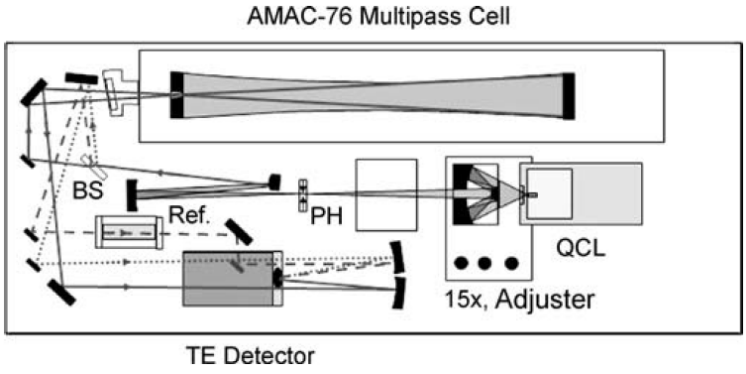

Figure 2.2. Schematic diagram of the C_2H_6 analyzer. The only significant change is that the quantum cascade laser (QCL) was replaced with an interband cascade laser to measure at the low wavenumber peak. 15x is the 15 power reflecting objective; Adjuster is the 3-axis position adjuster for the objective; PH is the 200 micrometer pinhole; BS is the BaF_2 beamsplitter; Ref is the 5 cm low-pressure reference cell and the thermoelectrically cooled detector is above the indicated beam lines. [37].

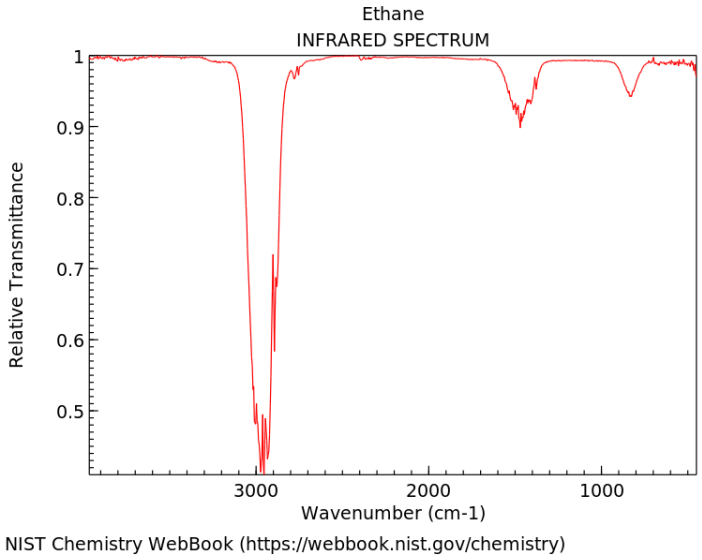

Figure 2.3. Transmittance spectrum of C_2H_6 in wavenumbers from the NIST chemistry WebBook [41]. The 2997 wavenumber peak is used by the ethane spectrometer.

2.1.2 Cavity Ring Down Spectrometer

Cavity Ring-down Spectroscopy (CRDS) helped to revolutionize the field of GHG quantification as these systems are able to detect ppb levels of CO_2 and CH_4 with high sensitivity and precision, are linear over typical atmospherically relevant concentrations, and do not require frequent calibrations. Picarro introduced commercially available instruments capable of 0.5 Hz measurements of CO_2 CH_4 and H_2O_v in 2010 [35, 42]. The most well-established technique used for GHG measurements of CO_2 before the development of CRDS was non-dispersive infra-red spectroscopy (NDIRS). These instruments required frequent zeroes and calibrations, making use of the instruments, particularly in remote measurement sites, more difficult and expensive. Additionally, the instruments were not precise enough for atmospherically relevant CH_4 measurements.

Figure 2.4 shows a block diagram of the Picarro G2301-m model used throughout this thesis. This model uses two telecom-grade distributed feedback (DFB) lasers with

a wavelength monitor. One laser is tuned to measure a single CO_2 absorption feature at 1603 nm and the other is tuned to measure H_2O_v and CH_4 spectral features at 1651 nm. Laser light is injected into a high-finesse optical cavity consisting of three mirrors (99.999% reflective) through one partially reflecting mirror. The light intensity inside the cavity builds up over time and is monitored through a second partially reflecting mirror via a photo-detector outside the cavity. Once the light intensity reaches a set threshold, the laser is turned off and the exponential decay of the light is measured as shown in Figure 2.5. The light decays as the cavity is not 100% reflective and some of the laser light leaks out of the cavity. The light remains trapped in the cavity for a long enough period of time to create an effective path length of tens of kilometers, giving the CRDS a high sensitivity. The patented Picarro wavelength monitor is solid-state without moving parts and provides wavelength measurements over a range of >100 nm with a 1σ precision of 1 MHz [35].

The measured ring-down time is directly proportional to the concentration of the absorbing species within the cavity. The concentration of the absorbing gas (N) can be calculated using Equations 2.1 and 2.2.

$$\frac{I(t)}{I(t=0)} = exp\left(\frac{-t}{\tau}\right) \tag{2.1}$$

$$\tau(\lambda) = \left(\frac{l_{cav}}{c}\right)(L_{opt} + \sigma(\lambda)Nl_{sample})^{-1} \tag{2.2}$$

Here I(t=0) is the threshold light intensity exiting the cavity when the laser is turned off, I(t) is the light intensity exiting the cavity at time t, and ($\tau(\lambda)$) is the ring-down decay constant for a given wavelength, λ. Then l_{cav} is the optical length of the cavity, c is the speed of light, L_{opt} is the optical loss of the empty cavity, σ is the absorption cross section of the species at a specific wavelength, N is the species concentration, and l_{sample} is the physical length of the of the cavity. This relies entirely on the timing of the light decay rather than direct absorption measurements, so measurements are not impacted by fluctuations in laser voltage or shot noise [35]. The slope and intercept

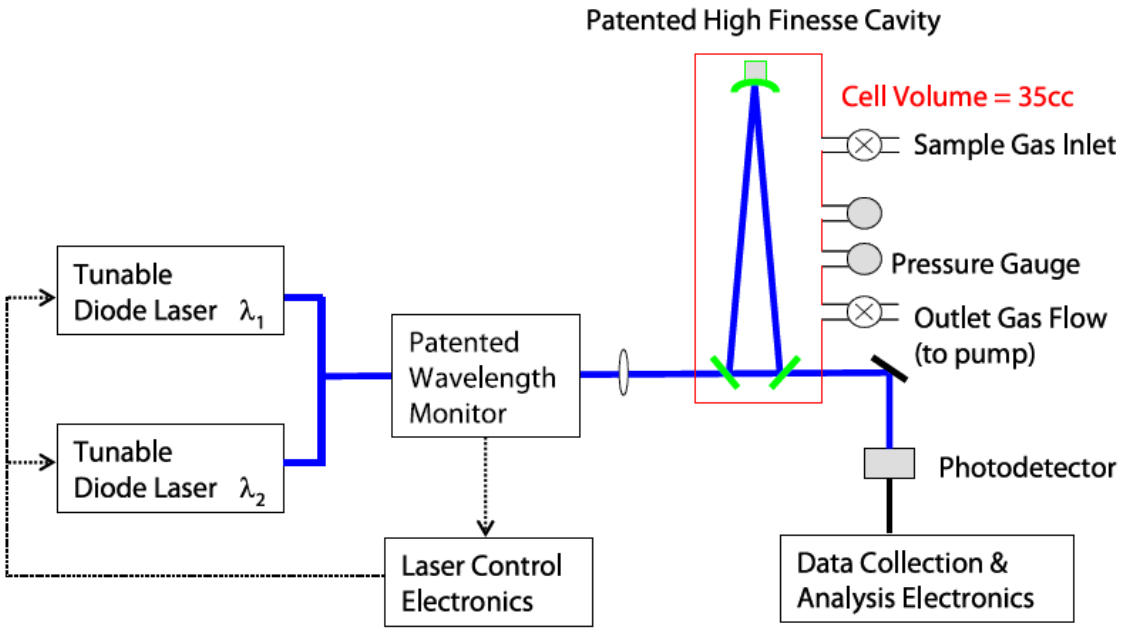

Figure 2.4. A block diagram of the Picarro CRDS instrument. One laser (λ_1) is tuned to a single spectral feature of CO_2 at 1603 nm while the other (λ_2) is tuned to measure H_2O_v and CH_4 spectral features at 1651 nm. Figure is from Crosson [35]

of all in-air calibrations is shown in Figure 2.6, demonstrating the long term stability. An example in-flight 3-point calibration is shown in Figure 2.7.

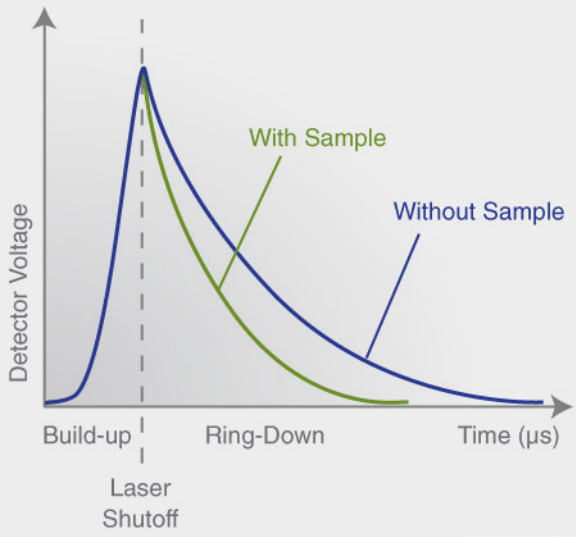

Figure 2.5. Conceptual diagram of the exponential decay (ring-down) approach of the Picarro. The ring-down rate is proportional to the concentration of the absorbing species in the sample cell. Figure from `https://www.picarro.com/company/technology/crds` [43]

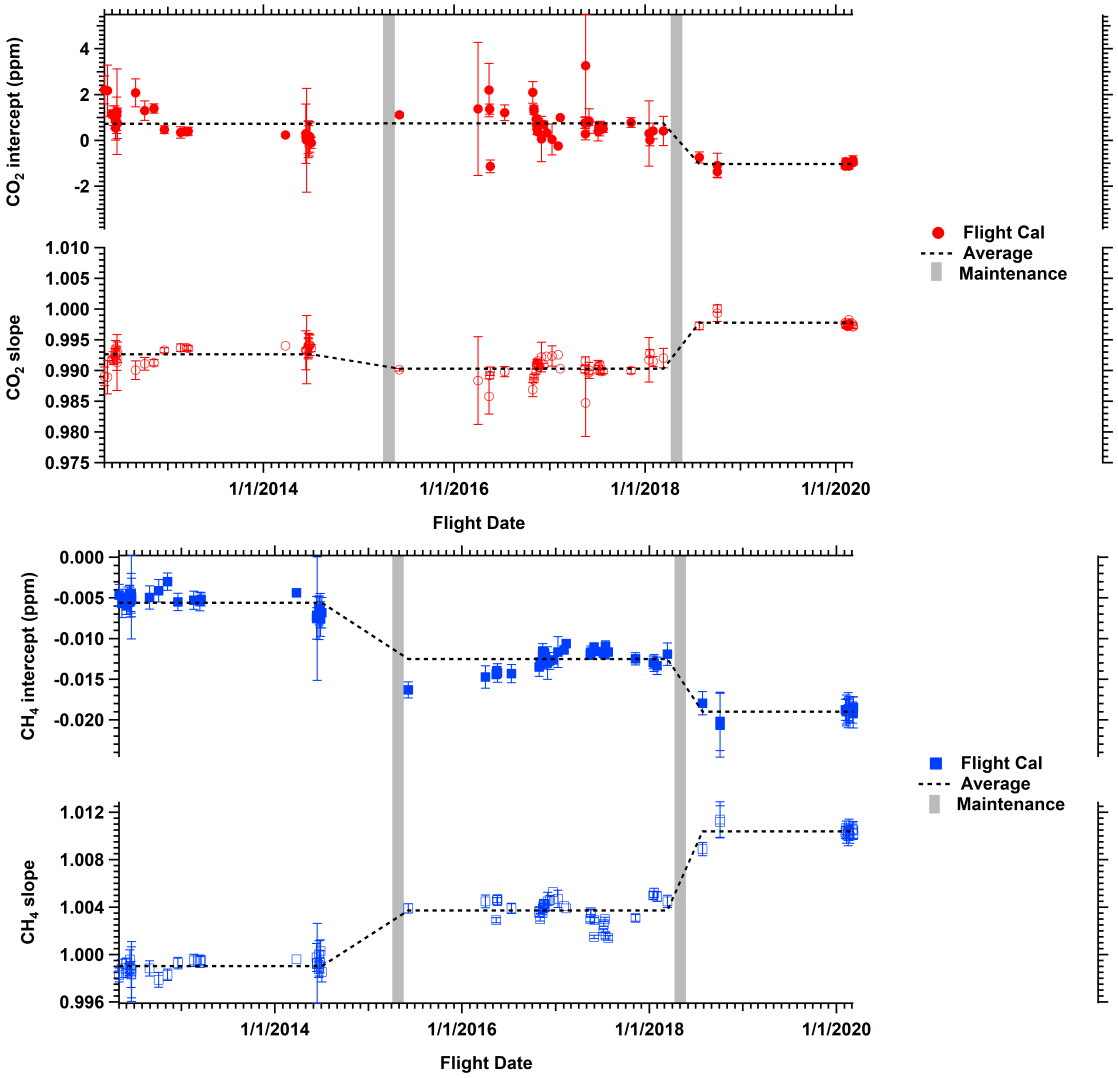

Figure 2.6. Long-term stability of the Picarro CRDS G2301-m CO_2 and CH_4 calibrations. Error bars represent 1σ. Calibration coefficients did change after maintenance events in the Springs of 2015 and 2018. Note the narrow ranges of the y-axes.

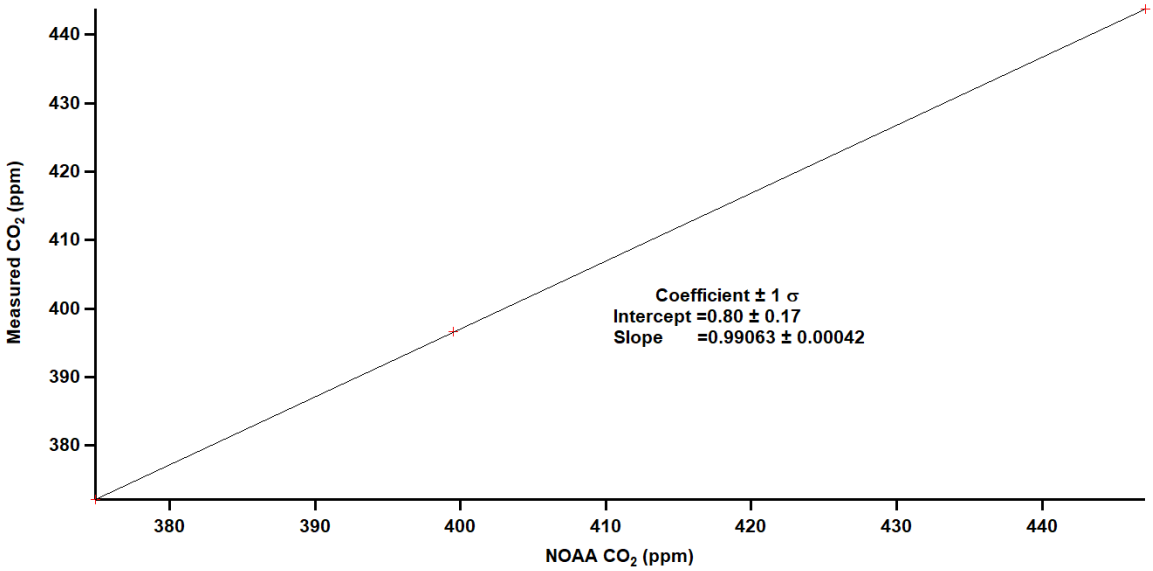

Figure 2.7. Example in-flight calibration curve for CO_2 on 11/19/2016. Each point represents the average of 2 minutes of sampling from the NOAA standard. Each tank was sampled twice and all 6 data points are shown.

2.2 The Airborne Mass Balance Method

The primary technique used in Chapters 3 and 4 of this thesis is the airborne mass balance experiment (MBE). This approach has been used to quantify emissions at scales ranging from point sources [44,45] to large shale oil/gas fields and cities [45–51]. The basic premise of the method involves measuring the upwind and downwind sides of a theoretical cube as illustrated in Figure 2.8. The mass of interest is an analyte emitted from a source within the cube (e.g. a power plant) and the intent is to quantify emissions through the downwind vertical plane while accounting for the signal flowing into the cube (background). Emissions adjacent to the pollutant plume (dashed lines in Figure 2.9) can be used to define this background, assuming it equivalent to the relevant upwind emissions, i.e. no significant change in signal between upwind and downwind. The flux or flow in units of mols/m^2s, of the tracer through the downwind side of the cube can then be calculated as the signal above background (enhancement) of the tracer multiplied by the wind speed. This can be converted to an emission rate (ER) in units of mols/s, by integrating the flux across the x, y, and z dimensions [50].

All MBEs are conducted during midday ($\sim$12 pm - 4 pm local time) when the CBL is well developed and the BLH relatively constant [1]. Flights include either a circle around the emitter/collection of emitters or an upwind horizontal transect to determine if other sources could significantly influence downwind measurements. MBEs are conducted by flying multiple horizontal transects, typically in 250 ft intervals, at a fixed distance downwind of the site from as low to the ground as is safe to the highest altitude where emissions can be seen, often with a vertical spiral through the downwind plume (see Figure 2.10) to estimate the BLH. In a small number of cases, the cloud base must be used as BLH due to heavy cloud cover. As discussed in Chapter 1 and shown in Figure 2.11, the BLH can be identified using the inflection point of potential temperature and significant changes in surface emitted compounds, particularly H_2O_v. The transects extend sufficiently beyond the edges of the plume so that GHG concentrations return to background concentrations. A standard linear

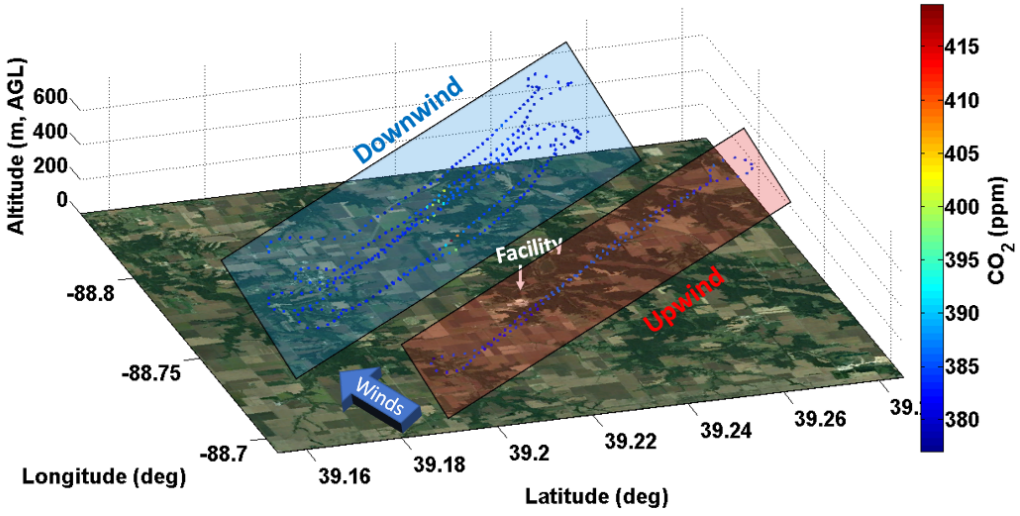

Figure 2.8. 3D plot of an example MBE with upwind and downwind areas, average wind direction, and the source labeled. Data points are colored by measured concentration and have been averaged down to 0.25 Hz for plotting.

regression is fit through this background data, with concentration as the dependent variable and distance along the downwind transect as the independent variable, to estimate the transect's background [45, 50, 52, 53]. This is done separately for each transect as there can be gradients in the background with altitude [46]. Point-wise enhancements are then calculated as the measured concentrations minus the background values.

These point-wise enhancements are converted to point-wise fluxes according to Equation 2.3.

$$\text{Flux}_\text{i} = \frac{([C]_i - [C]_{bg,i}) \times U_{\perp,i} \times P_i \times A}{T_i \times R} \tag{2.3}$$

Here the molar density of air ($\text{mol}_{air}/\text{m}^3$) is calculated using the ideal gas law with measured pressure (P_i in atm), measured temperature (T_i in Kelvin), and the ideal gas constant (R in atm m^3/mol K). This is multiplied by the perpendicular component of the measured winds ($\text{U}_{\perp,i}$ in m/s) and the enhancement in concentration ($[\text{C}]_i$ -

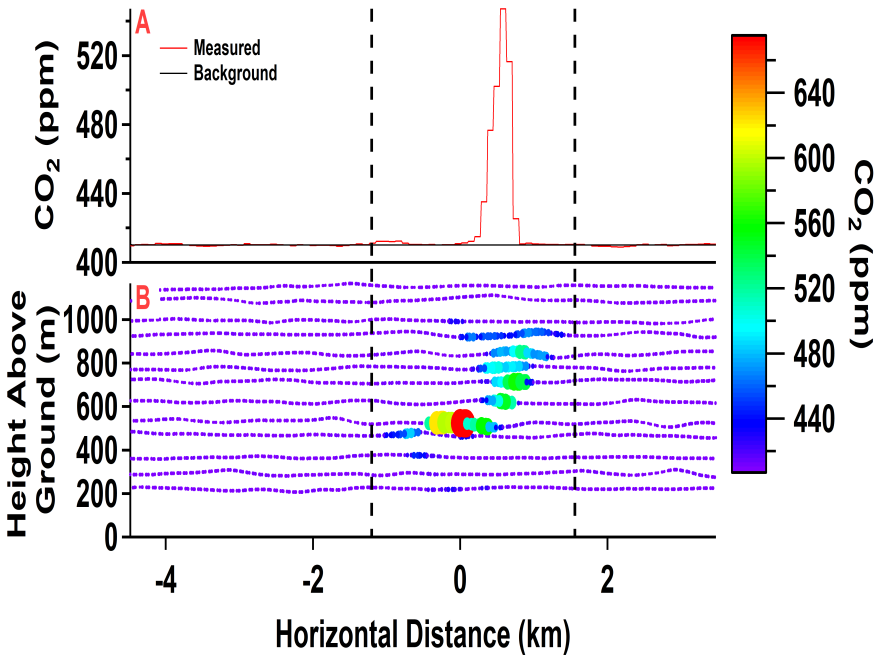

Figure 2.9. Example MBE dataset downwind of a power plant. A) measured concentration and background for the transect at 600 m. B) All measured transect data size and color scaled by CO_2 concentration. Vertical lines represent the edges of the plume.

$[C]_{bg,i}$) (mol_c/mol_{air}) to get a flux (mol/m^2s) at each point. A is a constant to convert concentrations from ppm to mol fraction (10^{-6}).

These point-wise fluxes are then interpolated into a complete 2-dimensional plane through kriging using the Matlab EasyKrig package [46, 50, 54]. Pixels are defined as 100 m x 10 m (width x height) and drawn from 0 m to the BLH (z_i) or the highest transect flown if transects went above the plume. The ER (mols/s) is finally calculated by integrating these pixels across the horizontal and vertical bounds of the plume from the surface to the BLH according to Equation 2.4.

$$MBE\ ER = \int_0^{Z_i} \int_{-x}^{x} \mathrm{Flux_i}\ \ \mathrm{d}x\,\mathrm{d}z \tag{2.4}$$

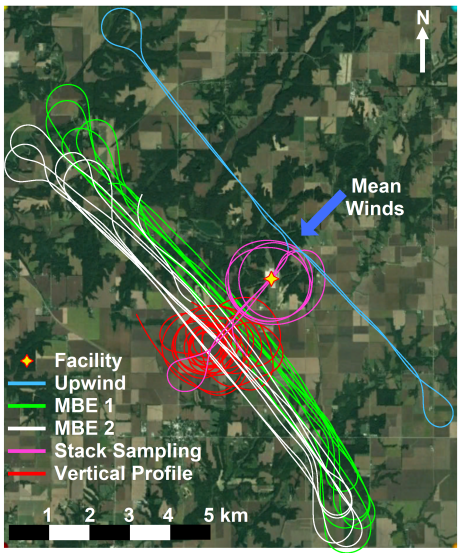

Figure 2.10. Typical MBE flight design for power plants with key features labeled. Stack sampling of power plants is discussed further in Chapter 3. Map data from Google.

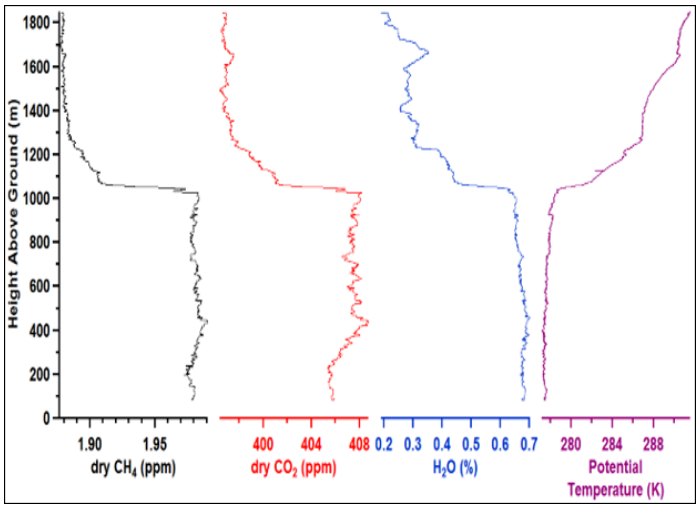

Figure 2.11. Example vertical profile (VP) flown downwind of Indianapolis in November of 2012. The BLH on this flight is clear at ∼1050 m by sharp changes in all trace gases, H_2O_v, and potential temperature.

2.3 MBE uncertainty calculation

Calculating the uncertainty for MBEs involves propagating the uncertainty of multiple terms and estimating the impact of flight conditions and interpolation. ERs for CO_2 and CH_4 are calculated according to Equation 2.4 for all MBE's. Power plant plumes are relatively narrow and transects always extend well beyond the plume to ensure there is good background data. As such, these MBEs have a significant amount of background data that can impact results if incorporated into the ER. Given a linear regression is used to define the background, small positive or negative enhancements exist in background data. Incorporating these small signals into the ER can have a sizable impact because of the significant amount of background data relative to the amount of plume data (e.g. in Figure 2.9 $\sim$2 km along the transect are plume data compared to a total of 4 km along the transect that is background data). To avoid this impact, we used only data within the horizontal bounds of the plume in all ER calculations including uncertainties. The uncertainty in these ERs is a combination of 1) uncertainty in the point-by-point flux measurements (relatively easy to calculate) 2) uncertainty due to incomplete capture of the plume (quite challenging to estimate), and 3) uncertainty introduced by the kriging interpolation, as described in Equation 2.5.

$$\frac{\delta_{ER}}{ER} = \sqrt{\left(\frac{\delta_{Flux}}{Flux}\right)^2 + \left(\frac{\delta_{Plume\ Capture}}{Plume\ Capture}\right)^2 + \left(\frac{\delta_{Krig}}{Krig}\right)^2} \tag{2.5}$$

Plume Capture Uncertainty

Our estimate of plume capture uncertainty is directly inferred from interpolating the flight data. Emissions typically exist below the lowest altitude transect that can be flown given general flight restrictions and safety concerns and there are multiple means to estimate them [47, 55, 56]. In Chapter 3 we reported the ER as the average ER between kriging only measured data (transect-only) and kriging to the ground. The uncertainty introduced by the plume capture $\left(\frac{\delta_{Plume\ Capture}}{Plume\ Capture}\right)$ is calculated as the

relative difference between this average and kriging only measured data. In three cases a synthetic transect, defined as identical to the lowest measured transect, was added to the surface to improve the kriging performance (synthetic krig). Kriging is primarily designed for interpolation, not extrapolation, and thus it can have difficulty reasonably extrapolating to the surface, particularly with a large range of altitudes without data as is sometimes the case below our lowest transect. In these three cases we report the average of the transect-only ER and the synthetic krig ER. All other uncertainty terms for these cases were calculated in the same manner as other flights.

In Chapter 4 this was refined further as the transect-only ER is definitively biased low, unless the bottom of the plume has been captured and kriging with a synthetic transect should be a relatively reasonable approximation. As such, averaging the two will result in an ER that is biased low. Instead, all results in Chapter 4, including those used in Chapter 3, are reanalyzed using three different approaches with the average being used as the calculated best-estimate ER, and the standard deviation as the plume capture uncertainty.

If the plume is approximately well mixed in the vertical then the average plume would represent average emissions at any height and can be used to estimate emissions near the surface (plume average approach) [45,48]. This is done by taking the average of all 10 m vertical altitude bins with plume signal in the kriged matrix (plume being defined here as any 10 m bin with data $\geq$5% of the single pixel maximum). If the plume is not well mixed then the lowest altitude transects are the best representation that we have of near surface data. We use these data in two different approaches, the synthetic krig approach already discussed and an approach in which we use the average of the lowest 3 transects to fill the gap between our lowest pass and the surface (three-pass average approach). Reported ERs represent the average across these three approaches (three-pass average, plume average, synthetic krig) and the variability across them is used as an estimate of plume capture uncertainty.

As the average plume and three-pass average approaches would greatly overestimate emissions if the plume was completely captured within the altitudes flown, we

use the transect-only approach in these cases and consider uncertainty due to plume capture 0%. An example where the plume was completely captured is shown in Figure 2.12. In a small number of MBEs where the top of the plume was not observed and emissions between the BLH (estimated with vertical profiles or as cloud base in the case of overcast conditions) and the top transect flown needed to be approximated, these same approaches were used with the exception that a synthetic transect = 0 flux was placed at the BLH, rather than a copy of the highest transect flown. Figure 2.13 provides a visual example of all four approaches.

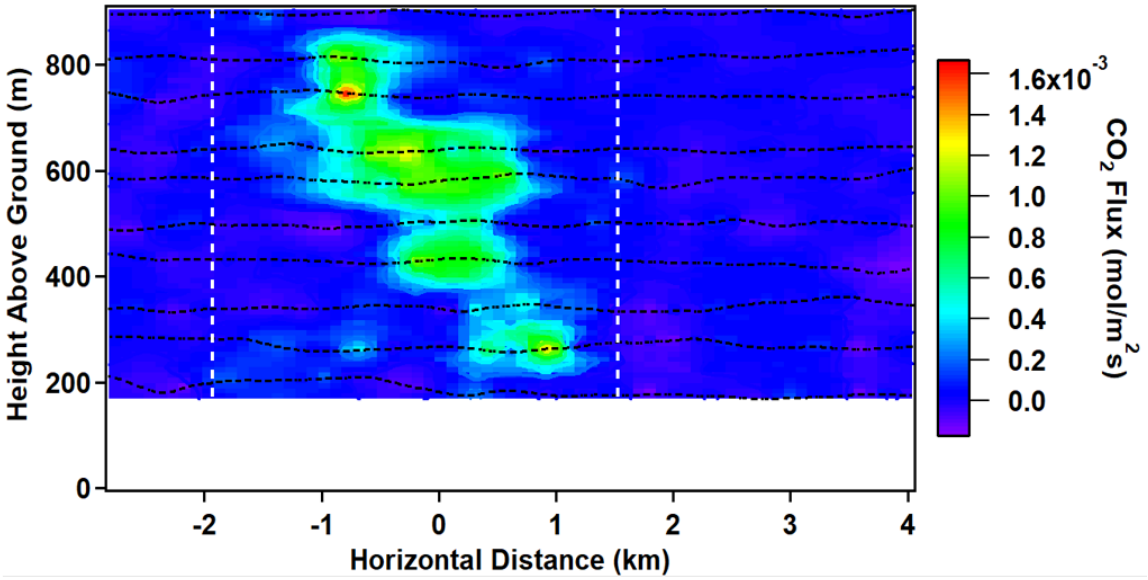

Figure 2.12. The kriged map of a power plant MBE on 11-15-2016 with transects shown in black dashed lines. This shows a case where emissions were completely captured within the transects flown.

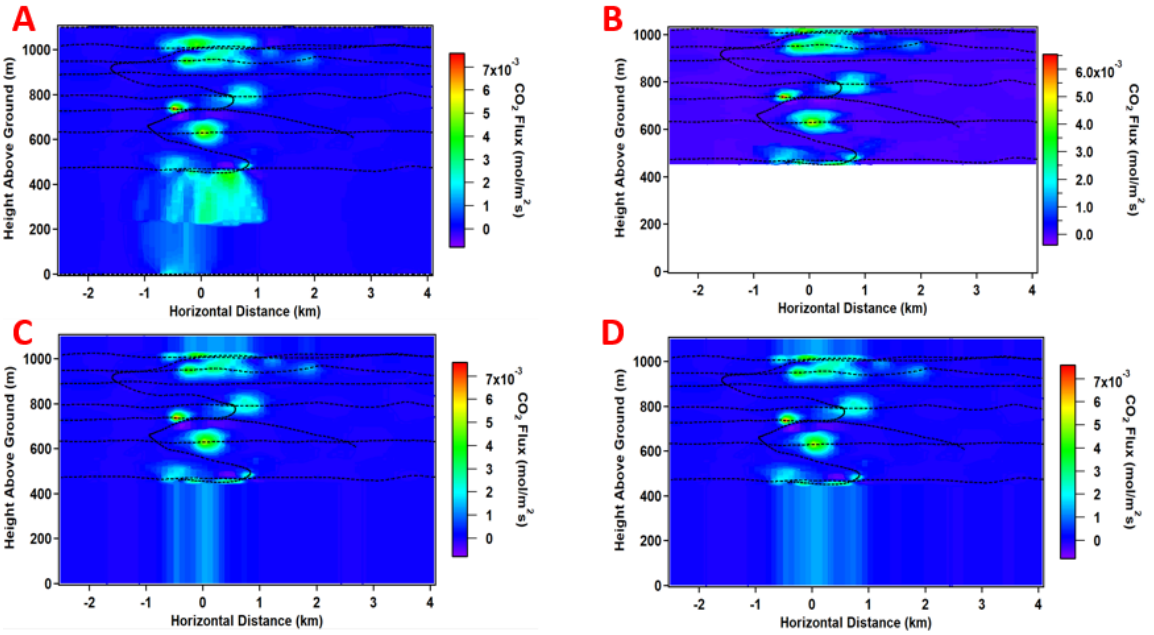

Figure 2.13. The kriged map of a power plant MBE on 11-14-2016 with transects shown in black dashed lines. This is one of the few cases that did not capture the top of the plume. A) The synthetic krig approach. B) The transect only approach. C) The three-pass average approach. D) The plume average approach.

Kriging Uncertainty

The kriging uncertainty has been estimated in the past by Cambaliza et al. [50] who reported average relative interpolation uncertainties of 12% and 8% for CO_2 and CH_4 respectively and relative extrapolation uncertainties of 13% and 10% for CO_2 and CH_4 respectively. We directly calculate each flight's extrapolation uncertainty with our plume capture uncertainty term and use a new approach to calculate the relative interpolation uncertainty. We recalculated ERs using an approach based on the Lattice Krig package in R [57–59] developed through a collaborative effort with NIST. This method is not finalized and thus could not be used as a replacement for EasyKrig [54], but we were able to directly compare the ER results from this method to the EasyKriging approach for a subset of flights. To avoid incorporat-

ing extrapolation uncertainties, only transect data was kriged for this comparison. Additionally, many flights showed small CH_4 ERs which can cause large relative uncertainties from small absolute ER changes. As such, we have chosen to use only CO_2 data to determine $\left(\frac{\delta_K rig}{Krig}\right)$ as all CO_2 ERs are large enough in magnitude for relative uncertainties to be independent of ER magnitude. First, we calculate the relative difference between the ER calculated using the 2 different kriging schemes, shown in Table 2.1. Then, since $\left(\frac{\delta_K rig}{Krig}\right)$ is meant to represent the interpolation uncertainty of the method, we average these relative differences across all flights.

Table 2.1.
Relative Difference Between Kriging Transect Data with EasyKrig [54] and Kriging with a Lattice Krig [57–59] Based Approach[a]

Date	Plant	CO_2 ER using EasyKrig (kg/hr)	CO_2 ER using Lattice Krig (kg/hr)	Relative difference (%)
11/13/16	P6	584,000	568,000	3
11/19/16	P6	820,000	998,000	22
11/19/16	P6	1,023,000	1,223,000	20
11/14/16	P8	139,000	104,000	25
11/17/16	P8	93,000	76,000	18
11/17/16	P8	109,000	93,000	15
5/18/17	P3	244,000	207,000	15
5/18/17	P3	173,000	213,000	24
7/7/17	P3	670,000	562,000	16
7/24/17	P3	329,000	269,000	18
7/24/17	P3	290,000	280,000	3
7/24/17	P4	149,000	162,000	9
7/24/17	P4	108,000	98,000	9

[a]The average is a 15% relative difference, within the variability of the 12% ± 14% calculated in Cambaliza et al. [50]

Flux Uncertainty

The last term, $\left(\frac{\delta_F lux}{Flux}\right)$, is the most involved as it must incorporate uncertainties from each parameter used to calculate fluxes shown in Equation 2.3. Each of the measured values has a relative uncertainty that can be propagated, but the uncertainty in the background must be estimated. Most of these terms have straightforward uncer-

tainty calculations, although some may be biased high. The relative uncertainty in pressure is calculated as the relative difference between the measured pressure and the barometric pressure calculated using the most recent surface pressure measurements from a nearby airport $\left(\frac{P_i - P_{bar,i}}{P_i}\right)$ and the barometric law, i.e. $\mathrm{P_z} = \mathrm{P_{surface}} e^{-z/H}$ where H=RT/Mg, M being the molar mass of air (0.02896 kg/mol), R the gas constant, T the temperature, and g the acceleration due to gravity. This uncertainty is biased high as the barometric law does not have to precisely agree with the measured pressure at altitude. The relative uncertainty in temperature is calculated as the relative difference between the two separate measurement systems on ALAR, the thermistor microbead and the FUST probe $\left(\frac{T_{bead,i} - T_{FUST,i}}{T_{bead,i}}\right)$. The relative uncertainty in the perpendicular component of the wind is based on the reported horizontal wind uncertainty of 0.4 m/s $\left(\frac{0.4}{U_{\perp,i}}\right)$ from Garman et al. [34]. Lastly, the relative uncertainty in the enhancement is based on a combination of the uncertainty in the calibration and that of the background $\left(\frac{\sqrt{\delta_{cal}^2 + \delta_{BG}^2}}{Enhancement}\right)$.

The combination of these terms is the square root of the sum of squares of relative errors as shown in Equation 2.6 given the individual terms are multiplied together to get the flux as described in Equation 2.3. All terms other than the enhancement term are based on the average of the relative uncertainty throughout the flight.

$$\frac{\delta_{Flux}}{Flux} = \sqrt{\left(\frac{\delta_{U,i}}{U_{\perp,i}}\right)^2 + \left(\frac{\delta_{P,i}}{P_i}\right)^2 + \left(\frac{\delta_{T,i}}{T_i}\right)^2 + \left(\frac{\sqrt{\delta_{cal}^2 + \delta_{BG}^2}}{Enhancement}\right)^2} \tag{2.6}$$

The uncertainty in the calibration for the enhancement term is the propagated uncertainty of the slope and intercept of the calibration curve. The background used for all flights is a linear regression through the background concentrations on the transect edges, done for each transect separately. The uncertainty in the background is therefore calculated as the standard error of this linear fit:

$$\delta = \sqrt{\frac{\sum r^2}{N - P}} \tag{2.7}$$

where r is the residual (measured – fit) for background data, N is the number of points used, and P is 2 since the fit used 2 parameters (slope and y-intercept). This does

not accurately capture the uncertainty due to the choice of background or method of defining the background, but solely describes the agreement between the fit used and measured background data. This value is made relative by dividing by the calculated background point-wise. Finally, this is converted from a relative uncertainty in the background to the absolute background component of the uncertainty by multiplying by the point-wise enhancement.

Finally, the calibration and background uncertainty terms can be combined to get an enhancement uncertainty term to use in Equation 2.6. The absolute error in the enhancement is calculated by combining the point-wise absolute uncertainty in the background and the point-wise calibration uncertainty as the square root of the sum of squares $\left(\sqrt{\delta_{cal}^2 + \delta_{BG}^2}\right)$. To calculate the average relative error in the enhancement for the entire flight we first combine the point-wise absolute uncertainties as the square root of the sum of squares for each transect separately. This is the uncertainty in each transect's total enhancement and is made relative to that transect's summed enhancement. Finally, this is converted to a flight average by squaring the relative uncertainty for each transect, averaging these relative variances together, then taking the square root of this average variance to get a flight-averaged relative uncertainty in the enhancement $\left(\frac{\sqrt{\delta_{cal}^2+\delta_{BG}^2}}{Enhancement}\right)$. As mentioned previously, all calculations including uncertainty terms exclude background data. However, there are also often transects without any significant enhancement. To address this, we only consider transects that contribute at least 5% to the total enhancement of the MBE in the calculation of an MBEs enhancement uncertainty. Relative uncertainties for transects with total enhancements near 0 would otherwise approach infinity and dramatically skew the MBE uncertainty. Typical uncertainties and ERs are shown in Table 3.4 in Chapter 3.

3. OBSERVATIONS OF METHANE EMISSIONS FROM NATURAL GAS-FIRED POWER PLANTS

3.1 Motivation for Research

Natural gas (NG) usage has been growing since the large-scale implementation of hydraulic fracturing and horizontal drilling technologies to take advantage of shale resources [60, 61]. Along with market factors and stricter environmental regulations, this has led to a near doubling of the U.S. electricity generation from NG since 2008, with electricity generation matching or surpassing that of coal since 2016 [62] as shown in Figure 3.1. NG offers improved efficiency and availability and only produces 56% the amount of carbon dioxide (CO_2) per unit energy as coal, making it a potential "bridge fuel" in the transition toward renewable energy [63]. However, NG is primarily composed of methane (CH_4), the second most important anthropogenic greenhouse gas (GHG) accounting for 9% of all U.S. GHG emissions in 2017 [64, 65] based on its 100-year Global Warming Potential (GWP) (calculations are detailed in the SI). CH_4 is also a short-lived gas (12.4 years [7]) with a GWP of 84 over a 20-year period compared to a GWP of 28 over a 100-year period [66]. These GWPs can also be used to converted CH_4 (or any other GHG) to an equivalent amount of CO_2 that would result in the same warming potential, or $CO_{2_{eq}}$. When using the 20-year GWP, CH_4 emissions are equivalent to 22% of annual U.S. GHG emissions. The short-term impact of reducing CH_4 emissions makes it an important focus of climate change mitigation efforts.

Over 50% of global CH_4 emissions are related to human activity, and losses from the energy sector are the largest anthropogenic source in the U.S. [21]. On the basis of

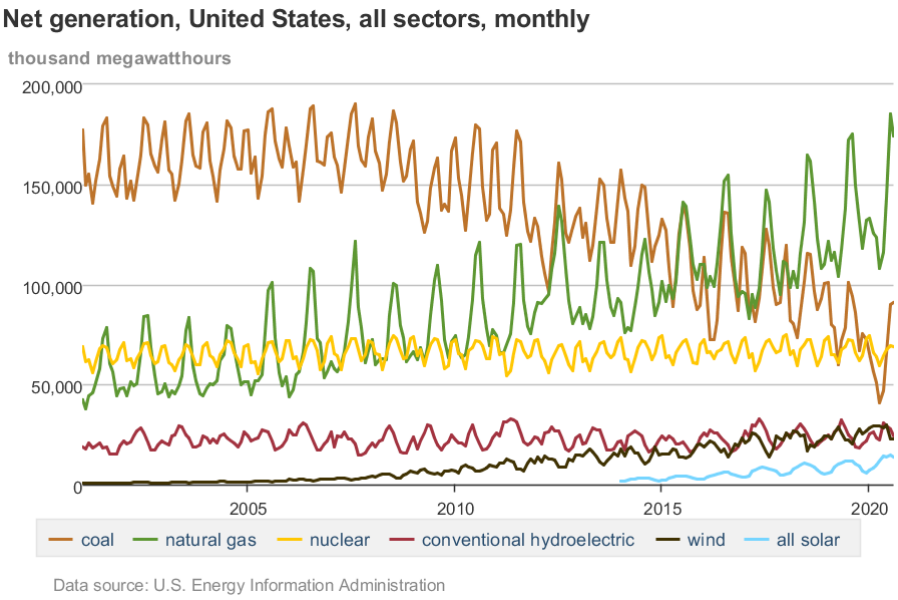

Figure 3.1. Net power generation in the U.S. across the primary sources. NG production begins surpassing coal in 2015-2016. Figure from the EIA electricity data browser. [62]

a recent synthesis of CH_4 emissions from well to end user, Alvarez et al. [22] estimated that 2.3% of U.S. gross production of NG is emitted to the atmosphere. At this loss rate, supply chain CH_4 emissions nearly double the short-term climate impact of the combustion of NG for energy. Therefore, quantifying losses along the NG supply chain from production to end use is essential. To realize the climate benefit of NG, it must be efficiently handled and combusted.

There have been multiple studies focused on the production, storage, and processing of NG, but there has been little work on end users, such as natural gas-fired power plants (NGPP) [22, 44, 48, 67–77]. Lavoie et al. [73] studied three NGPPs and saw emissions of unburned CH_4 from the stacks and relatively large CH_4 leaks attributed to non-stack sources on-site. The Lavoie et al. study was based on a small sample size of 3 combined cycle power plants (CC). CC facilities use the combustion gases to turn a turbine and then use the excess heat in these gases to generate steam

to turn a second turbine as shown in Figure 3.2. CC plants are the most efficient NGPPs, producing 46% more energy per energy content of fuel consumed than a simple combustion turbine [78]. Because of this higher efficiency, CC facilities are the most common type of NGPP, providing 89% of the electricity produced by NG [79]. As such, we focus largely on CC NGPP emissions in this study.

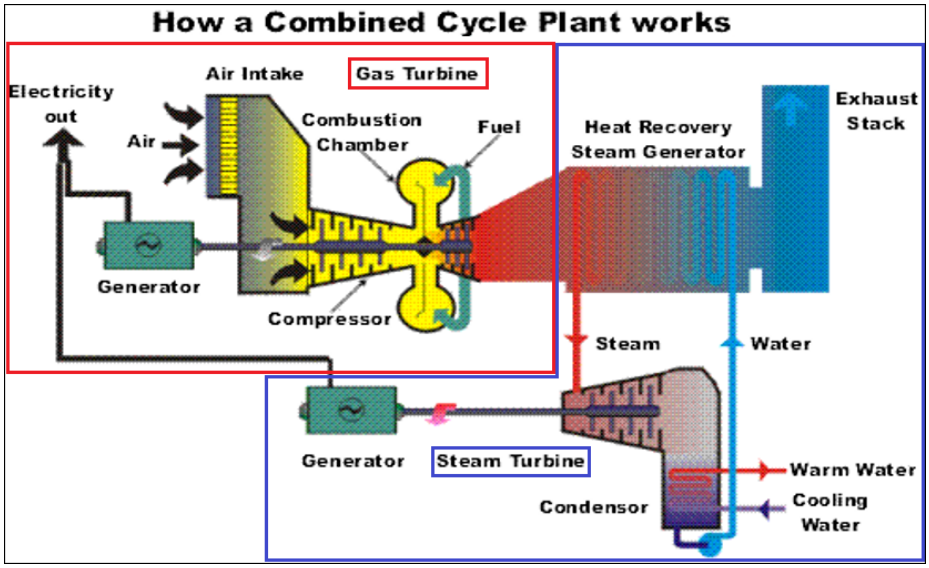

Figure 3.2. Simple diagram of how a CC power plant works. The red region highlights the gas turbine, or combustion turbine, portion of the diagram while the blue region highlights the steam turbine, or simple thermal, portion.

We expand on the work of Lavoie et al. by sampling a larger set of NGPPs to thoroughly investigate the prevalence of on-site CH_4 leaks and to gather more robust emissions data to compare to the Environmental Protection Agency (EPA) estimates. We studied 14 NGPPs, but only 5 showed downwind ΔCH_4, while all showed ΔCO_2 downwind. This suggests CH_4 emissions were too low to be detected above atmospheric variability at most NGPPs. This work focuses on the 5 NGPPs that showed downwind ΔCH_4. We calculate $\Delta CH_4/\Delta CO_2$ (ppm/ppm) ratios when flying through the stack emission plumes with/against the mean wind direction or circling near the stacks. We quantify the facility (non-stack) CH_4 leaks by comparing this to the same

ratio from downwind aircraft-based mass balance experiments (MBE), which would capture all plant emissions.

Although the EPA calculates CH_4 emissions from NGPPs, it does so using emission factors (EF) that have not been well-tested and may underestimate emissions based on previous work in the NG sector [61,67,68,73]. The EPA requires that facilities report hourly averaged CO_2 emissions through the Air Markets Program Data (AMPD) using Continuous Emissions Monitoring Systems (CEMS) as described in Title 42 of the U.S. Code of Federal Regulations [79, 80]. As for CH_4, the Greenhouse Gas Reporting Program (GHGRP), a reporting program for GHG point sources, uses an EF of 1 g CH_4 per million British thermal units (MMBTU) for all NGPPs based on the Intergovernmental Panel on Climate Change (IPCC) recommendations [80–82]. The Greenhouse Gas Inventory (GHGI), a comprehensive bottom-up inventory used to estimate national emissions by source category, instead uses an EF of 3.9 g CH_4/MMBTU for CC and combustion turbine NGPPs based on both the IPCC and the EPA's Compilation of Air Pollutant Emission Factors (AP-42) [83–85]. In this work, we present statistically meaningful results from 5 NGPPs and discuss the magnitude and variability of stack emissions. Chapter 4 investigates the measured CO_2 emission rates (ERs) as compared to AMPD reported CO_2 ERs.

3.2 Materials and Methods

3.2.1 Instrumentation

Flights were conducted using Purdue's Airborne Laboratory for Atmospheric Research (ALAR) [44, 49–51, 86], which is a modified twin-engine Beechcraft Duchess aircraft. ALAR is outfitted with a global positioning and inertial navigation system, a Best Air Turbulence probe for high precision 3-dimensional wind measurements [87], and a model G2301-m Picarro Cavity Ring Down Spectrometer designed for 0.5 Hz airborne measurements of CO_2, CH_4, and H_2O [88]. We conducted multiple three-point calibrations each flight using NOAA-certified standard cylinders containing CO_2

and CH_4, with concentrations that bracket the range of typical observations. A direct absorption ethane (C_2H_6) spectrometer designed by Aerodyne Research and modified at Harvard University was added to ALAR for a subset of flights.

3.2.2 Flight Design and Site Selection

We conducted a total of 23 flights at 14 NGPPs to quantify NGPP CH_4 emissions. Combined, these plants represent 3.4% and 1.5% of NG and total U.S. nameplate capacity, respectively [89]. A principal goal of this study was to produce a representative data set; thus, NGPPs were chosen to include a variety of regions, firing methods, maximum capacities, ages, and operation types, as shown in Table 3.1 [73]. These NGPPs are relatively new, but this is to be expected as ∼70% of NGPP capacity comes from units ≤20 years old [78]. Operation type refers to a unit's typical generation and is defined here as baseload units operating >70% of the year, intermediate units operating 30 - 70%, and peaking units operating <30% of the year based on AMPD data [79].

We performed MBEs during each flight to quantify ERs and stack measurements of $\Delta CH_4/\Delta CO_2$ ratios. Flights also included either a circle around the NGPP or an upwind horizontal transect to determine if other sources could influence downwind measurements. MBEs were conducted by flying multiple horizontal transects, typically in 250 ft intervals, at a fixed distance (∼3 km) downwind of the site from as low to the ground as is safe to the highest altitude where emissions could be seen, often with a vertical spiral through the downwind plume (see Figure 2.10 in Chapter 2). The transects extend sufficiently beyond the edges of the plume so that GHG concentrations return to background concentrations. A standard linear regression is fit through this background concentration to estimate the transect's background [52].

Low wind conditions increase the ER uncertainty as transects are less likely to capture all emissions with meandering winds, so several flights use the stacked closed-path method discussed by Conley et al. [55] to obtain an ER, as it is more likely to

Table 3.1.
Key Parameters Describing the NGPPs Studied[a]

ID	state	firing method	max capacity (MW)	operation type	commercial operating date
P1	UT	combined cycle	560	intermediate	2005
P2	UT	combined cycle	1180	intermediate	2007, 2014
P3	IL	combined cycle	1310	baseload	2002
P4	IL	combined cycle	680	peaking	2002
P5	IN	combined cycle	730	baseload	2002
P6	FL	combined cycle	3530	baseload	2009, 2011
P7	FL	simple thermal	1070	baseload	2013
P8	FL	combined cycle	1190	baseload	2014
P9	FL	combustion turbine	790	intermediate	2002
P10	FL	50% combined cycle, 50% combustion turbine	2100	intermediate	2003, 2009
P11	OH	combined cycle	760	baseload	2012
P12	OH	combined cycle	590	baseload	2012
P13	OH	combined cycle	940	baseload	2003
P14	MI	50% combined cycle, 50% combustion turbine	1000	baseload	2001, 2002

[a]Operation types are based on the most active units (e.g., a plant with 1 baseload and 3 intermediate units is labeled baseload). Maximum capacities are calculated from the maximum hourly heat input from AMPD [79], and the heat rate from the U.S. Energy Information Administration [78]. Commercial operating dates are from AMPD data and news articles for the plants. Multiple years are listed when additional units were added, and conversion dates are used if plants were converted to gas.

capture all emissions in such conditions. The uncertainty estimates for this method are described in detail by Conley et al. [55] and include uncertainties associated with wind speed and direction, precision of the chemical species monitor, and the circle-to-circle variability in calculated horizontal fluxes, caused by stochastic turbulence.

3.2.3 Calculation of Stack ERs

To quantify the impact of non-stack emissions, stack $\Delta CH_4/\Delta CO_2$ ratios are multiplied by the measured CO_2 ER to calculate a theoretical CH_4 ER (stack ER, in kg/hr) according to Equation 3.1. Stack ratios were calculated in a similar manner to previous studies [73, 90, 91]. Any MBE ERs that are substantially greater than the stack ER would indicate potential facility-scale CH_4 leaks. Briefly, Lavoie et al. [73] manually defined the bounds of stack plumes using CO_2 measurements, used a 2-point linear regression about these bounds to calculate a background, then subtracted the background to retrieve ΔCO_2 and ΔCH_4. Lastly a standard linear regression forced through zero was applied for ΔCH_4 vs. ΔCO_2 and the slope was considered the stack ratio. Although the method is similar, some aspects of the calculation have changed in this work.

$$\text{average stack ratio} \times \text{MBE } CO_2 \text{ ER} \times \text{mol wt. ratio} \left(\frac{16}{44}\right) = \text{stack } CH_4 \text{ ER} \quad (3.1)$$

One of the more significant changes is that we no longer manually define the bounds of stack plumes, but instead have automated the process. For CO_2, a 2-minute rolling average and standard deviation of the data during stack measurements is calculated with at least 1 minute of background data for initialization. This is calculated point-wise and any datum which is 5σ larger than the rolling average of the previous point is considered a stack plume and not incorporated into the rolling average. Only these points, which are 5σ larger than the rolling average, are considered stack signals and used in stack analyses. To avoid incorporating minor nearby CO_2 signals (e.g. brush fires or small emitters in an urban environment) into the rolling average, any

data 3σ larger than the rolling average is considered a non-stack signal and excluded from the rolling average, but not used in stack analyses. CO_2 plume bounds are then defined as the nearest point at which there are 5 consecutive concentrations within 2σ of the point-wise rolling average. CO_2 backgrounds are then calculated as a standard linear regression of these 5 points on either end of the plume. The same points in CH_4 are used to calculate a background for the CH_4 data. The result of this process can be seen in Figure 3.3A. The location of each plume is also plotted using an online tool [92] to ensure only samples downwind/over the stacks are included, as shown in Figure 3.3B. In a small number of cases where large CH_4 plumes were seen, the CH_4 bounds were manually adjusted due to a slight mismatch between the bounds of CO_2 plumes and CH_4 plumes.

In addition to automating the calculation of stack enhancements, we have made some changes to the calculation methodology, and to how the stack ratios are used. We account for the dilution effects of CO_2 on the measured CH_4 concentrations given such large stack CO_2 signals (>1,000 ppm), although we note that the effect is small at only 0.1 ppb for a 1,500 ppm ΔCO_2 and 70 ppb ΔCH_4. We are also not using a simple linear regression for the ΔCH_4 vs. ΔCO_2 regression of each sample, but instead an orthogonal distance regression (ODR) forced through 0. This type of regression accounts for errors in both the x and y data, but requires that both species have equal measurement error standard deviations [94]. This is not the case for these 2 species, but Igor Pro [95], used for most analyses in this work, allows for a variation of ODR with user-defined measurement error standard deviations, i.e. not true ODR fitting [96]. Lastly, Lavoie et al. [73] aggregated stack data to calculate a daily stack ratio for each NGPP, whereas we are treating each plume as a separate sample and averaging the ratios to get a daily stack ratio, due to the large variability across short timescales, the study of which is one objective of this work.

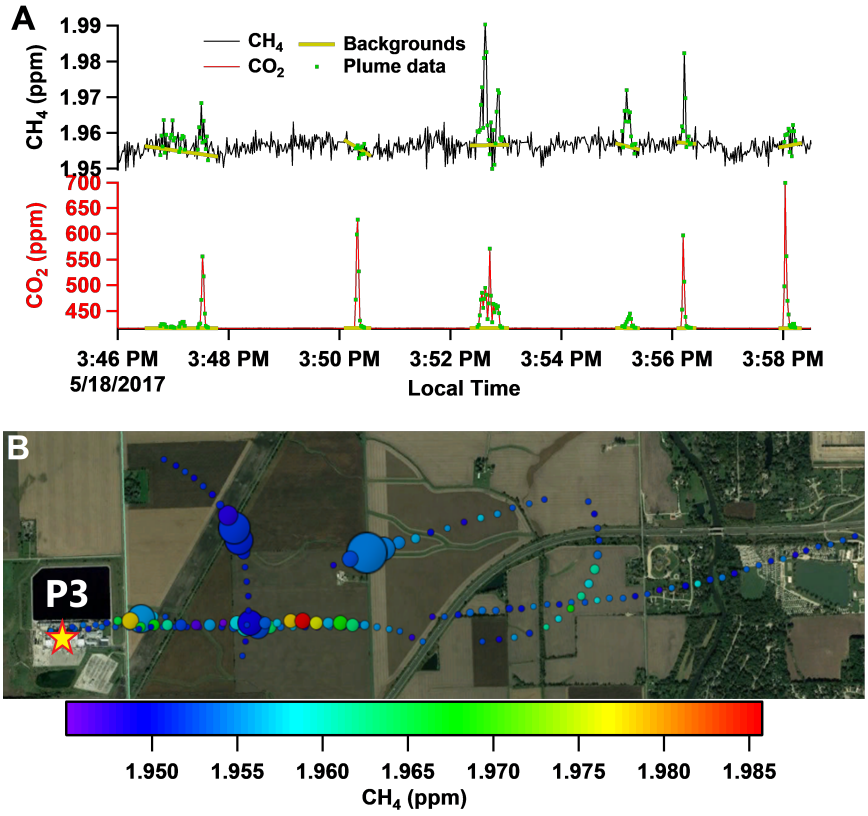

Figure 3.3. A) Stack measurements at P3 on 5/18/2017 with key features for calculating the stack enhancements shown. B) Location of the plumes in Google Earth [93] color scaled by CH_4 and size scaled by CO_2 with the power plant labeled. These plots were used to visually verify the power plant as the likely source before using any stack data. Map Data from Google.

3.2.4 Calculation of EFs

A recent life cycle analysis of the NG supply chain estimated the current supply chain loss rate at 2.3% of U.S. gross production, ∼60% larger than EPA estimates [22]. However, the study authors were unable to update local distribution and end user emissions due to insufficient information. To help address this lack of information, we have also calculated loss rates for our end user data using Equations 3.2 and 3.3. Equation 3.2 shows the calculation of the CH_4 throughput using the AMPD reported heat input, the density of NG, the heat content of NG [97, 98], and the assumption that NG is 95% CH_4 [99]. Equation 3.3 shows the calculation of loss rates, and Equation 3.4 shows the calculation of the throughput-based EF. Both calculations rely on a theoretical CH_4 ER (AMPD stack ER) calculated according to Equation 3.1 using the AMPD CO_2 ER instead of the MBE CO_2 ER to avoid incorporating any potential biases of the MBE ERs.

$$\text{throughput}\left(\text{kg}\frac{\text{CH}_4}{\text{hr}}\right) = \text{heat input}\left(\frac{\text{MMBTU}}{\text{hr}}\right) \times \frac{1\text{ MCF}}{1.033\text{ MMBTU}} \times \frac{18.9\text{ kg CH}_4}{1\text{ MCF}} \times 0.95 \tag{3.2}$$

$$\text{loss rate (\%)} = \frac{\text{AMPD stack ER}\ \left(\text{kg}\frac{\text{CH}_4}{\text{hr}}\right)}{\text{throughput}\left(\text{kg}\frac{\text{CH}_4}{\text{hr}}\right)} \times 100 \tag{3.3}$$

$$\text{EF}\left(\frac{\text{g}}{\text{MMBTU}}\right) = \frac{\text{AMPD stack ER}\left(\text{g}\frac{\text{CH}_4}{\text{hr}}\right)}{\text{heat input}\ \left(\frac{\text{MMBTU}}{\text{hr}}\right)} \tag{3.4}$$

3.3 Results and Discussion

3.3.1 Analysis of Stack Emissions

Although all flights showed ΔCO_2, only 5 of the 14 NGPPs examined showed ΔCH_4 above atmospheric variability in the downwind transects, consisting of 10 flights and 15 MBEs. Each flight's meteorological conditions are described in Table 3.2. P6 was successfully sampled on 11/12/2016, 11/13/2016, and 11/19/2016. P3, previously

sampled by Lavoie et al., [73] was sampled on three separate occasions, but the third (7/24/17) showed evidence of an intermittent source upwind of the plant and has thus not been used for MBE ER quantification. P2, also sampled by Lavoie et al., [73] was sampled on 10/12/2017 and 10/13/2017, but the 10/12 flight has been considered unusable as poor plume capture would make uncertainties in the MBE ERs large. P8 was sampled on 11/14/2016 and 11/17/2016, and P4 was sampled on 6/14/2017, 6/21/2017, and 7/24/2017, although we were unable to measure stack plumes on 6/21/2017. However, the flight at P6 on 11/12/2016, one of the MBEs at P3 on 5/18/2017, and the flight at P4 on 6/14/2017 all showed no downwind ΔCH_4.

We used Equation 3.1 to compare stack ERs to downwind MBE ERs and found no statistically significant difference. MBE ERs calculated according to Equation 2.4, stack ratios, and stack ERs calculated according to Equation 3.1 are provided in Table 3.3. In all cases, there is agreement within uncertainty between stack ERs and MBE ERs, although many flights exhibit large variability in stack ratios leading to large uncertainties in stack ERs. This suggests that all CH_4 emissions measured were uncombusted fuel CH_4. The component and final uncertainties for all MBE data is shown in Table 3.4.

Our flights have shown highly variable $\Delta CH_4/\Delta CO_2$ stack ratios for individual power plants even over the short time scale from one pass over the stack to the next. The flight at P3 on 5/18/2017 included significant stack measurements to investigate the extent to which CH_4 emissions were from the stack as compared to equipment on-site, and to more thoroughly investigate the high variability in $\Delta CH_4/\Delta CO_2$ stack ratios. Figure 3.4 highlights the temporal variability in unburned CH_4 observed in the stack emissions for P3, covering just one 13 min window. In that 13 min period, the slopes spanned a range of $\sim$25, not including the one case with a negative slope (discussed below). The data plotted in Figure 3.4 represents $\Delta CH_4/\Delta CO_2$ for short-term simultaneous spikes in CH_4 and CO_2, which are background-subtracted using a linear regression through the data immediately pre- and post-plume as shown in Figure 3.3. Thus, we believe the observed variability is not influenced by variability

Table 3.2.
Conditions and Date of Each Mass Balance Flight[a]

ID	date (MM/DD/YY)	time (local)	wind direction (deg)	wind speed (m/s)	flight method
P6	11/12/16	13:50 – 15:40	145 ± 70	2 ± 1	DT[d]
P6	11/13/16	14:35 – 15:33	130 ± 10	4.1 ± 0.9	DT
P6	11/19/16	13:14 – 15:14	335 ± 30	4 ± 2	DT
P8	11/14/16	14:05 – 14:50	250 ± 10	3.2 ± 0.7	DT
P8	11/17/16	13:12 – 14:19	38 ± 8	8 ± 2	DT
P4	6/14/17	12:40 – 13:11	220 ± 13	7 ± 1	spiral[d]
P4	6/21/17	14:50 – 15:40	250 ± 20	4 ± 1	spiral
P4	7/24/17	16:05 – 17:26	50 ± 10	4.2 ± 0.9	DT
P3	5/18/17	13:46 – 15:44	260 ± 10	13 ± 3	DT
P3	7/7/17	14:40 – 15:16	340 ± 10	11 ± 1	DT
P3	7/24/17	12:01 – 13:38	30 ± 20	5.5 ± 2	DT[e]
P2	10/12/17[c]	13:26 – 13:53	290 ± 50	2 ± 1	DT[f]
P2	10/13/17[c]	12:23 – 12:51	NA[b]	3[b]	spiral

[a]Uncertainties are 1σ. DT = downwind transects.

[b]Complex wind conditions with some evidence of winds being driven by a lake-breeze effect [100].

[c]AMPD data shows the facility to be in startup, having begun producing within the past 4 hr.

[d]CH_4 emission were too low to be quantified.

[e]Emissions cannot be quantified because of contamination from an upwind source.

[f]Emissions could not be quantified due to incomplete plume capture downwind.

Table 3.3.
MBE ERs, Stack Ratios, and Stack ERs[a]

ID	date	average stack ratio (CH_4/CO_2, mol/mol)	CH_4 MBE ER (kg/hr)(eq 2.4)	CH_4 stack ER (kg/hr)(eq 3.1)
P6	11/12/16	-3 ($\pm$7) $\times$ 10^{-4}	NA[b]	-70 $\pm$ 150
			NA[b]	-60 $\pm$ 120
P6	11/13/16	2 ($\pm$1) $\times$ 10^{-4}	74 $\pm$ 15	53 $\pm$ 36
			71 $\pm$ 18	46 $\pm$ 32
P6	11/19/16	1 ($\pm$3) $\times$ 10^{-4}	89 $\pm$ 20	30 $\pm$ 96
			135 $\pm$ 27	40 $\pm$ 140
P8	11/14/16	2 ($\pm$1) $\times$ 10^{-4}	56 $\pm$ 22	21 $\pm$ 16
P8	11/17/16	3 ($\pm$3) $\times$ 10^{-4}	8 $\pm$ 5	21 $\pm$ 13
			13 $\pm$ 5	16 $\pm$ 14
P4	6/14/17	-0.7 ($\pm$6) $\times$ 10^{-5}	NA[b]	-0.5 $\pm$ 4
P4	6/21/17	NA	80 $\pm$ 30	NA
P4	7/24/17	1.8 ($\pm$0.4) $\times$ 10^{-3}	113 $\pm$ 22	99 $\pm$ 29
			42 $\pm$ 12	91 $\pm$ 28
P3	5/18/17	3 ($\pm$2) $\times$ 10^{-4}	NA[b]	22 $\pm$ 17
			15.6 $\pm$ 8.6	24 $\pm$ 18
P3	7/7/17	3 ($\pm$3) $\times$ 10^{-4}	36.6 $\pm$ 7.5	70 $\pm$ 78
P2	10/13/17	2 (+3/-2) $\times$ 10^{-2}	22 $\pm$ 47	350 + 660/-350

[a]All uncertainties are 1σ. Uncertainty lower limits are set to 0 for P2 as stack data were highly variable but consistently positive.

[b]CH_4 emissions were too low to quantify.

Table 3.4.
Summary of Each Component of the Uncertainty in the ER for Transect MBEs

Date	Plant	$\frac{\delta_{U_\perp}}{U_\perp}$	$\frac{\delta_P}{P}$	$\frac{\delta_T}{T}$	$\frac{\delta_{Enh}}{Enh}$ CH_4	$\frac{\delta_{Flux}}{Flux}$ CH_4	$\frac{\delta_{Plume\ Capture}}{Plume\ Capture}$ CH_4	$\frac{\delta_{Krig}}{Krig}$	$\frac{\delta ER}{ER}$ CH_4	ER CH_4
11/13/16	P6	11%	2%	0.8%	6%	13%	6%	15%	**21%**	**74 ± 15**
11/13/16	P6	10%	2%	0.7%	5%	11%	18%	15%	**26%**	**71 ± 18**
11/19/16	P6	16%	2%	0.9%	4%	17%	3%	15%	**22%**	**89 ± 20**
11/19/16	P6	9%	2%	0.9%	4%	10%	8%	15%	**20%**	**135 ± 27**
11/14/16	P8	18%	2%	1%	3%	18%	31%	15%	**39%**	**56 ± 22**
11/17/16	P8	6%	2%	0.9%	47%	48%	45%	15%	**67%**	**8 ± 5**
11/17/16	P8	6%	2%	1%	33%	34%	4%	15%	**37%**	**13 ± 5**
7/24/17	P4	12%	2%	0.5%	2%	12%	1%	15%	**19%**	**113 ± 22**
7/24/17	P4	10%	2%	0.4%	7%	12%	20%	15%	**27%**	**42 ± 12**
5/18/17	P3	3%	4%	0.5%	120%	120%	6%	15%	**120%**	**-1 ± 1**
5/18/17	P3	4%	4%	0.6%	52%	53%	7%	15%	**55%**	**16 ± 9**
7/717	P3	4%	4%	0.4%	11%	13%	6%	15%	**20%**	**37 ± 7**

in background values. Each stack plume measured is regressed in a similar manner as in Figure 3.4, and the slope represents the $\Delta CH_4/\Delta CO_2$ ratio for that individual plume, hereafter referred to as a stack sample. Figure 3.5 shows a histogram of stack samples for P3 across three different flight days. For comparison, a histogram of all stack samples across all CC facilities is shown in Figure 3.6. The median corresponds to an unburned CH_4 fraction of 0.01% in Figure 3.6 compared to 0.024% in Figure 3.5. These highlight the high combustion efficiency of these plants, high enough that in some cases there is less CH_4 in the exhaust than in the intake air.

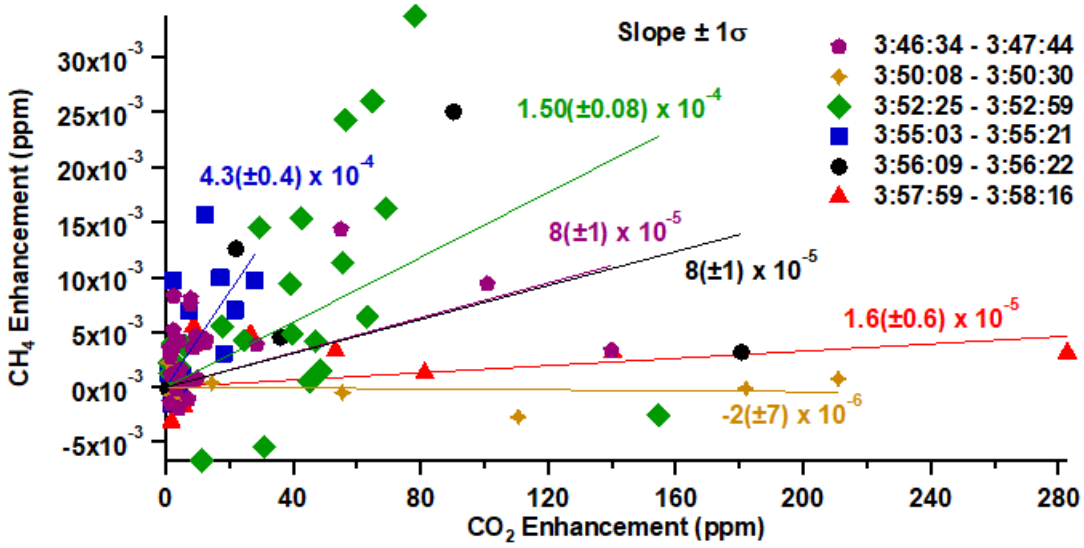

Figure 3.4. Stack samples from P3 measured from 3:46 to 3:59 local time on 5/18/2017. Each stack sample was measured by flying directly over the stacks with/against the mean winds. As such, some plumes were followed further downwind, up to a maximum distance of 5 km. The large variability in the slope, equivalent to the $\Delta CH_4/\Delta CO_2$ stack ratio, over short time scales can be seen. This leads to large uncertainties in the flight averaged stack ratios in many cases. That should not be confused with uncertainty in the individual slopes.

Unexpectedly, at a small number of facilities, we measured CH_4 depletions during stack sampling. Figure 3.7 shows an extreme case that we observed, and Figure 3.8 shows the regressions for multiple stack samples with statistically significant negative

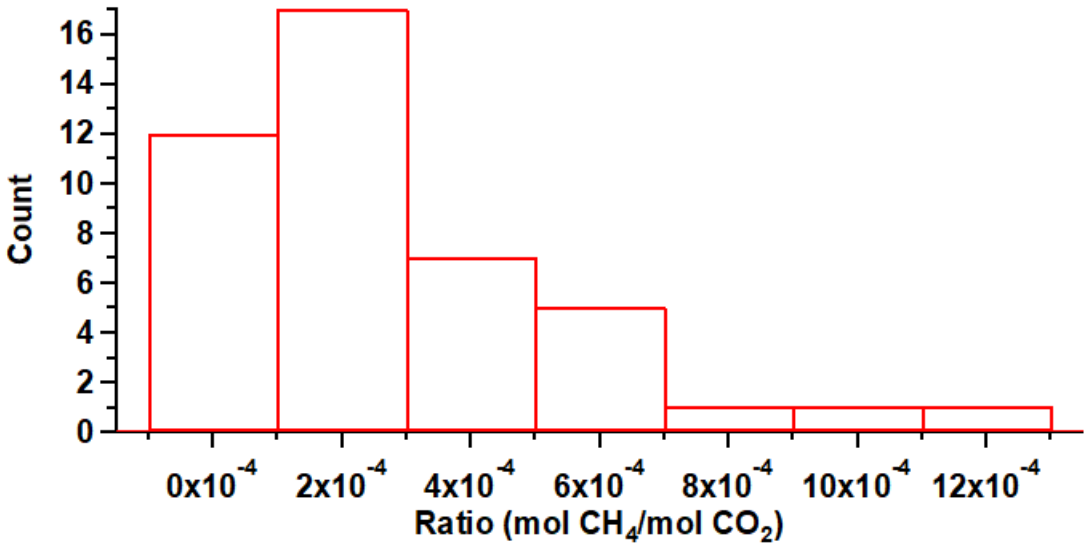

Figure 3.5. Histogram of all stack samples from P3 across all 3 flight days, excluding data with evidence of an upwind source on 7/24/17. N= 44, mean = 2.9×10^{-4}, and median = 2.4×10^{-4}.

slopes. Because such signals are then diluted and dispersed downwind, we have not observed any statistically significant depletions of CH_4 during downwind MBEs. We hypothesize that the most likely cause for this phenomenon is a highly efficient combustion process that consumes all fuel CH_4 and a small fraction of ambient CH_4 from the combustion turbine's intake air. A similar hypothesis was provided by Fischer et al. [76] when similar depletions were observed while studying household appliances. Although we collected C_2H_6 data for a small number of stack samples that showed CH_4 depletions, none show a clear ΔC_2H_6. One of the largest CH_4 depletions was 3.7% depleted relative to background. This would correspond to a 0.037 ppb theoretical C_2H_6 depletion from the 1 ppb background, assuming equal percent background depletion. This is within atmospheric variability and just above instrumental precision.

One NGPP (P2) exhibited large CH_4 emissions on two separate flights, both of which included C_2H_6 measurements. On 10/12/2017, there were no stack measure-

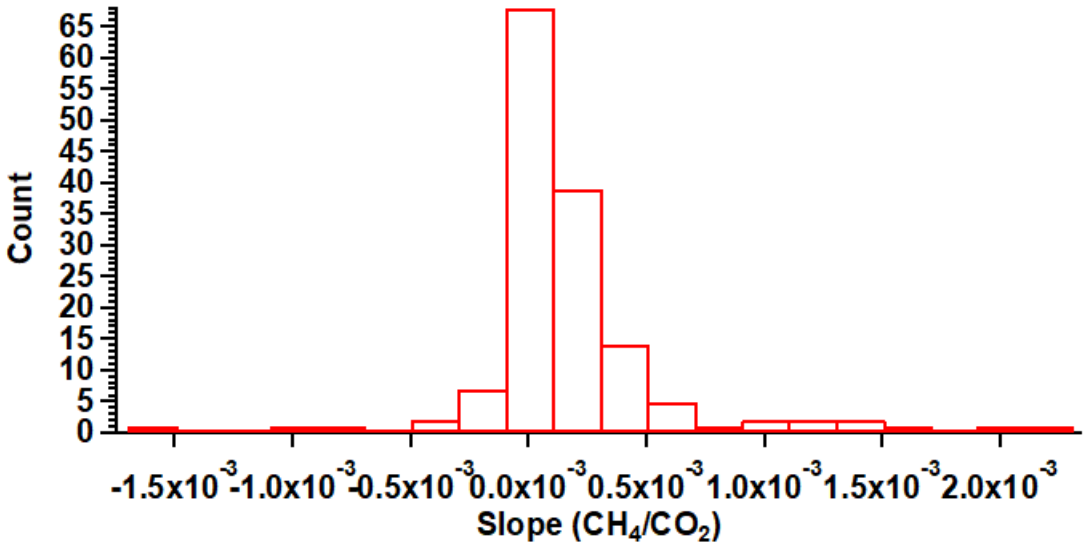

Figure 3.6. Histogram of all CC stack samples from all flights excluding P2 (discussed separately in Figure 3.9), including those without CH_4 enhancements and those with CH_4 depletions. N= 149, mean = 2×10^{-4}, and median = 1×10^{-4}. The majority of samples show a near 0 $\Delta CH_4/\Delta CO_2$ stack ratio highlighting the high combustion efficiency of these plants.

ments, and the vertical extent of the plume was not well captured; therefore, the flight could not be confidently used to calculate an MBE ER. However, the flight shows clear downwind ΔCH_4 and ΔC_2H_6 of up to 470 and 15 ppb, respectively, with ΔCO_2 of $\leq$2 ppm, which is much smaller than typically seen. The flight on 10/13/2017 showed stack $\Delta CH_4/\Delta CO_2$ ratios that were up to 3 orders of magnitude (to 13% indicated CH_4) larger than those observed at all other NGPPs, with concurrent emissions of CH_4, CO_2, and C_2H_6 throughout the flight, as shown in Figure 3.9A. Some stack samples even showed CH_4 and C_2H_6 concentrations above the dynamic range of the ethane analyzer but with CO_2 signals comparable to those observed at other facilities as shown in Figure 3.10. AMPD data for both P2 flights show that the facility was within 4 hr of starting up, suggesting these may be emissions associated with the startup condition. To ensure that all measured CH_4 was from NG

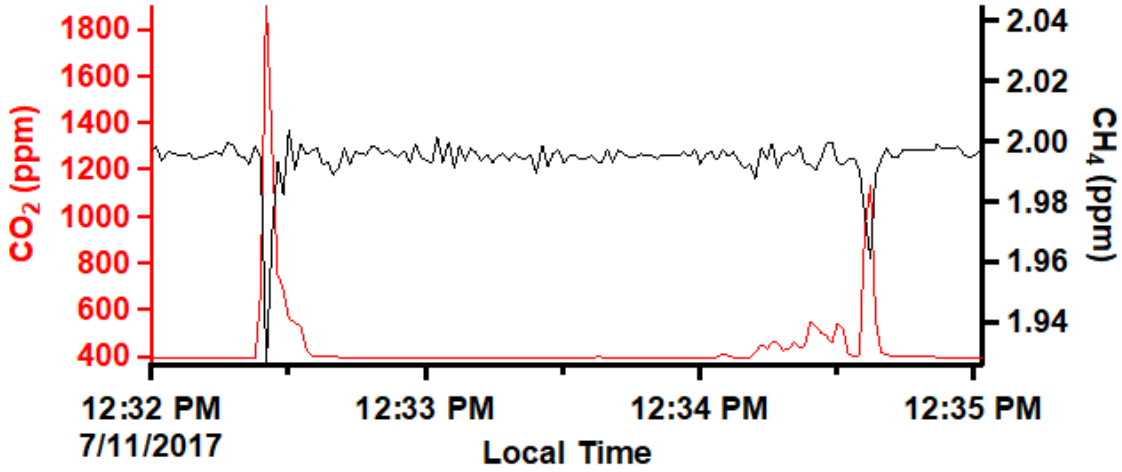

Figure 3.7. Example negative ΔCH_4 stack measurements from the 7/11/2017 flight at P12. We suggest that this represents partial consumption of intake air's background CH_4.

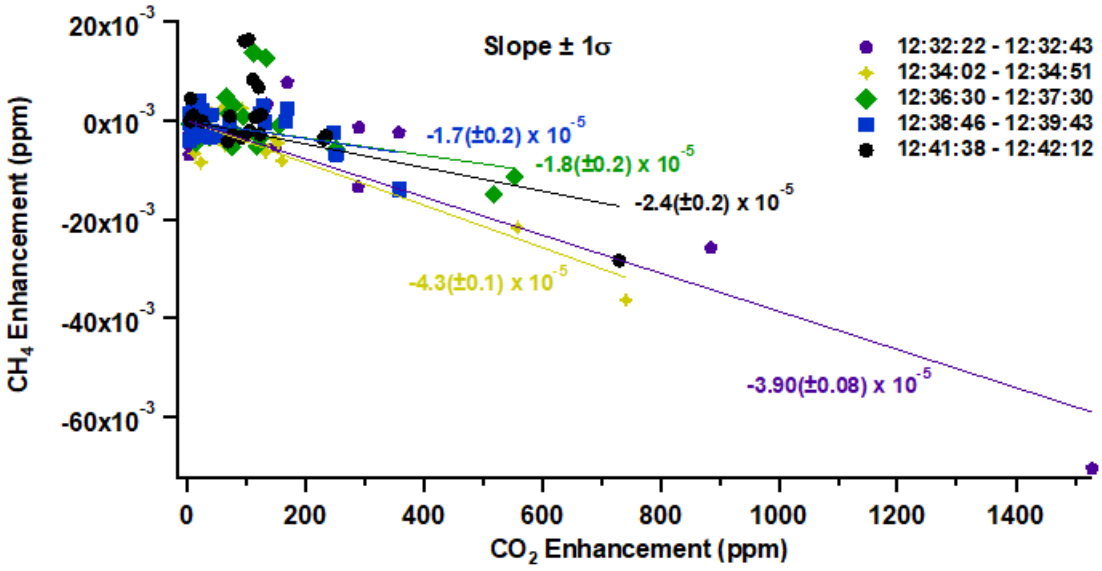

Figure 3.8. Stack samples on 7/11/2017 for P12 that show consistent anti-correlated ΔCH_4. This shows that the anti-correlation is consistent throughout the dips.

in this city environment we compared the $\Delta C_2H_6/\Delta CH_4$ ratio to pipeline reports in Figure 3.11. Both flights show a ratio ∼25% lower than pipeline data but also show a highly linear ΔC_2H_6 versus ΔCH_4 relationship as shown in Figures 3.9B and Figure 3.11, which suggests all emissions are from a thermogenic source. This discrepancy in $\Delta C_2H_6/\Delta CH_4$ may be caused by a combustion skew as the rate constant for CH_4 oxidation by OH radicals is ∼20% as large as that for the C_2H_6–OH reaction at 1600°C [99, 101].

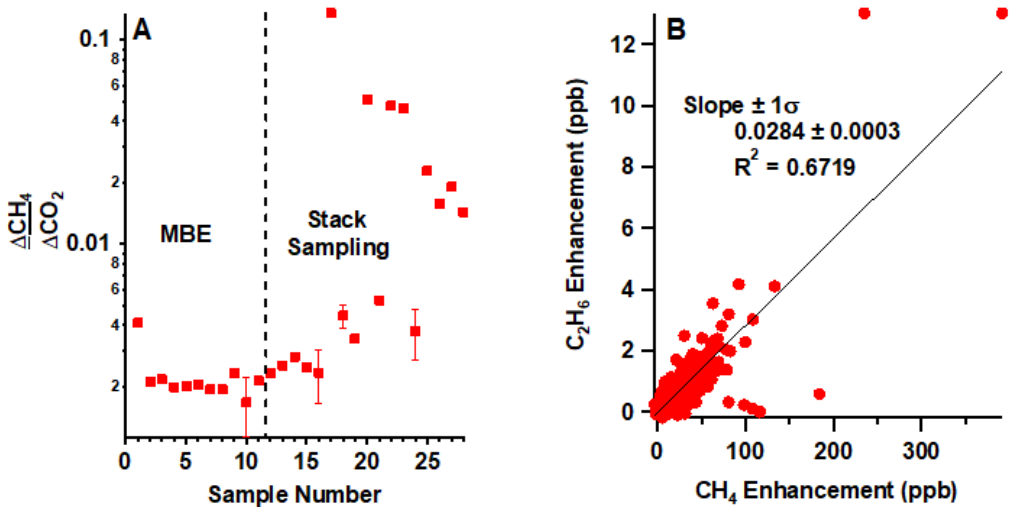

Figure 3.9. (A) Log scale showing the ratio of $\Delta CH_4/\Delta CO_2$ in each plume (both stack and MBE) from P2 on 10/13/2017. Samples 1–11 are from the MBE. These ratios are at least an order of magnitude larger than those seen at other facilities, although they are also much more variable. (B) Regression of ΔC_2H_6 versus ΔCH_4 for all plumes with usable C_2H_6 data for 10/13/2017. The linearity of the data suggests a single thermogenic source of CH_4.

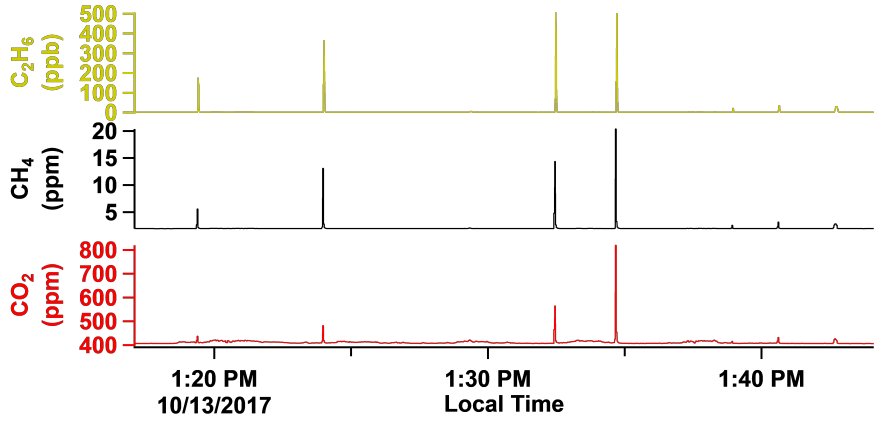

Figure 3.10. Large CH_4 and C_2H_6 signals observed when sampling the stacks of P2 on 10/13/2017. These show the largest magnitude emissions seen during the campaign. C_2H_6 data is not quantitative, as some peaks are above the dynamic range of the C_2H_6 analyzer.

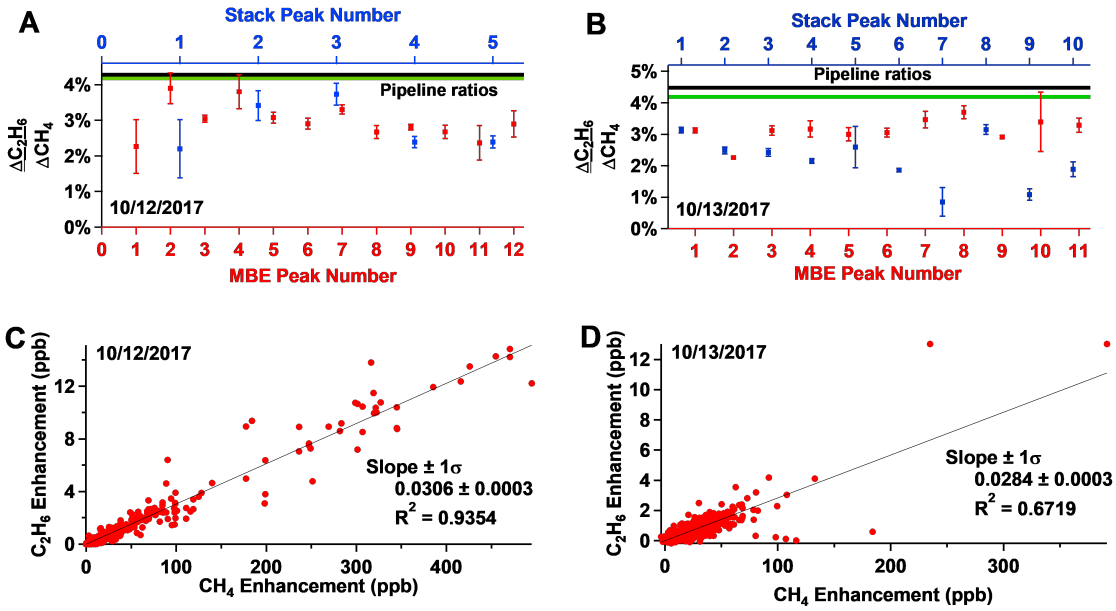

Figure 3.11. A) and B) show the $\Delta CH_4/\Delta C_2H_6$ ratio for each plume measured from P2 with pipeline ratios shown as black and green traces. The different axes/colors separate the plumes measured while flying directly in the stack plume from those measured while flying downwind transects. C) and D) show the regression of ΔC_2H_6 vs. ΔCH_4 across all plumes. Both flights show a strong linearity, suggesting a thermogenic source of CH_4 without a biogenic influence.

3.3.2 Natural Gas Power Plants as CH_4 Emitters

We used Equations 3.2–3.4 to convert the stack $\Delta CH_4/\Delta CO_2$ ratio into useful metrics in understanding NG leaks. The AMPD stack ERs, throughputs, loss rates, EFs, and reported AMPD CO_2 ERs are presented in Table 3.5. The EFs are directly compared to the EPA EFs of 1 g/MMBTU (GHGRP) and 3.9 g/MMBTU (GHGI) in Figure 3.12.

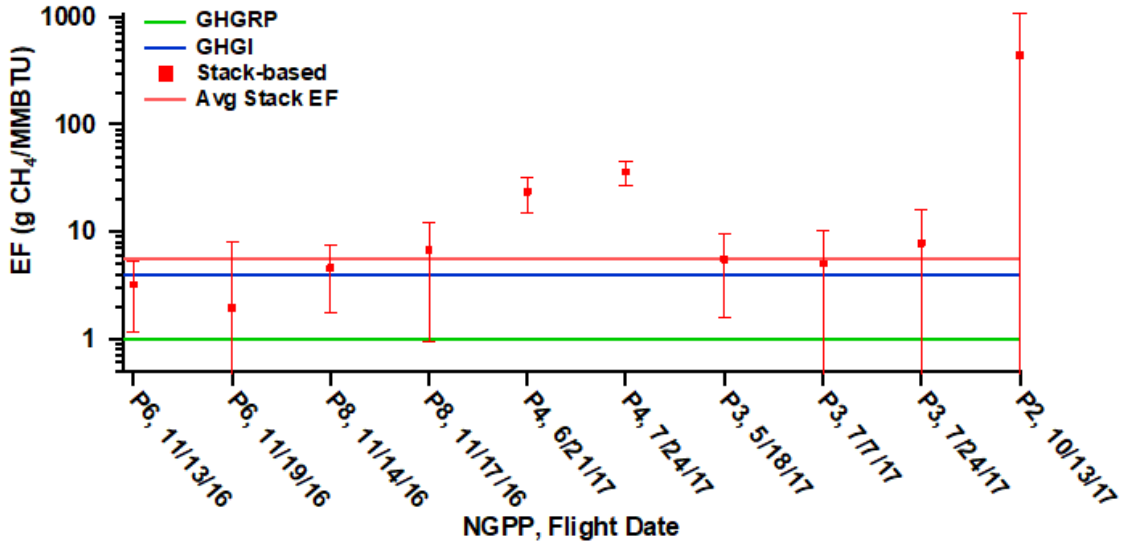

Figure 3.12. Log plot of EFs calculated from stack data from each flight. 1σ uncertainties are based on the variability across all stack samples that flight. The GHGRP and GHGI EFs of 1 g/MMBTU and 3.9 g/MMBTU respectively are shown for comparison. The average EF includes all CC stack data except for P2, regardless of downwind CH_4 emissions. Uncertainty bounds that are near or <0 are not shown. The measured EFs and the EPA EFs for most flights are statistically indistinguishable, with most EFs lying closer to the GHGI value, compared to the GHGRP value.

Although the average EF is consistent with EPA EFs, two plants show noticeably higher EFs (Table 3.5). P4, the only peaking facility studied, shows a slightly negative stack ratio for one flight and high stack ratios relative to the EPA EFs for the other two. The only other noteworthy aspect of P4 is the slightly lower load relative to

the maximum capacity which was ∼60% across all flights as compared to 70–80% at all other CH_4 emitting facilities, excluding P2. AMPD reported CO_2 ERs were similar across the three flights with 170 Mg/hr on 6/14 and 180 Mg/hr both other flight days. Including CC plants that did not show downwind ΔCH_4, but excluding P4 and P2, the average loss rate is 0.014 (+0.021/–0.014)% which is consistent with Lavoie et al. [73] who reported stack loss rates of 0.05 (±0.06)%. The average stack EF calculated using all CC stack data other than P2 is 5.4 (+10/–5.4) g/MMBTU. Because of the significant variability in stack samples (Figures 3.4 and 3.9) and to some degree cases with depleted CH_4 (Figures 3.7 and 3.8), propagated uncertainties are large, but we are representing them with a 0 lower limit given our data does not indicate negative emissions at the scales a symmetric uncertainty would suggest.

Even though several flights did not show significant CH_4 emissions downwind, they were still incorporated into the average loss rate and the average EF. For 4 flights, however, the stack samples showed no detectable CH_4 signal above background noise. These data are incorporated into the average stack EF but averaging in zero values would bias this estimate low as there is potentially CH_4 below our limit of detection (LOD). Instead, we have used an LOD-based method to calculate the stack $\Delta CH_4/\Delta CO_2$ ratio for these 4 flights. We calculate the CH_4 LOD as three times the 1σ variability of data during calibration tank runs, since we are interested in detecting enhancements. We use half this LOD to represent values below the LOD when calculating the average stack EF, as is common practice when averaging data near the LOD. To convert this CH_4 LOD to a stack $\Delta CH_4/\Delta CO_2$ ratio we divide by the average ΔCO_2 from all stack samples collected that day. As this ratio approaches infinity if the ΔCO_2 is small, a minimum stack plume signal of 20 ppm ΔCO_2 was defined. Any individual stack sample with a maximum ΔCO_2<20 ppm was excluded from this averaging while all data, regardless of magnitude, were included if the maximum ΔCO_2 during the stack sample was >20 ppm. Only a handful of samples were excluded using this criterion, however it did result in the exclusion of all stack data from P1 as the maximum ΔCO_2 across all stack samples was only 8 ppm. The

average stack EF excluding P2 is 5.4 (+10/-5.4) g CH_4/MMBTU. If we were to average in zeros in place of all 4 flights that were below the LOD the average EF excluding P2 is instead 4.9 (+9.9/-4.9) g CH_4/MMBTU.

P2 is the only facility measured during startup and it showed a substantially higher EF than other facilities, as shown in Figure 3.9A. As P2 is the only facility that was sampled during startup, we do not know if our observations are broadly representative of startup emissions. EPA's AP-42 [85] explains that EFs are based on efficient combustion under high operating conditions ($\geq$80% of max capacity) and that emissions during lower operating conditions or frequently changing loads such as startup are likely larger. If the large loss rate measured for P2 is common during startup it could have important implications for the climate benefits of NGPPs. Peaking facilities that are designed for faster startups and more flexible loads may show different startup emissions.

Our EFs were used to estimate annual national CH_4 emissions from CC NGPPs with and without accounting for the large startup emissions. To account for startup emissions, we calculated the average duration of startup across the CC plants studied (4 hr) and use this to calculate the heat input consumed during startup for all CC facilities in 2017 (3.519%). P2's EF was then applied to 3.519% of 2017 CC heat input [79] and the average stack EF of 5.4 (+10/–5.4) g/MMBTU was applied to the remainder. When incorporating startup emissions like this, we calculate 170 (+200/–170) Gg CH_4 emitted as uncombusted CH_4 compared to 44 (+81/–44) Gg without accounting for startup. On the basis of \$3.52/thousand ft^3 of NG [102], these emissions are equivalent to 9 (+16/–9) million dollars of CH_4 lost or 33 (+40/–33) million dollars if including startup losses. For comparison, CC NGPPs purchased 29.0 billion dollars' worth of NG CH_4 in 2017. The U.S. GHGI estimates 2016 CH_4 emissions from NG systems as 6.54 Tg. Therefore, emissions from NGPPs contribute in the range of 0.7–2.6% to the total CH_4 emissions from NG systems, depending strongly on the impact of startup conditions.

End users of NG, such as NGPPs, have been poorly studied and our work suggests that they could play a meaningful role in supply chain CH_4 emissions, particularly if the measured startup emissions are common. Although highly variable, startup emissions were up to several orders of magnitude larger than continuous operation emissions and warrant further study. Future work should also further investigate peaking NGPPs as they have more variable loads and startup more often but also more quickly. Additionally, shutdown emissions were not observed in this work but may show high emissions similar to startup given shutdown also involves quickly changing, low loads. Airborne measurements provided a useful snapshot of emissions in this work but continuous measurement systems like CEMS, given the variability seen, would likely prove more informative in the future. As such, cooperation with facilities is vital. Further improving our understanding of NGPP emissions will help fill a gap in the understanding of supply chain losses and could lead to changes in utility operations to minimize startup emissions.

Table 3.5.
Calculated Emissions Data Based on the Average Stack $\Delta CH_4/\Delta CO_2$ Ratio and AMPD Data[a]

ID	date	AMPD CO_2 ER (Mg/hr)	AMPD stack ER (kg CH_4/hr)	stack EF (g/MMBTU)	throughput (kg CH_4/hr)	loss rate (%)
P6	11/12/16	710 ± 100	-90 ± 180	-7 ± 13	230 000	-0.04 ± 0.08
P6	11/13/16	850 ± 120	51 ± 32	3.2 ± 2.0	275 000	0.018 ± 0.012
P6	11/19/16	970 ± 140	30 ± 110	1.9 ± 6.2	311 000	0.011 ± 0.035
P8	11/14/16	200 ± 30	17 ± 10	4.6 ± 2.8	64 000	0.026 ± 0.016
P8	11/17/16	240 ± 30	30 ± 26	6.6 ± 5.7	78 000	0.038 ± 0.033
P4	6/14/17	170 ± 20	-0.5 ± 4	-0.2 ± 1.2	54 000	-0.0009 ± 0.0067
P4	6/21/17	180 ± 20	NA	23.6 ± 8.4[b]	57 000	0.136 ± 0.048[b]
P4	7/24/17	180 ± 20	117 ± 31	35.5 ± 9.3	57 000	0.204 ± 0.054
P3	5/18/17	420 ± 60	43 ± 30	5.5 ± 3.9	136 000	0.031 ± 0.022
P3	7/7/17	440 ± 60	41 ± 43	5.0 ± 5.2	143 000	0.029 ± 0.030
P3	7/24/17	430 ± 60	63 ± 63	7.8 ± 7.9	138 000	0.045 ± 0.045
P2	10/13/17	62 ± 9	510 +760/–510	440 +660/–440	20 000	2.5 +3.8/–2.5

[a]Uncertainties represent 1σ based largely on the propagated uncertainty of the stack ratios. AMPD uncertainties are 14% based on the calculation discussed by Peischl et al. [75] All data shown other than for 6/21 is unrelated to the MBE ER data and as such unaffected by any potential biases in the MBE method.

[b]No stack data was collected for this flight, so the MBE ER was used as the numerator in Equations 3.3 and 3.4 instead. Propagated uncertainties include the MBE uncertainty instead of the variability of stack samples throughout the day for this flight.

4. ASSESSING THE ACCURACY AND PRECISION OF THE AIRBORNE MASS BALANCE TECHNIQUE FOR POINT-SOURCE EMISSIONS QUANTIFICATION

4.1 Motivation for Research

Urban GHG emissions and urbanization are both expected to continue to increase in coming years [103,104]. Accordingly, many cities have passed legislation or set goals for specific GHG reductions [105]. However, high precision monitoring techniques are necessary to act on this legislation or to quantify the impact of effective mitigation strategies. We have flown a large series of flights to assess the airborne MBE as a means to address this need. This technique has been used in point source [45, 55, 73, 106], regional [44, 48], and urban studies [45, 49–53, 56, 107] by multiple groups. Over the course of 5 years we performed >20 flights at >19 different power plants. Although many of these flights have been used in previous publications [73, 106], this work aims to use the large dataset to assess the airborne MBE technique as power plants are required to report CO_2 emissions to the EPA using CEMS. We quantify the accuracy using both a regression against CEMS measurements (slope=0.87) and the Mean Absolute Percent Error (MAPE) compared to CEMS (20%) and quantify the precision as the campaign averaged relative standard deviation from replicate MBEs (25%).

Airborne MBE techniques vary slightly across research groups, but few have directly assessed the capabilities of their technique against known emissions [45, 48, 55, 56]. To the authors' knowledge, only Conley et al. [55] and Ahn et al. [45] have directly assessed the method precision and/or accuracy against known emissions. Both

of these studies used a similar approach to calculate the accuracy of the quantification method, relying on power plant CEMS data as the "known" emission rate. We combine the uncertainty in the concentration and flow rate estimates in quadrature to estimate CEMS uncertainties at ±14% [75]. Conley et al. [55] estimated an MAPE of 10% based on 5 power plant flights and Ahn et al. [45] estimated an MAPE of 24% for 16 power plant MBEs and a precision of 19% based on 7 flights downwind of DC-Baltimore. The Conley et al. [55] approach is not suitable for regional or urban studies, however, as it requires flying many (20-25) stacked circles around the source of interest. The Ahn et al. [45] method is generally comparable to that used in this thesis, but the CBL is assumed well mixed. As such, there is no need to interpolate the downwind plume to a 2D grid. Instead, the authors can represent the entire CBL based on the flux from a single pass. However, they did not provide evidence that in fact, the CBL was always well-mixed.

4.2 Materials and Methods

4.2.1 Instrumentation

All flights were conducted using Purdue's Airborne Laboratory for Atmospheric Research (ALAR) [46, 49–51, 106] which is a modified twin-engine Beechcraft Duchess. ALAR is equipped with a Best Air Turbulence Probe for high precision 3-D wind field measurements [32, 33], a GPS/INS system, and a Picarro Cavity Ring Down Spectrometer designed for 0.5 Hz measurements of CO_2, CH_4, and H_2O [35]. Flights typically included two in-air three-point calibrations with World Meteorological Organization certified standard cylinders (WMO-CO2-X2007) ranging from 360 to 450 ppm CO_2, as described above.

4.2.2 Flight Design and MBE Method

Flights include between 1 and 4 MBEs at progressively further downwind distances to quantify the emission rate (ER). Multiple MBEs that were performed back to back are then used to assess the precision. MBEs were typically conducted by flying at multiple altitudes, typically in ∼250 ft intervals, at a fixed distance downwind of the site from as low to the ground as is safe to the highest altitude where emissions could be seen, often with a vertical spiral through the center of the plume. Transects extend sufficiently beyond the plume so that CO_2 concentrations return to background values. An ordinary least squares regression is fit through the background values on either end of the plume to estimate each transect's background [45, 46, 53, 73, 106]. The MBEs were typically within 5 km of the power plant, but those with more than 2 MBEs would go farther downwind, up to 13 km. This approach is broadly consistent with Chapter 3, except that all reported ERs are based on the average of a synthetic krig, three-pass average, and plume average approach to estimate emissions below the lowest flown transect as discussed in detail in Chapter 2 and shown in Figure 2.13. The uncertainty associated with the plume capture is also calculated as the variability across these three approaches. MBEs where the plumes were completely captured within the transect altitudes are instead reported as the transect only result and have a plume capture uncertainty of 0%. Figure 4.1 shows the impact that emissions below the lowest flown transect have by comparing the reported ER to that of the transect only approach.

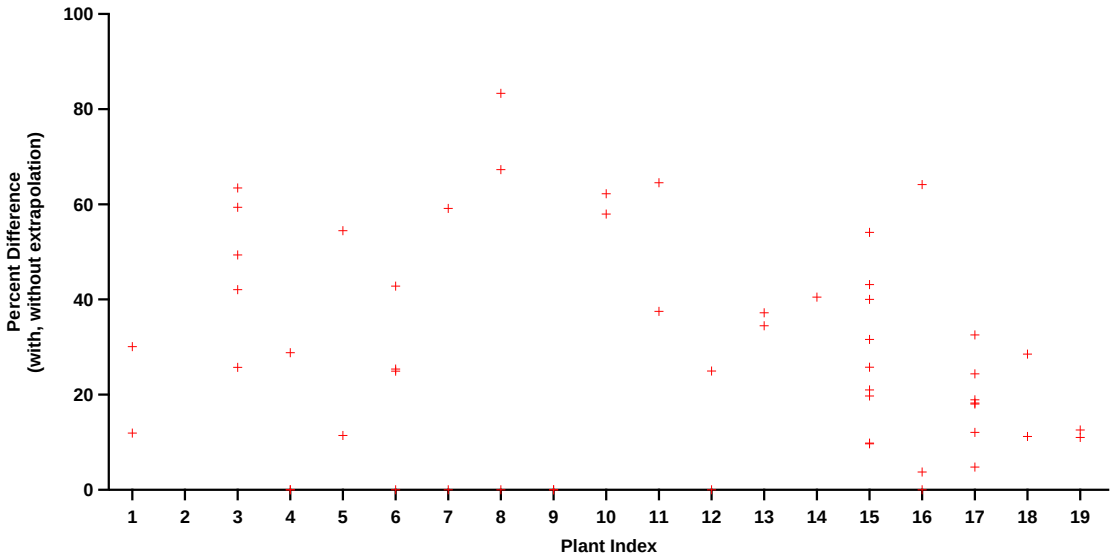

Figure 4.1. Percent difference between ERs calculated using only transect data and the reported ERs plotted against the plant index. The average is 28%, but excluding the cases of complete plume capture which have values of 0 the average is 34%. This represents the average impact that the emissions below the lowest transect flown have on the ER.

4.3 Results & Discussion

4.3.1 Accuracy

We calculate the accuracy of the MBE method using the CEMS data in two different approaches. In the first approach, we draw an ODR fit [96, 106], a type 2 regression that accounts for uncertainties in both axes, through the calculated 3-method average ERs plotted against the CEMS ERs, as shown in Figure 4.2. The calculated slope is slightly less than 1 at 0.923 ± 0.033, indicating that the measured ERs may slightly underestimate emissions. However we note that this slope is within our assumed uncertainty of the CEMS data. Although the four largest emission rates are significantly farther on the x-axis than any other facility and thus could be weighted more heavily by the fit, removing them has negligible impact on the slope. The reduced χ^2 statistic, a measure of the goodness of fit, for this regression is 1.702. A value >1 suggests that the error variances used in this fit are underestimated (i.e. either ER or CEMS uncertainties are not well defined).

Our second approach is to calculate the mean percent error (MPE) and mean absolute percent error (MAPE) from the individual MBEs as shown in Figure 4.3. The MAPE is 29% ± 32, but the median is only 17%, given that a small number of MBEs disagreed by a large margin. To address this we defined outliers as MBEs with a percent error that is more than 1.5 x the interquartile range (IQR, equal to the third quartile minus the first quartile) greater than the third quartile or less than the first quartile, known as Tukey Fences. This results in threshold values of $\sim\pm 66$ percent error. We removed the five MBEs that were beyond these bounds and repeated the above analyses. The slope of the regression between measured and CEMS ERs decreased to 0.871 (see Figure 4.4) and the reduced χ^2 statistic reduced to near 1. This suggests that the larger reduced χ^2 was driven primarily by the outliers and that these outliers offset a small amount of the MBE methods' low bias. The MAPE also decreases to 20% ± 13 while the median decreases slightly to 15%, suggesting there is still some skew in the distribution. Without outliers the data is also approximately

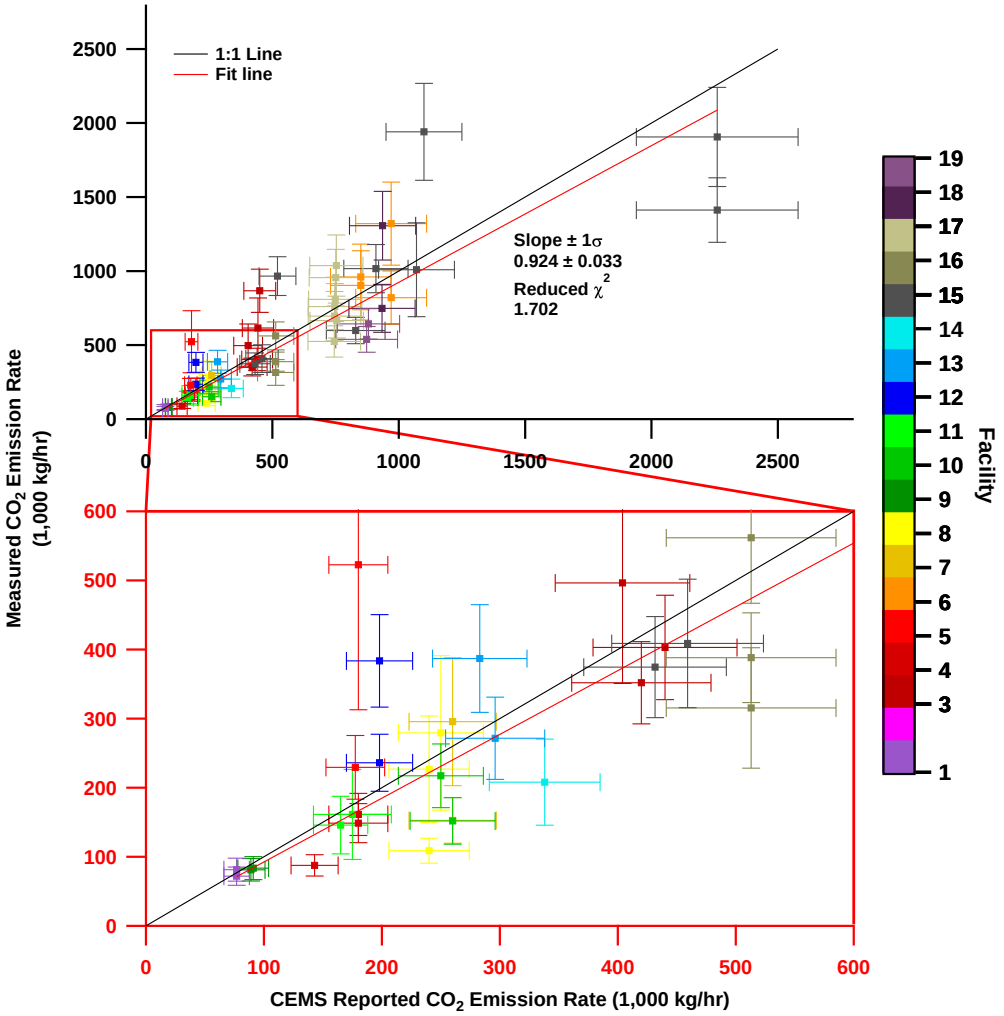

Figure 4.2. Measured ERs plotted against CEMS ERs, both in 1,000 kg/hr, with an inset of data between 0 and 600,000 kg/hr to more clearly see the large number of plants in this region.

normal, as expected if errors are random, with a Shapiro-Wilk test p-value of 0.13 as compared to a p-value of $2x10^{-6}$ when using all data. These distributions are shown in Figure 4.5.

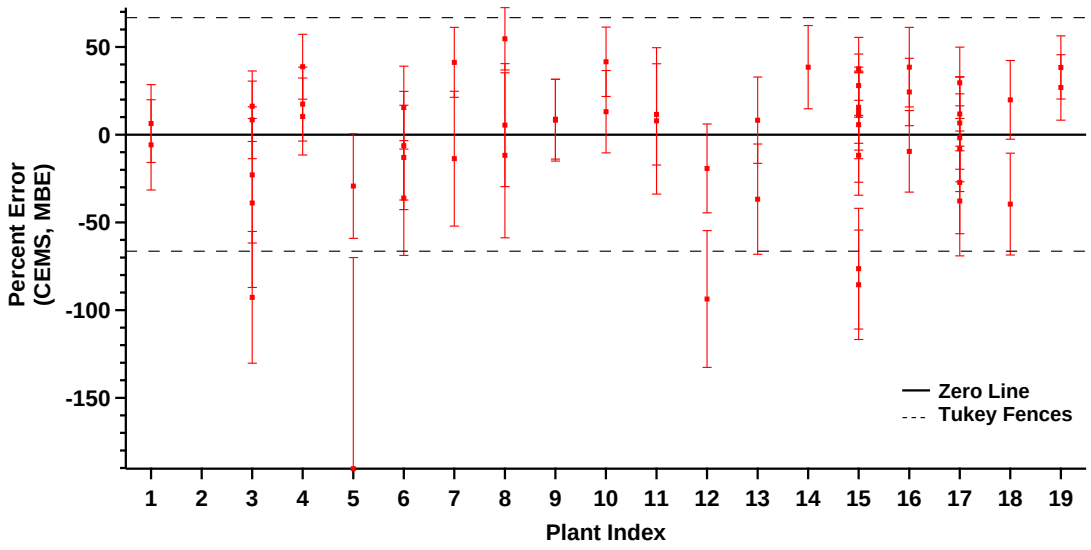

Figure 4.3. Percent error of the measured ERs as compared to CEMS plotted against the plant index. Negative values represent a larger measured ER while positive values represent a larger CEMS value. Tukey Fences used to identify outliers are also shown. Error bars represent the propagated errors.

Most of these outliers can be seen in Figure 4.6 as those with the shortest time from emission to measurement (transit time). Of the 5 outliers, 4 of them had transit times of 4 minutes or less. This parameter was chosen because of the relatively poor expected vertical and horizontal mixing of the plume with short transit times, making it more likely that the aircraft transect did not intersect the plume. This must be balanced with the higher signal to noise ratio measured when nearer to the source, even with large point sources like power plants. However, this does not explain the reason that all outliers overestimate the ERs, as "puff" type plumes (see Figure 1.2 from Chapter 1) that may occur close to a source, before emissions are relatively well-mixed vertically, would result in areas of high emissions as well as areas

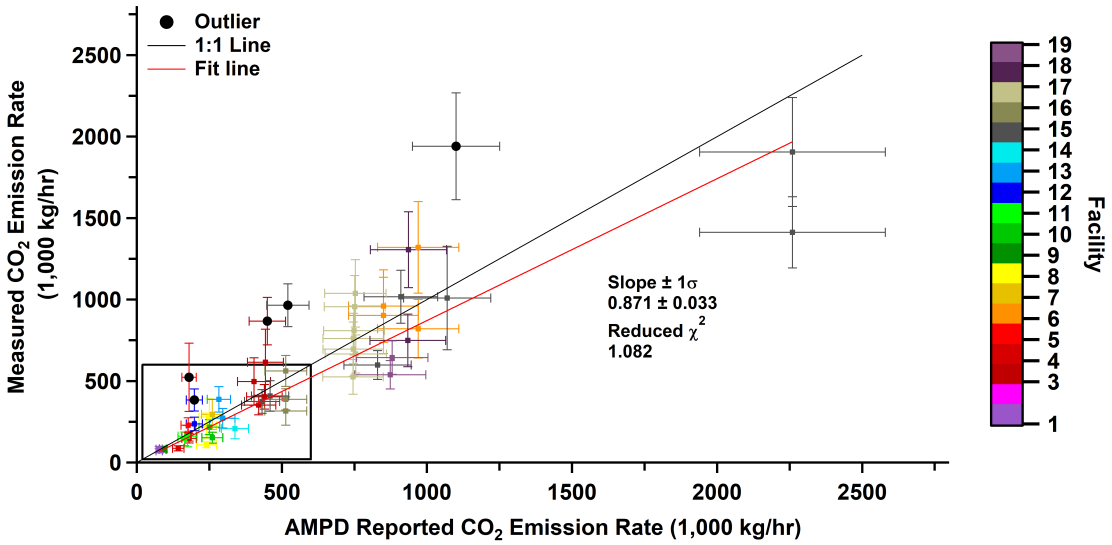

Figure 4.4. Figure 4.2 with the 5 outliers highlighted with black circles and the fit line recalculated without these outliers.

with low emissions [1]. The exact cause for this is a focus for future work. The 1 remaining flight is one of the few flights that did not fly above the emission plume, but otherwise does not seem to have any clear explanation for why it may be an outlier in performance. Other parameters, including the wind speed, the variability of the wind speed, the variability of the wind direction, and altitude of the lowest pass (Figure 4.7) were all briefly investigated for possible relationships that could explain the bias in the method, but no trends were observed.

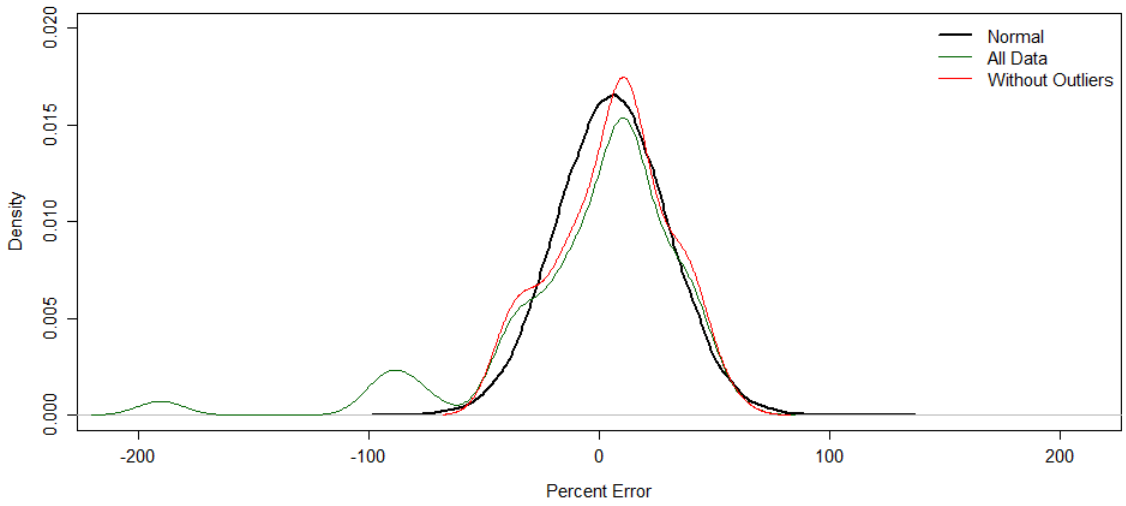

Figure 4.5. Probability Distribution Functions for the percent difference, and the percent difference without outliers. For reference, a normal distribution is also plotted. It is based on 100,000 random pulls from a normal distribution with the mean and standard deviation of the dataset without outliers.

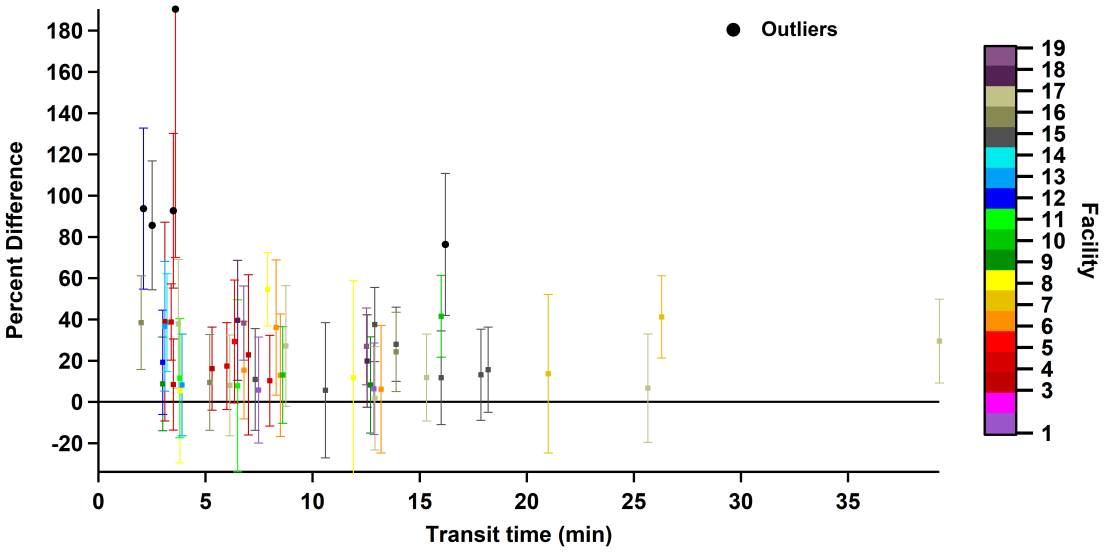

Figure 4.6. Absolute percent difference plotted against the transit time, calculated as the distance from the power plant to the location of the plume in the transect divided by the mean wind speed across the flight. This appears to have an exponential decay relationship, but it is driven primarily by a small number of outliers. Many facilities with similar transit times as the outliers do not have abnormally large percent differences.

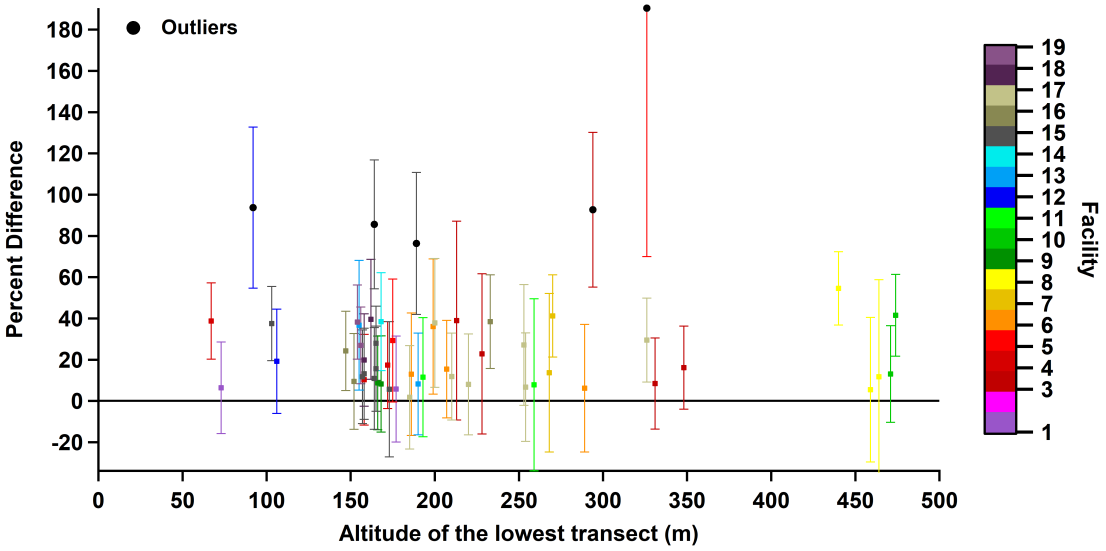

Figure 4.7. Absolute percent difference plotted against the altitude of the lowest transect, i.e. the gap between measurements and ground. There is no clear relationship between these variables, suggesting the impact of the emissions below the lowest altitude transect are not a dominant source of error.

4.3.2 Precision

These power plant MBEs can also be used to investigate the precision of the MBE technique by looking at back to back experiments. We note that these will yield an estimate of precision, except that they are not exact replicates, as there is a distance variable. Many of the flights included between 2 and 4 back to back MBEs at the power plant. With verification from CEMS that the ER remained approximately constant, these can be seen as replicate experiments. Although the increasing distance across replicate MBEs may have some impact, Figure 4.6 suggests this should generally be a small effect. The precision for each set of replicate MBEs is calculated as the standard deviation divided by the average MBE ER across the replicate MBEs and is shown in Figure 4.8. The average precision is calculated as 25% $\pm$ 16, comparable to the estimated 20% accuracy of the approach.

Although there is some uncertainty to these estimates, this work adds to the existing literature [50, 52] assessing the accuracy and precision of the airborne MBE. The calculated precision is in general agreement of both previous studies. Cambaliza et al. [50] calculated a precision of 30% with a range from 12 - 52% across 4 point source flights and the same general method. More recently, Heimburger et al. [52] calculated a precision of 22% based on 9 Indianapolis MBEs, each on a different flight day, assuming city emissions constant across the 1 month timeframe. Interestingly, the precision of the approach seems consistent between the regional/urban and point source scales, even though, in general, the S/N ratio is much larger for the point source emitters. This may result from compensating factors - for power plants, the S/N ratio is large, but the plumes are not well-mixed, leading to sampling statistics errors, while for urban regions, the S/N of the enhancement is relatively small, but the plume is relatively well-mixed, and sampling errors are minimized. If the average accuracy is assumed consistent as well, the MBE approach has a single experiment accuracy of 20%, which can be further reduced by averaging [52]. This has implications for the MBE approach as a means to detect policy-relevant changes in emissions over time.

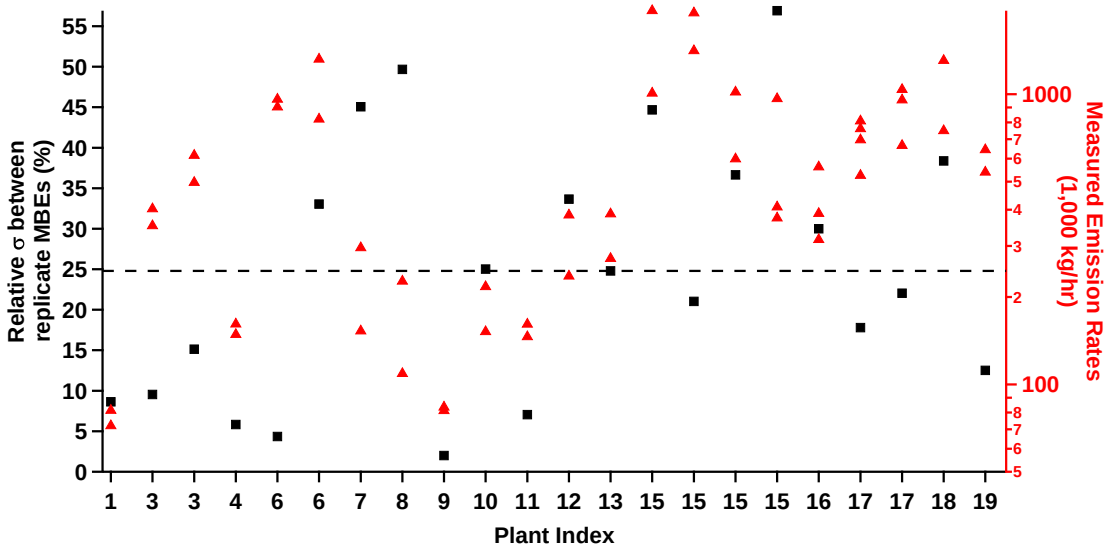

Figure 4.8. The relative standard deviation of replicate MBEs is shown in black, on the left Y axis. The reported ERs are shown on a log scale in red, on the right Y axis. The dashed line represents the average relative standard deviation, 25%. As can be seen in red, some plants were sampled 3-4 times in a single flight. Repeated x values represent separate flights at the same plant.

z

Using NY's 6%/yr reduction goal (85% reduction by 2050) as an example, single MBE campaigns could detect changes at a 95% confidence after 6.5 years (calculated as 20% * 1.96 / 6). However, flights are typically done in campaigns with multiple MBEs performed over a short timeframe. If the accuracy scales with $1/\sqrt{N}$ as would be expected, then the average of a 10 flight campaign would have a 1 σ accuracy of 6.3%, making it capable of detecting 6%/yr changes with 95% confidence after only 2 years.

5. ESTIMATING ANTHROPOGENIC CO_2 EMISSIONS FROM NEW YORK CITY USING AIRCRAFT MEASUREMENTS AND DISPERSION MODELLING

5.1 Motivation for Research

Carbon Dioxide (CO_2) emissions from fossil fuel combustion are the largest source of anthropogenic climate change [7]. The majority of these emissions occur in urban areas and the fraction of emissions from urban centers is expected to increase as populations continue to urbanize [103, 104]. As such, cities have been at the forefront of greenhouse gas (GHG) reduction efforts as evidenced by groups like the global covenant of mayors and C40 cities [108, 109]. Many U.S. cities have already set goals for significant GHG reductions and several states have passed legislation aimed at switching to renewable energy sources [105]. In particular, the state of New York (NY) has recently passed a suite of laws explicitly outlining actions to significantly reduce GHG emissions with set targets across sectors. The Climate Leadership and Community Protection Act sets a goal of net zero emissions from electricity, including purchased electricity, by 2040 and an 85% decrease across all sectors by 2050 [110]. On top of this legislation New York City (NYC) has passed the Climate Mobilization Act which includes a series of bills targeting building emissions, the largest emitting sector for the city when including indirect emissions [111], with large fines for non-compliance [112].

As cities work toward their reduction goals and enact laws with explicit reduction requirements that are monitored against self-reported bottom-up inventories, it becomes necessary to have high precision top-down emissions monitoring techniques to inform progress and details about the accuracy of these self-reported in-

ventories [31, 47, 50, 113, 114]. In addition to the self-reported inventories, there are published bottom-up inventories that utilize a combination of emission factors (e.g. kmol CO_2/m^2s for residential housing) and activity data (e.g. total area of residential homes, m^2), modeling, monitoring station data, fuel statistics, and other datasets from agencies like the Energy Information Agency (EIA) and Environmental Protection Agency (EPA) to allocate emissions in a gridded field [115–117]. There are also published disaggregated inventories that rely instead on proxies to disaggregate reported national total emissions to a gridded product. These can be generated more regularly at a global scale given they are less labor intensive, but have additional uncertainty due to the use of a proxy rather than the relevant activity data [118–120]. These high resolution inventories can inform policy about emissions, including relative emissions across sectors, and are often used in atmospheric transport modeling efforts [118, 121].

In this work we use the Stochastic Time-Inverted Lagrangian Transport (STILT) [122,123] dispersion model, with minor source code modifications, to combine airborne measurements downwind of the dense, heterogeneous domain of NYC with prior emissions during the non-growing season in a scaling factor (SF) approach. We convolve a "prior", or modified inventory used as an initial estimate of emissions for the period of our flights (described in detail in Section 5.2), with footprints calculated using the STILT dispersion model to calculate modeled enhancements. We then calculate posterior results by combining SFs, which represent a ratio between the measured and modeled enhancements, with the prior data [47, 124–126]. Finally, we investigate multiple methods of calculating the SF and discuss the variability in the resulting posterior emission rates across SF calculation method, flight day, background definition, choice of meteorology product (MET) used to drive STILT, and choice of prior. This approach allows us to calculate a campaign averaged emission rate that, with additional flights in coming years, could also be used to monitor changes in emissions over time, such as the impact of the COVID-19 "shutdowns" on CO_2 emissions.

Previous studies have also derived top-down estimates of urban emissions using the mass balance method [45, 46, 50, 53, 127] and more complex inversion techniques [31,107,128,129]. Mass balance experiments provide a domain-total emission rate that can be calculated relatively quickly based on a simple conceptual model. However, for cities that are surrounded by other emission sources it is difficult to define both an appropriate background concentration and the area over which the prior emissions should be aggregated when comparing to the measured flux.

Inverse modelling techniques use a dispersion model to simulate concentration enhancements at the measurement locations based on prescribed emissions. This emission map is then optimized to reduce mismatch between the simulation and the measurements [31, 107, 126]. These approaches require information on the error covariances of the transport model, prior, and measurements to constrain the solution. They then typically involve weighting these data based on the prescribed error covariances to reach an optimized posterior that combines the information from the prior and the measurements [31, 130–132].

The SF approaches employed in this study follow the same basic premise as an inverse model approach, but constrain the solution to have the same spatial distribution as a prescribed prior [47]. Conceptually, this can be thought of as an inverse modeling solution where the state vector has been condensed to a limited set of scaling factors. This induces aggregation errors and limits the spatial patterns that can be inferred, however, it allows for a simpler approach to calculate posterior emissions and their sensitivity to model parameters without having to deal with the complexities of the error covariances for both the transport and the prior emissions [133, 134]. While most of the SF approaches are unable to directly account for uncertainties in the modeled data, we derive information about the transport error in this work through the use of multiple MET. Similar SF approaches have recently been demonstrated using towers in Boston [124, 125] and aircraft in an oil and natural gas field [126]. In cases where the spatial distribution of prior emissions is sufficiently accurate to

reproduce the measured plume structure, the different assumptions inherent in this method makes it a good complement to more complex inverse approaches.

5.2 Methods & Materials

5.2.1 Flight Design and Equipment

All flights were conducted using Purdue University's Airborne Laboratory for Atmospheric Research (ALAR), a modified twin-engine Beechcraft Duchess [46, 50]. ALAR is equipped with a GPS/INS system, a Best Air Turbulence probe for high precision 3-dimensional winds [32, 33], and a Picarro Cavity Ring Down Spectrometer designed for measurements of CO_2, methane (CH_4), and water vapor (H_2O) [35], although this work focuses exclusively on CO_2 emissions. Measurements are reported as dry air mole fractions, in units of micromoles per mole of dry air, or parts per million (ppm). Each flight included multiple in-situ three-point calibrations using NOAA-certified standard cylinders of CO_2 and CH_4 (WMO-CO2-X2007, WMO-CH4-X2004A).

As biosphere emissions/uptake could complicate this analysis, we used a TROPOspheric Monitoring Instrument (TROPOMI)-derived Gross Primary Production (GPP) product described in Turner et al. [135] to confirm that the biosphere was less active. Briefly, during photosynthesis chlorophyll α molecules are excited by absorbed sunlight, then de-excitation occurs either through dissipation of heat or re-emission via fluorescence. The small fraction of light that is re-emitted at longer wavelengths ($\leq$2% in a two-peak spectrum from $\sim$650–850 nm) is called solar-induced chlorophyll fluorescence (SIF) and has been measured using a variety of satellite platforms already [135, 136]. Some work suggests that SIF is a better proxy for photosynthetic activity than other vegetation indices as it is directly related to the radiation absorption, whereas indices like the normalized difference vegetation index are more akin to the photosynthetic capacity. Turner et al. [135] have recently used TROPOMI satellite data to derive high resolution SIF estimates and, using comparisons to tower

measurements, directly related this to GPP based on a strong linear relationship that was consistent across ecosystems. The TROPOMI spectrometer measures in the UV/vis, and near IR, including the far-red part of SIF emissions at 725-775 nm, using four different detectors while aboard the Sentinel-5 Precursor satellite (launched in 2017), as shown in Figure 5.1. It covers ∼2600 km with a given swath with 7 km resolution along the track and 3.5 - 15 km resolution across it (worsening resolution as it approaches the edge of the swath) as illustrated in Figure 5.2 [137].

The flight campaign involved a total of 7 flights around NYC in March 2019 and 2020, and November of 2018 and 2019. Airborne measurements allow us to capture vertical variability in CO_2 concentrations and give us a large footprint, such that our measured CO_2 enhancements are sensitive to emissions distributed over a wide area. All flights were conducted by flying transects perpendicular to the mean wind direction at a set distance downwind of NYC, with multiple passes through the NYC plume at multiple altitudes within the boundary layer. An upwind pass was also flown just before/after the downwind passes to verify the absence of inflowing plumes of elevated GHG concentrations. Flight tracks for the downwind passes for all 7 flights are shown in Figure 5.3A.

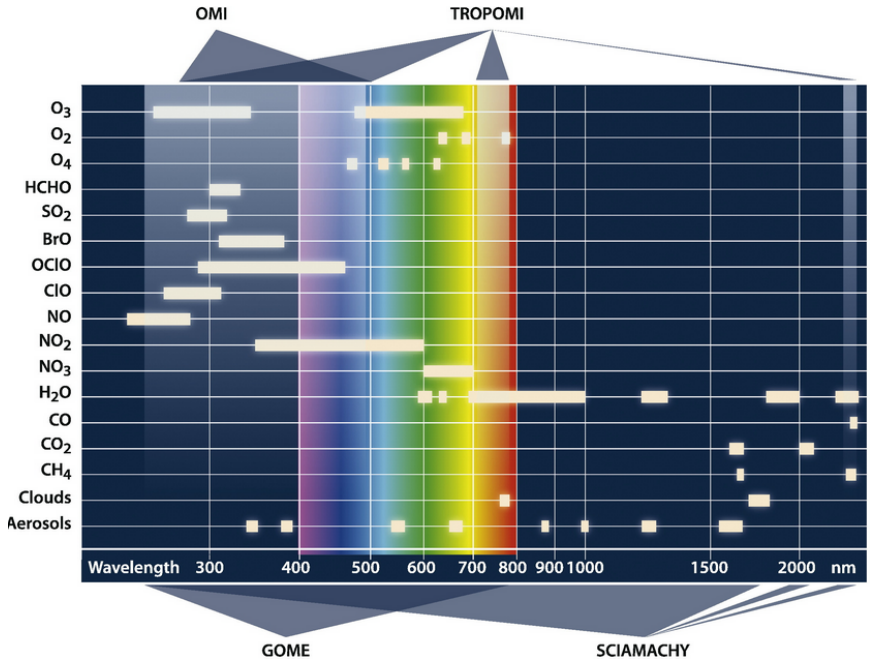

Figure 5.1. Spectral range of TROPOMI and several previous satellites with similar goals along with the absorption features of relevant pollutants and GHGs. Figure 2 from Veefkind et al. [137]

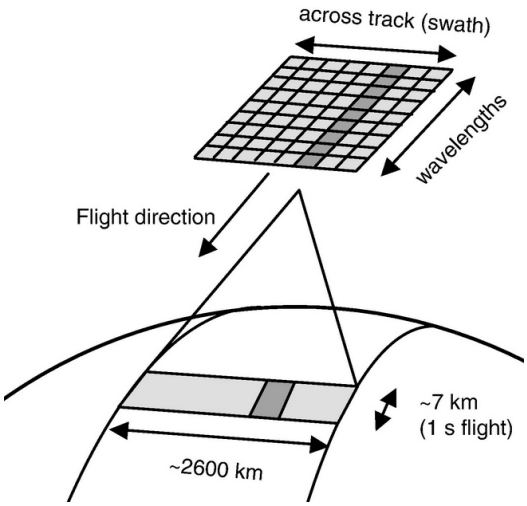

Figure 5.2. Example depiction of the track and resolution of TROPOMI. The entire 2,600 km swath is measured simultaneously and the dark grey surface area is measured as a spectrum in the detector, as shown with the dark grey pixels. Figure 1 from Veefkind et al. [137]

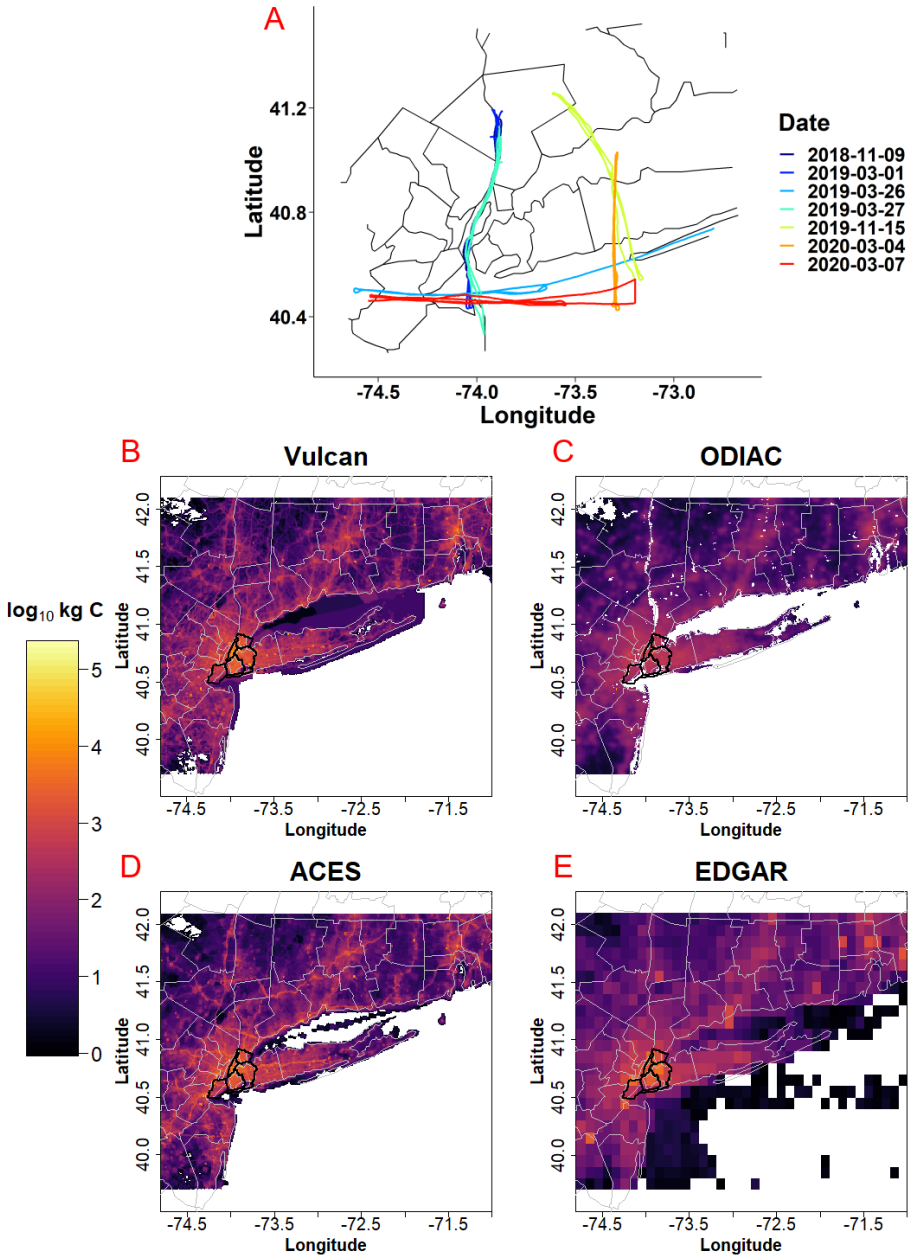

Figure 5.3. (A) All flight tracks overlaid on a county map. 2018-11-09, 2019-03-01, and 2019-03-27 had similar downwind passes over the Hudson River and thus cannot be distinguished in Figure 5.3A. Winds were from the east on 2018-11-09, 2019-03-01, and 2019-03-27, west on 2019-11-15 and 2020-03-04, and north on 2019-03-26 and 2020-03-07. (B-E) Each CO_2 prior overlaid on a county map, with the 5 NYC boroughs [138] highlighted in black. All priors are in $\log_{10}$(kg C/km^{2}hr) for 12:00 pm on 2019-03-27 truncated at 1 kg C/km^{2}hr .

One of the flights, 2018-11-09, showed poorly modeled boundary layer heights (as compared to in-flight observations) across the higher resolution MET (HRRR, NAMS, NAM12) as shown in Figure 5.4 and thus these MET were excluded from this flight in all analyses. On two flights, 2019-03-01 and 2020-03-04, ERA5 had similar difficulty representing the boundary layer heights as shown in Figure 5.5 and was also excluded [139]. Not only are the higher altitude passes during these flights showing modeled enhancements that are too small, but the lower altitude passes also show modeled enhancement that are too large, consistent with what would be expected when the emissions are mixed into a CBL that is smaller than that measured. These modeled boundary layer heights are calculated using a modified Richardson number (the ratio between buoyant and shear forces) calculated from the MET, as is the default approach to estimating the boundary layer height in STILT. Finally, the flight on 2019-03-27 showed evidence of free tropospheric influence on the southern half of the two highest passes as shown in Figure 5.6, suggesting a low marine boundary layer. As such, we have excluded these top two transects from all analyses.

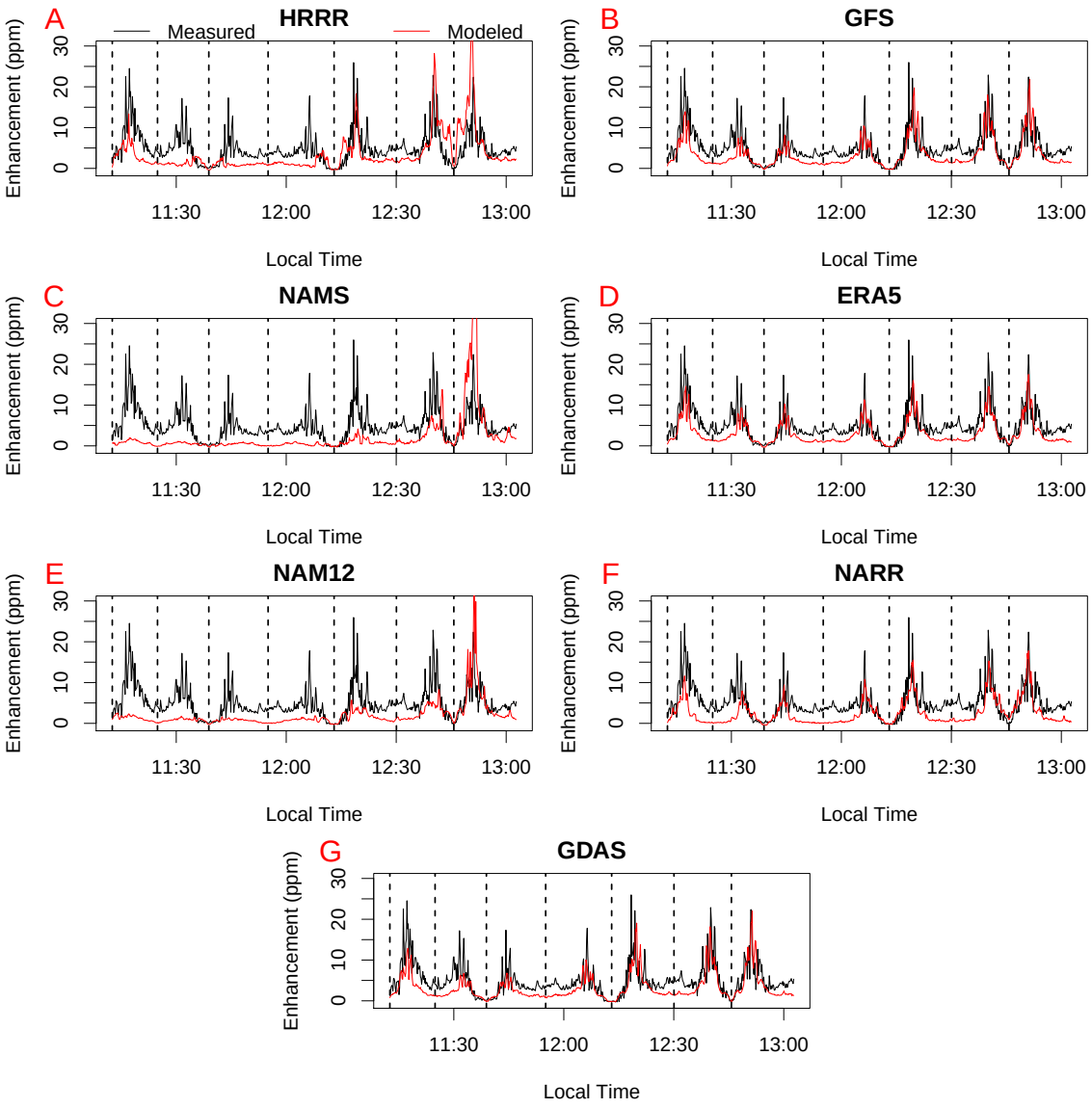

Figure 5.4. Measured and modeled enhancements across (A, C, E) the higher resolution MET and (B, D, F, G) the lower resolution MET. These enhancements are based on the percentile background and Vulcan prior for 2018-11-09. Dashed vertical lines represent the individual passes downwind of NYC. Chronologically, the median altitudes for each pass were about 450m, 590m, 590m, 520m, 350m, 300m, and 230m.

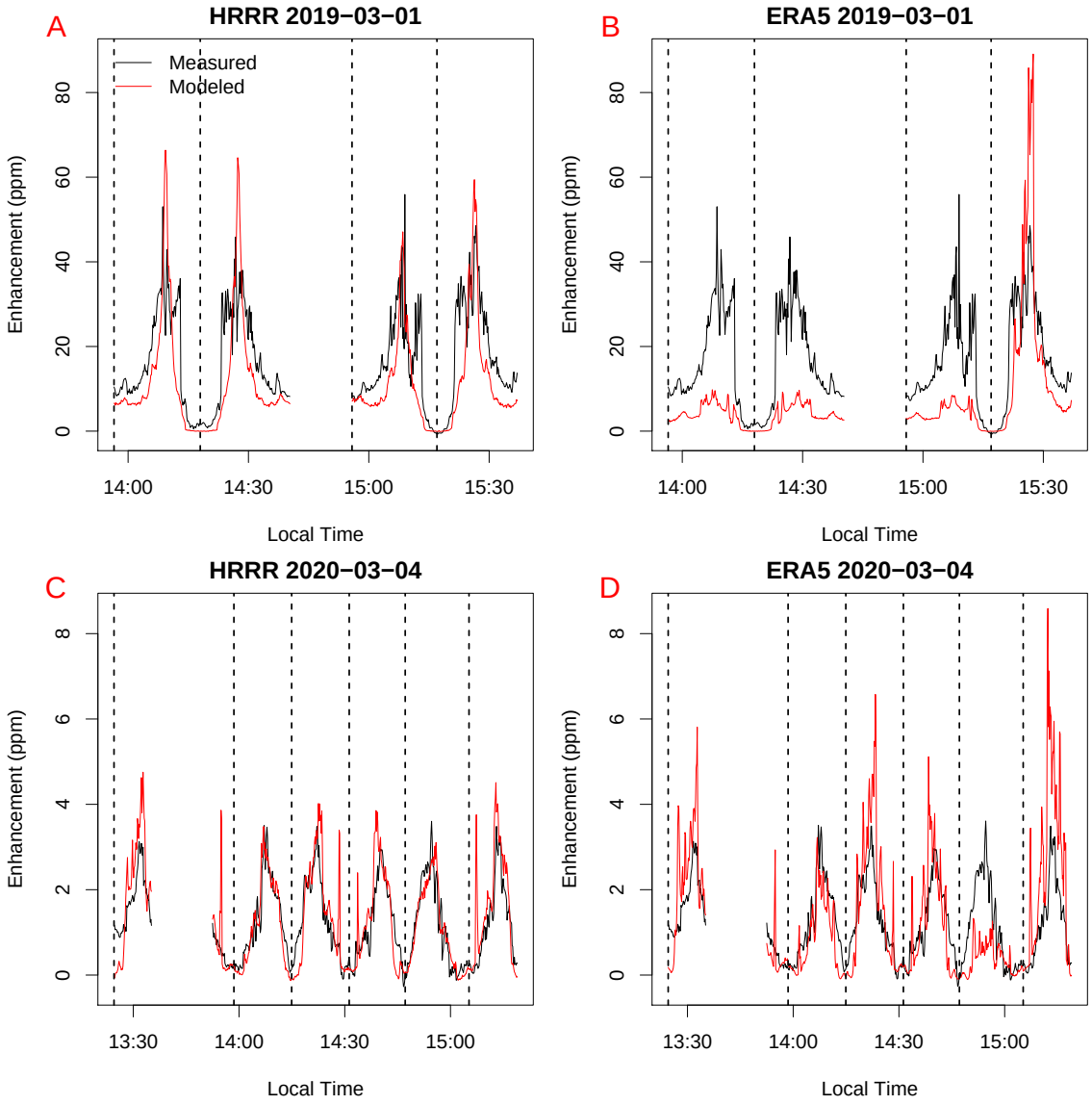

Figure 5.5. Measured and modeled enhancements for (A, B) 2019-03-01 and (C, D) 2020-03-04. These enhancements are based on the percentile background and Vulcan prior. Dashed vertical lines represent the individual passes downwind of NYC. Chronologically, the median altitudes for each pass on 2019-03-01 were about 280m, 330m, 400m, and 190m and on 2020-03-04 they were about 350m, 1010m, 590m, 810m, 1190m, and 360m. Gaps are vertical profiles that have been removed from all analysis.

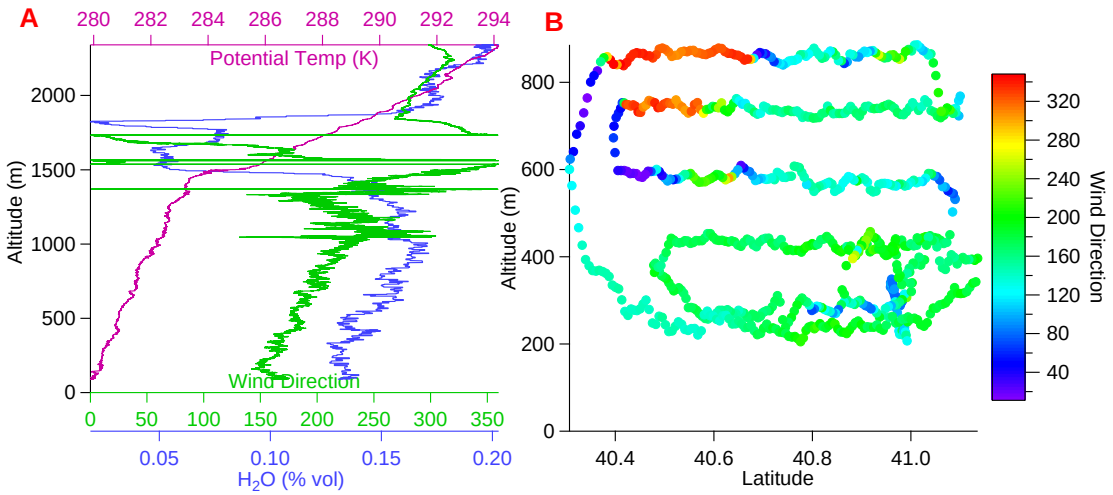

Figure 5.6. (A) shows a vertical profile with potential temperature, H_2O, and wind direction performed on 2019-03-27 at the northern end of the transect, near Croton Bay. There is a clear change in the airmass at 1500 m with considerable change in the winds. (B) shows the downwind curtain colored by wind direction in degrees with 0 and 360 equal to winds coming from due N and 90 representing winds from due E. It is clear that during the top two transects the aircraft was not sampling within the marine CBL on the southern end even if the altitude was lower than 1500 m, as such we have excluded these transects from our analysis.

5.2.2 Transport Modeling

The basic principle of a Lagrangian particle model such as STILT is to track a theoretical cloud of particles over time using a modeled MET field. This first involves defining a set of locations, or receptors, from which to release the particles. Particles are moved, in our case backwards in time, based on the average MET wind field with a random 3D velocity added to simulate turbulence. We can quantify the surface influence impacting the air mass measured at the receptor by tracking these particles in 3 dimensions as they flow out of the domain [123].

The model domain is shown in Figure 5.7 and is defined as -74.8 to -71 degrees longitude and 39.7 to 42.1 degrees latitude. Receptors were defined as 10 s block averages of flight data, excluding vertical profiles. Using STILT we released 500 particles per receptor and followed them back in time with run times long enough to ensure >95% of the particles exit the domain with the exception of the flight on 2018-11-09, which had changing wind directions throughout the previous evening and early morning that caused up to 20% of the particles to remain in the domain for some receptors. To characterize the transport modeling uncertainty we drive the STILT model with 7 MET models: the Copernicus ERA5 global reanalysis [140] and 6 from the National Oceanic and Atmospheric Administration's gridded data archives [141], namely the North American Mesoscale Forecast System with Hybrid Sigma Pressure levels (NAMS), a temporally coarser variant of NAMS archived on isobaric vertical levels (NAM12), the High-Resolution Rapid Refresh (HRRR), the Global Forecast System (GFS), the Global Data Assimilation System (GDAS), and the North American Regional Reanalysis (NARR) (see Table 5.1). Note that NARR and GDAS (0.5 deg) were not archived by NOAA after 12/2019 and 6/2019 respectively so we do not use these MET for flights performed after these dates. As particles are not restricted to a grid and the MET is interpolated to subgrid-scales, all of these MET can be used to generate influence functions on a consistent, fine grid. We used a 1.2 x 1.2 km resolution grid when generating the influence functions, or footprints, that

quantify the observations' sensitivity to surface emissions. The main model time-step was set to 1 minute, and the hyper near field correction was used in all cases [122].

The source code edits to STILT in this work were both minor. First, the starting time of trajectories was not set appropriately. The minutes of the starting time were being ignored, causing the trajectories to begin at the start of the intended hour, e.g. 12:55 pm would instead be treated as 12:00 pm. This should have little impact if meteorological conditions are fairly consistent hour to hour, but can cause sharp changes in trajectories over time if not and thus was corrected. Second, the MET data for the hour before and after the trajectory were not utilized in the original STILT code. This is relevant as the MET is interpolated to higher temporal resolutions when running trajectories and the hour before/after the run would both be needed to do so properly.

Table 5.1.
MET Spatiotemporal Resolutions [140, 141]

	HRRR	**NAMS**	**NAM12**	**GFS**	**ERA5**	**NARR**	**GDAS**
Resolution	3 km	12 km	12 km	0.25°	0.25°	32 km	0.5°
Frequency	1 h	1 h	3 h	3 h	1 h	3 h	3 h
Vertical Layers	36	40	26	55	37	24	55

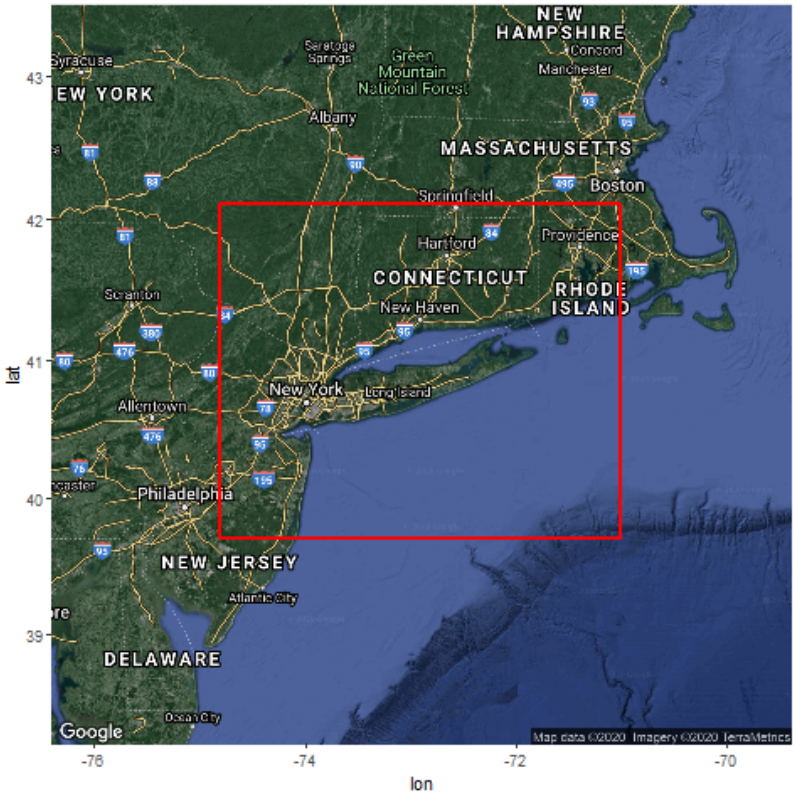

Figure 5.7. Map of the domain highlighted in red, overlaid on top of a google earth image.

5.2.3 Prior Emissions

We use two bottom-up national inventories, the Anthropogenic Carbon Emissions System (ACES) version 2.0 [142] and Vulcan version 3.0 [143] as well as two global disaggregated inventories, the Open-source Data Inventory for Anthropogenic CO_2 (ODIAC) version 2019 [144], and the Emission Database for Global Atmospheric Research (EDGAR) version 5 [145, 146] as our priors. At the time of analysis, none of the inventories we used covered the timeframe of our flights. We use the most recent data for all priors, which is 2018 for EDGAR [145] and ODIAC [144], 2017 for ACES [142], and 2015 for Vulcan [143]. All priors are $\sim$1 km^2 resolution except for EDGAR, which is 0.1 deg x 0.1 deg (approx. 12 km^2 at NYC). Currently, ACES and

Vulcan are both available at an hourly resolution, ODIAC is monthly and EDGAR is annual. To take full advantage of the hourly resolution of ACES and Vulcan, we calculate the footprints hourly and multiply them with the corresponding hour of the prior.

EDGAR and ODIAC are used unaltered, but for the hourly priors we better account for the fact that the prior emissions are for a different year by using 5-week averages of emissions from the same day of the week as the actual flight day. For example, 3/27/2019 is a Wednesday so we average each hour of the nearest Wednesday in 2017, 3/29/2017, and the 2 previous and following Wednesdays (3/15, 3/22, 3/29, 4/5, 4/12) to represent 3/27/2019. This is particularly important with regard to the difference between weekday and weekend emissions [147]. Using the nearest day alone (3/29/2017) would assume that the emissions magnitude, diurnal pattern, and spatial structure are exactly the same on the flight day (3/27/2019) as they were on the nearest day of the prior year (3/29/2017). The 5-week average does still assume that the monthly averaged prior is a reasonable representation of the spatial distribution of emissions on the flight day, ignoring potential changes between the year of the prior emissions and that of the flights.

There are some reprojection errors in the multiplication of prior with footprint as ACES and Vulcan are provided in a Lambert Conformal Conic (LCC) projection while EDGAR, ODIAC, and the STILT footprints are provided in a Latitude/Longitude (Lat/long) projection. Any conversion to a different projection will introduce some spatial smoothing errors. To convolve the footprints with the priors they must be in the same projection, so for our analysis we reprojected the LCC priors to a Lat/long projection. As an estimate of this error we calculated the percent difference in the domain-sum across these two projections for Vulcan at $\sim$7%, with the LCC projection having the larger domain-sum. The difference between modeled emissions when reprojecting the footprint to LCC to convolve and when reprojecting the prior to Lat/long to convolve is shown in Figure 5.8. The case where footprints are reprojected to the LCC projection leads to campaign averaged posterior results that are

~7% larger than for the case of reprojecting the priors to the lat/long projection (the approach used in all analyses).

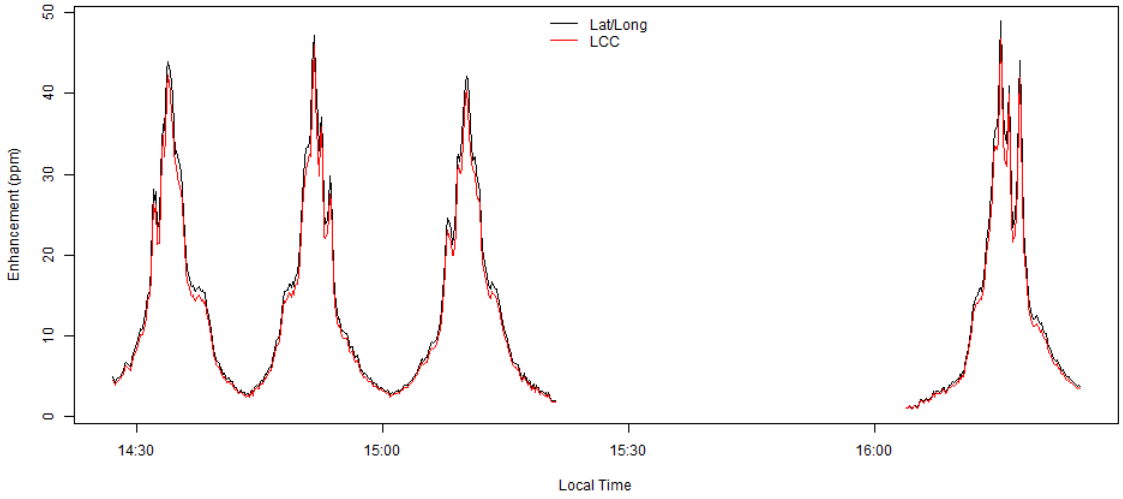

Figure 5.8. Modeled enhancements using the Vulcan prior and GFS MET on 2019-03-27 calculated by reprojecting the prior to the Lat/long grid (black) and by reprojecting the MET to the LCC grid (red) before convolving.

5.2.4 Scaling Factor Approaches

Modeled anthropogenic CO_2 enhancements along the flight track were simulated by multiplying footprints (ppm$\cdot(\frac{\mathrm{m^2 s}}{\mu\mathrm{mol}})$ or mole fraction/flux) from the STILT dispersion model [122, 123] by emissions from one of a selection of priors (converted to $\frac{\mu\mathrm{mol}}{\mathrm{m^2 s}}$). This multiplication was done on an hour-by-hour basis to take full advantage of the temporal resolution of some of the priors. The model simulates the enhancement in CO_2 relative to a "background" value at the boundary of the domain, and this background must then be subtracted from observed concentrations in order to compare the observed enhancements with the model.

Background Calculations

We calculated the background concentrations using two methods: a percentile method [107] and a linear method [46, 106] (LR). For the percentile background we first added the modeled and measured data point-wise so our choice of background is based on both datasets. Next, we identified the timestamps with concentrations below the 5^{th} percentile of concentrations from this combined dataset. We calculated the measured background as the average of all measured data during these timestamps. As the modeled concentrations for these points were small but non-zero, we also calculated a modeled background as the average of all modeled data during these same timestamps as shown in Figure 5.9A, C, and E. As the computed background is dependent on the modeled data, this process was repeated for every flight to yield a slightly different background for every unique combination of MET and prior. If we had defined the background points based solely on the measured dataset, this could have led to the selection of background points with large modelled concentrations in cases where the modeled plume was mis-located. Using the combined measurement-model dataset as described above mitigates this issue.

The LR background calculation method used a 10-point linear regression through the edges of each transect. It was calculated for every transect with a different fit for every unique combination of MET and prior. The 5 lowest concentrations during the first/last 20% of the transect were used to calculate the 10-point regression as shown in Figure 5.9B, D, and F. Figure 5.10 shows the enhancements above the linear background for an example flight. There was 1 transect on 2019-03-26 that did not extend completely into background on one side so the average background data from the other two transects was used. Because the three transects occurred back to back and the remaining two transects were consistent (5-point average and 1σ of 416.84 ppm $\pm$ 0.07 ppm and 416.87 ppm $\pm$ 0.12 ppm for the 2 transects), it is unlikely this approach adds significant uncertainty. Additionally, on 2019-11-15 HRRR modeled

plumes did not return to background so the average fit from the other MET was used to define the background as shown in Figure 5.11.

To relate the measured and modeled enhancements we calculated SFs, which represent the factor by which the modeled enhancements need to be multiplied to best match the measurements, using 5 methods described below and summarized in Table 5.2.

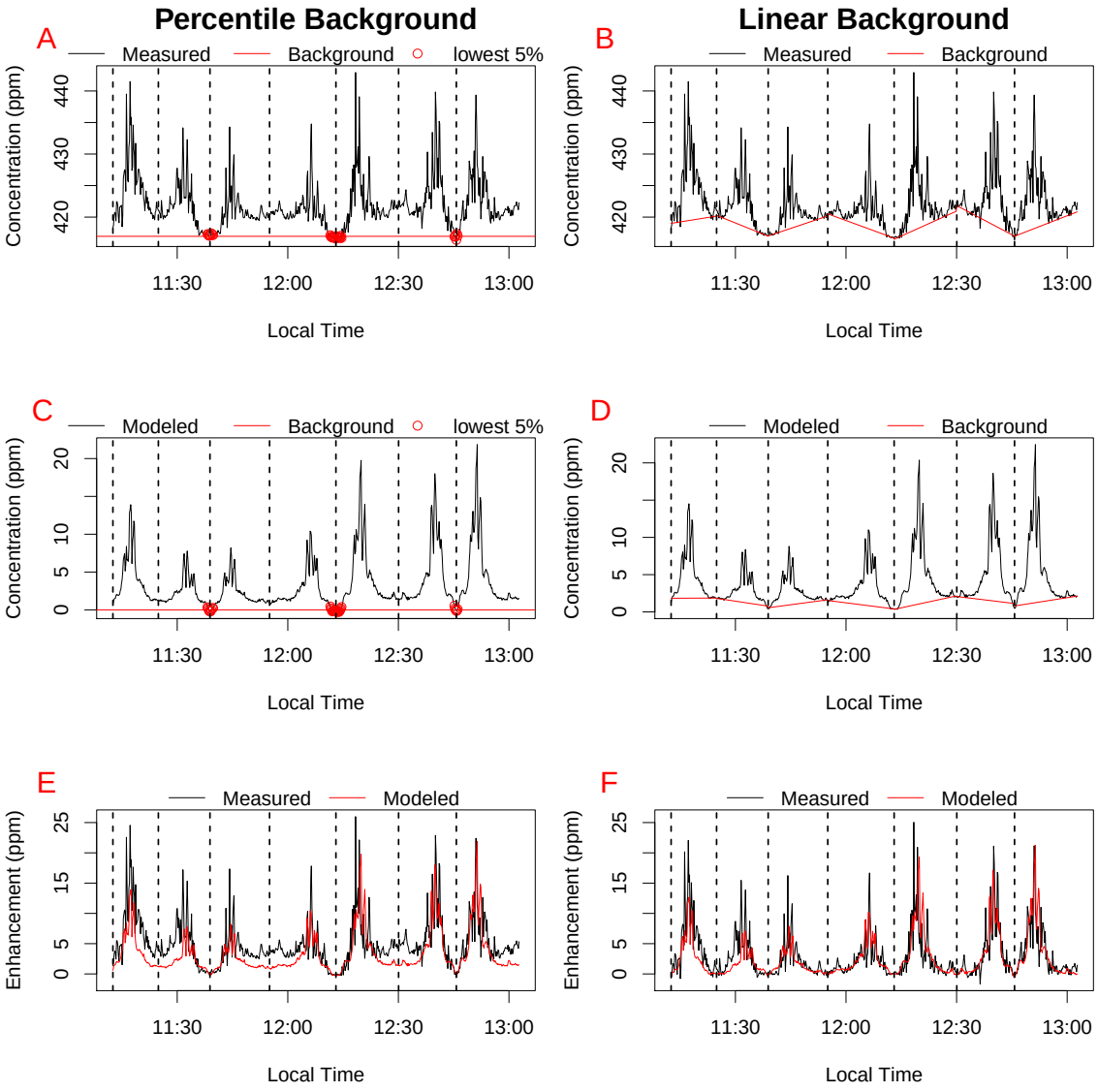

Figure 5.9. (A) Measured and (C) modeled data from the flight on 2018-11-09 with the points used to define the percentile background marked with red circles and the average of them a red line. (E) Measured and modeled enhancements using the percentile background. (B) Measured and (D) modeled data from the same flight with linear backgrounds marked with red lines. (F) Measured and modeled enhancements using the linear background. Dashed vertical lines in all plots represent transect bounds (aircraft 180°turns) and all modeled data is based on GFS and the Vulcan prior. Chronologically, the median altitudes for each pass were about 450m, 590m, 590m, 520m, 350m, 300m, and 230m.

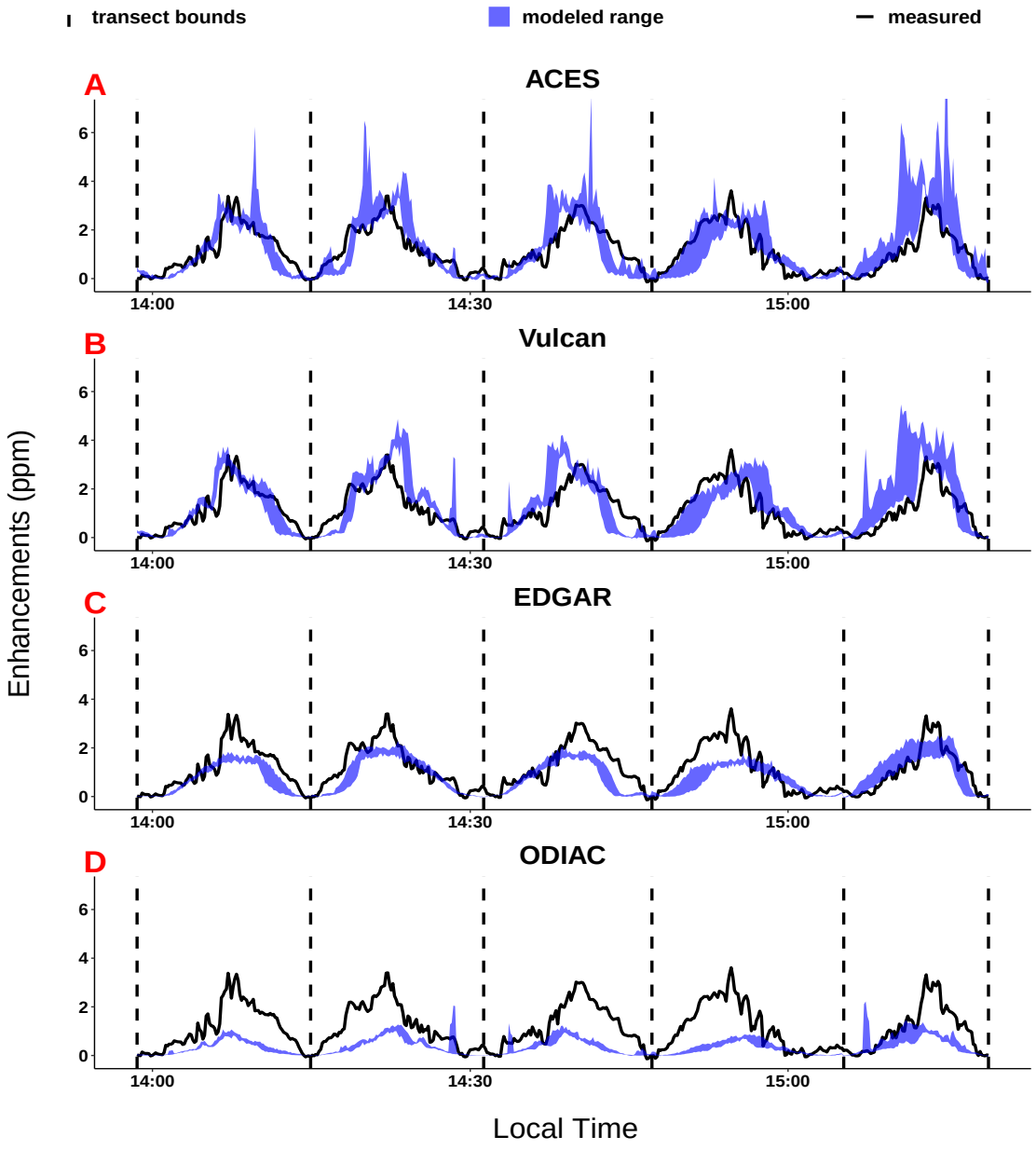

Figure 5.10. Measured and modeled CO_2 enhancements over time using the linear background for the flight on 2020-03-04. Model bands represent the range of enhancements across all MET excluding NARR and GDAS (unavailable for this timeframe). Chronologically, the median altitudes for transects were about 1010 m, 590 m, 810 m, 1190 m, and 360 m above ground.

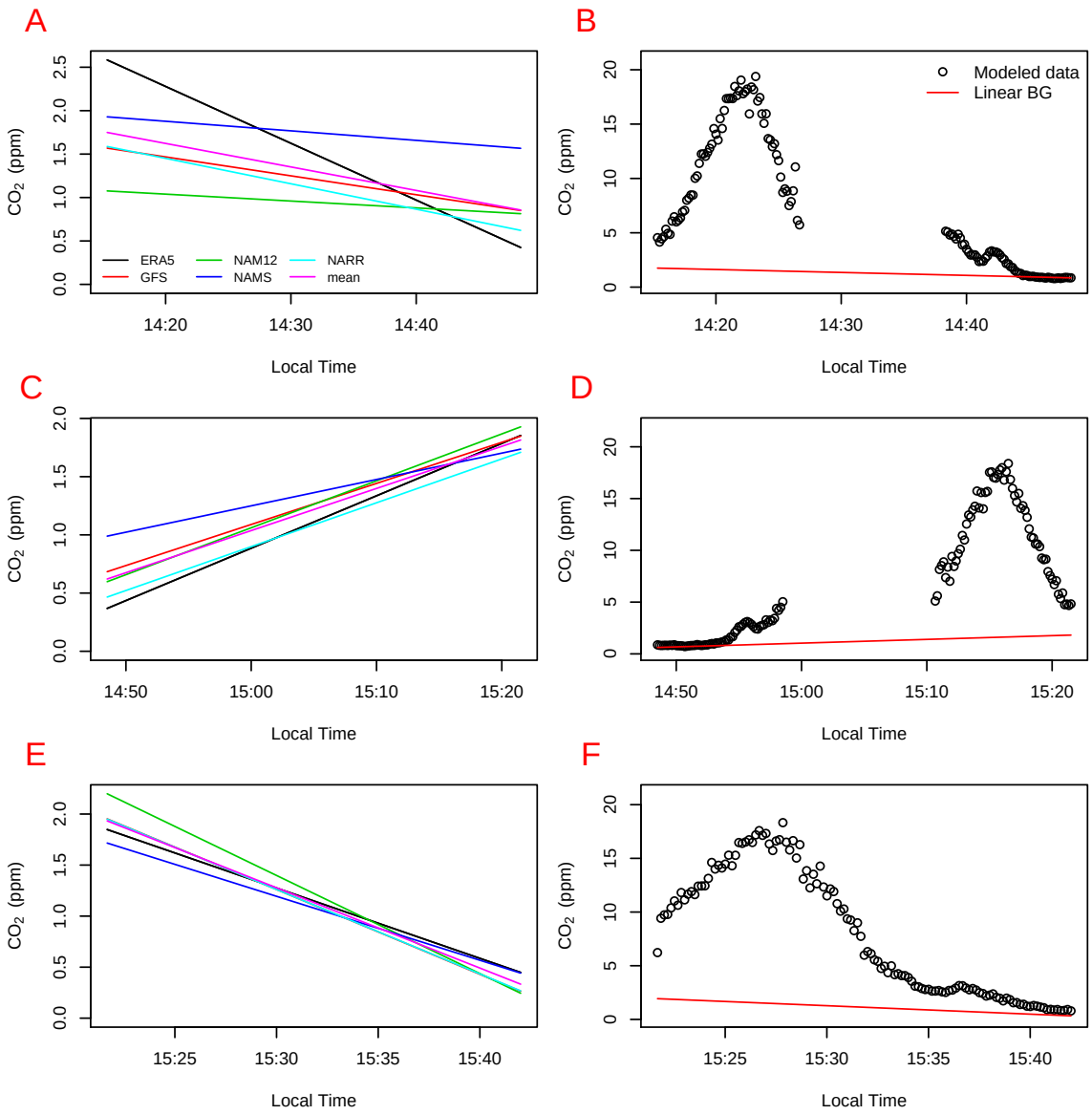

Figure 5.11. (A, C, E) The fits used as the linear background for all the various MET for the 3 passes on 2019-11-15 as well as the average across them, used as the background for HRRR modeled data. (B, D, F) The modeled data and the linear fit being used as the background for HRRR for the 3 passes on 2019-11-15. All data shown here is using the Vulcan prior. Gaps in the first two passes are vertical profiles that have been excluded from analysis.

Integral (I) SF Method

The first scaling factor method used was an integral ratio SF (I). We integrated enhancements over each downwind transect through the plume for both measured and modeled enhancements. The ratio of these integrated enhancements gives a SF for that transect (Eq. 5.1).

$$SF(I) = \frac{\sum (CO_{2obs} - BG_{obs})}{\sum (CO_{2mod} - BG_{mod})} \tag{5.1}$$

Here CO_{2obs} and CO_{2mod} represent the measured and modeled mole fractions respectively, while BG_{obs} and BG_{mod} represent the measured and modeled background mole fractions.

Regression (fit, fit-0) SF Methods

The second approach that we used to calculate SFs was a simple ordinary least squares (OLS) fit of modeled enhancements against measured enhancements across a transect (fit). The slope of this fit is the reciprocal of the SF for this approach. This was repeated with the intercept forced to zero (fit-0), as this can mitigate the impact of poor correlation on the slope.

Bayes (B, 2B) SF Methods

We calculated a SF using two different approaches that rely on Bayes' Theorem. In general, the Bayesian approach can be written as

$$y = H(\lambda) + e_r \tag{5.2}$$

Here $\mathbf{y}$ is the observations vector (n x 1, where n is the number of observations), here the analyte (CO_2) mole fraction enhancements measured along the track; λ is the state vector (m x 1, where m is the total number of unknowns) or vector of parameters which we aim to optimize; $\mathbf{H(\lambda)}$ is the observation operator (n x 1) which

converts the model state to observations (i.e. the STILT dispersion model) and $\mathbf{e}_r$ is the uncertainty in the measurements and in the modeling framework (model-data mismatch).

Optimum posterior estimates of fluxes are obtained by minimizing the cost function J [148, 149]:

$$J(\lambda) = \frac{1}{2}\left[(\lambda - \lambda_b)^T P_b^{-1}(\lambda - \lambda_b) + (H(\lambda) - y)^T R^{-1}(H(\lambda) - y)\right] \tag{5.3}$$

Here λ_b is the first guess or a priori state vector, $\mathbf{P}_b$ the a priori error covariance matrix which represents the uncertainties in our a priori knowledge about the state vector, and $\mathbf{R}$ the model-data error covariance matrix, which represents the uncertainties in the observation operator $\mathbf{H}$ and the observations $\mathbf{y}$, also known as model-data mismatch.

The observations operator, $\mathbf{H(\lambda)}$ is a function of the unknown parameters and represents the model used to simulate the observations. This includes the transport, $\mathbf{T(x)}$, of trace gases from the sources, $\mathbf{x}$ (s x 1, with s the number of sources), to the measurements plus additional terms if desired. Assuming $\mathbf{H}$ is a linear function of λ, we can write in matrix form:

$$H(\lambda) = H_{nxm}\lambda_{mx1} \tag{5.4}$$

First, we consider a model where only a single scaling factor λ (m = 1) is used to scale the emissions (method B):

$$H_{nx1} = T_{nxs}x_{sx1} \tag{5.5}$$

In this case, the prior covariance is a 1x1 matrix populated with the a priori variance of the scaling factor (λ_1):

$$P_b = \left[\sigma_{\lambda 1}^2\right] \tag{5.6}$$

Then, we can also consider a model where three parameters λ (m = 3) are used (method 2B). In this case, the first parameter represents the SF, the second parameter represents a constant offset to account for potential background bias and the

third parameter represents the slope of a linear trend to account for gradients in the background. Thus, we can write $\mathbf{H}_{nx3}$ as follows:

$$H_{nx3} = \begin{bmatrix} & & 1 \\ T_{nx1} & I_{nx1} & \vdots \\ & & n \end{bmatrix} \tag{5.7}$$

and the prior covariance as a diagonal 3x3 matrix populated with the a priori variances of the parameters assuming the parameters are uncorrelated:

$$P_b = \begin{bmatrix} \sigma^2_{\lambda 1} & 0 & 0 \\ 0 & \sigma^2_{\lambda 2} & 0 \\ 0 & 0 & \sigma^2_{\lambda 3} \end{bmatrix} \tag{5.8}$$

In both cases, and assuming the model-data errors are uncorrelated, the **R** error covariance can be written as a diagonal n x n matrix populated with the uncertainties in the transport model and the measurements added in quadrature.

An analytical solution exists to the minimization of Equation 5.3 and can be written as [150]:

$$\lambda_a = \lambda_b - K\left(H\lambda_b - y\right) \tag{5.9}$$

$$K = P_b H^T \left(H P_b H^T + R\right)^{-1} \tag{5.10}$$

where λ_a is the optimized state vector, which contains the optimized parameters in our model and **K** the Kalman gain.

In this work, we chose as prior parameters λ_b= [1 0 0]^T with prior uncertainties of [1 1 0.1]^T, i.e. assuming a SF = 1 and no correction to the background necessary. The transport model uncertainty is computed as the 1σ of the modeled enhancements across the various MET and the measurements uncertainties is computed as the average 1σ during the calibrations of the specific flight, an estimate of instrument precision.

Posterior emission totals for NYC were calculated by multiplying these SFs by the total prior emissions within the 5 borough boundaries (including water areas) [138]

Table 5.2.
SF and Background Methods

Method	Variables fit	Description
Linear Background (LR)		Linear regression through 5 points on each side of the plume. Applied separately for each transect and for each combination of MET and prior.
Percentile Background		Average of the lowest 5% of data. The same points are used for both measured and modeled data. Applied separately for each flight and for each combination of MET and prior.
Integral (I)		Integrated measured enhancements divided by integrated modeled enhancements.
Regression (fit)	2	Reciprocal of the slope of an OLS regression between modeled enhancements plotted against measured enhancements.
Regression forced through 0 (fit-0)	1	Fit, but calculated when forcing the regression through the origin.
Bayesian (B)	1	Bayesian calculation using measured enhancements, modeled enhancements, and uncertainty estimates.
Bayesian with a background correction (2B)	3	B with 2 additional terms to adjust the background with a linear correction.

shown in Figure 5.3B-5.3E. This SF approach assumes that the SF obtained for the modeled enhancements calculated using the footprints within the domain also applies to the NYC Boroughs, which represent 24% of the total emissions in the domain (based on annually averaged Vulcan) while representing only ∼1% of the area. Given ACES and Vulcan are hourly products, we had to address which hours to use in this calculation. To do so, we combined all footprints for each transect separately and calculated the fraction of modeled emissions that came from NYC when using Vulcan and HRRR. All hours where at least 40% of the modeled emissions originated from NYC were averaged to represent the relevant prior emissions. This typically resulted in averaging the prior over the first few hours of the footprint. Although the prior, MET, and threshold used to select these hours are subjective, they only impact the exact midday hours being averaged and have little impact on the posterior or its variability.

5.3 Results & Discussion

We used a TROPOMI SIF-derived Gross Primary Productivity (GPP) product [135] to confirm that the biospheric uptake of CO_2 was small and did not complicate the urban mixing ratios measured in this study. Our analysis shows that during our flights the GPP of NYC was $\leq 1\%$ of the ACES emissions of NYC [135, 151] as shown in Figure 5.12. However, we do not account for ecosystem respiration and it may explain some of the differences between prior and posterior results. During the winter, Sargent et al. [124] estimated that ecosystem respiration contributed 5% of measured enhancements at a city-center measurement site in Boston, and up to 20% of the total flux within the wider domain. Similarly, Miller et al. [152] estimated biospheric emissions as 27% of total emissions for Los Angeles in winter. For context, the 2018-2019 average winter (November - March) temperature was 3.11 °C in Boston, 4.33 °C in NYC and 14.78 °C in Los Angeles based on airport temperature records [153].

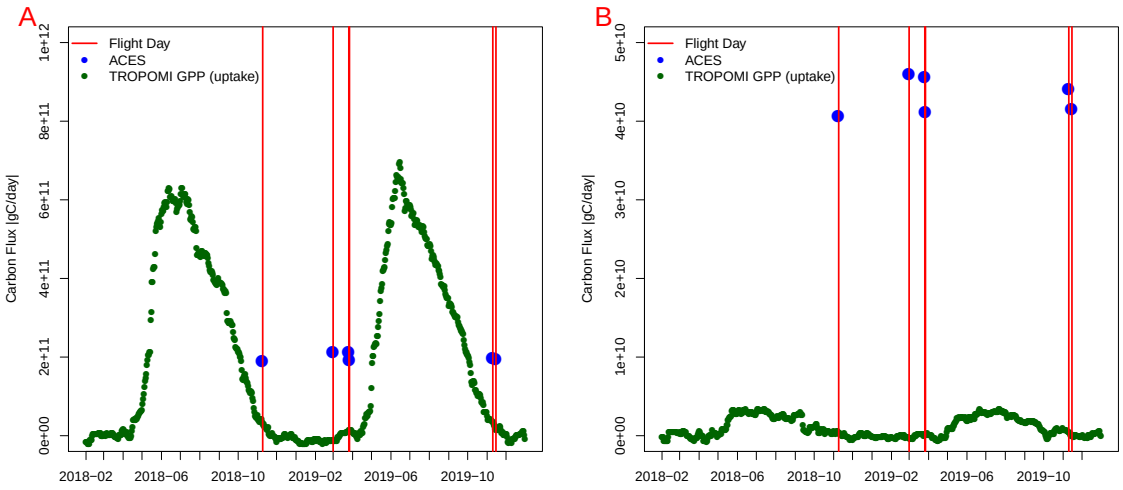

Figure 5.12. (A) Shows the total TROPOMI derived GPP across the domain for this study across 2018 and 2019. Days where a research flight was conducted are denoted by vertical red lines on the plot and blue dots on these lines represent the total ACES CO_2 emissions for the same domain. (B) the same as (A), but for the 5 boroughs of NYC instead of the larger domain. We believe that this is justification for not including a biospheric uptake component into the model calculations.

We report posterior emissions based on the range of results across the various MET, SF methods, flight days, and priors using the standard deviation across posteriors, one parameter at a time. These provide information about the variability in posterior emissions introduced by each of these aspects of the analysis. Given NARR and GDAS were discontinued partway through the flight campaign and had little impact on final results, they have been excluded in the plots and calculations below. The 2B posterior results are considerably lower than all other methods with an average $\pm$ 1σ posterior of 45 kmol/s $\pm$ 24 kmol/s compared to a posterior of 61 kmol/s $\pm$ 33 kmol/s for I_LR, the minimum across the remaining methods. This approach also generally results in a lower mean absolute error (MAE) than other methods. There are even cases where the 2B approach calculates a near 0 SF and

relies entirely on the linear correction to the background to optimize agreement between modeled and measured enhancements. This suggests that the 2B method may be overfitting the data and as such it has been excluded from analyses, although refining the uncertainties used in the approach may improve its performance in the future. The fit method has also been excluded from analyses as this approach is quite sensitive to cases with a low correlation between measured and modeled data, sometimes resulting in considerably different posteriors with high MAEs. Across all remaining parameters, the campaign average posterior for the five NYC boroughs is 67 $\pm$ 31 kmol/s (mean $\pm$ 1σ), with the bounds representing the variability across flight days (not the propagated method uncertainty, which would include uncertainty that the SF applies to NYC equally well). We have also repeated the analysis using ACES and Vulcan annual means rather than the hourly versions. The comparative results are shown in Figure 5.13.

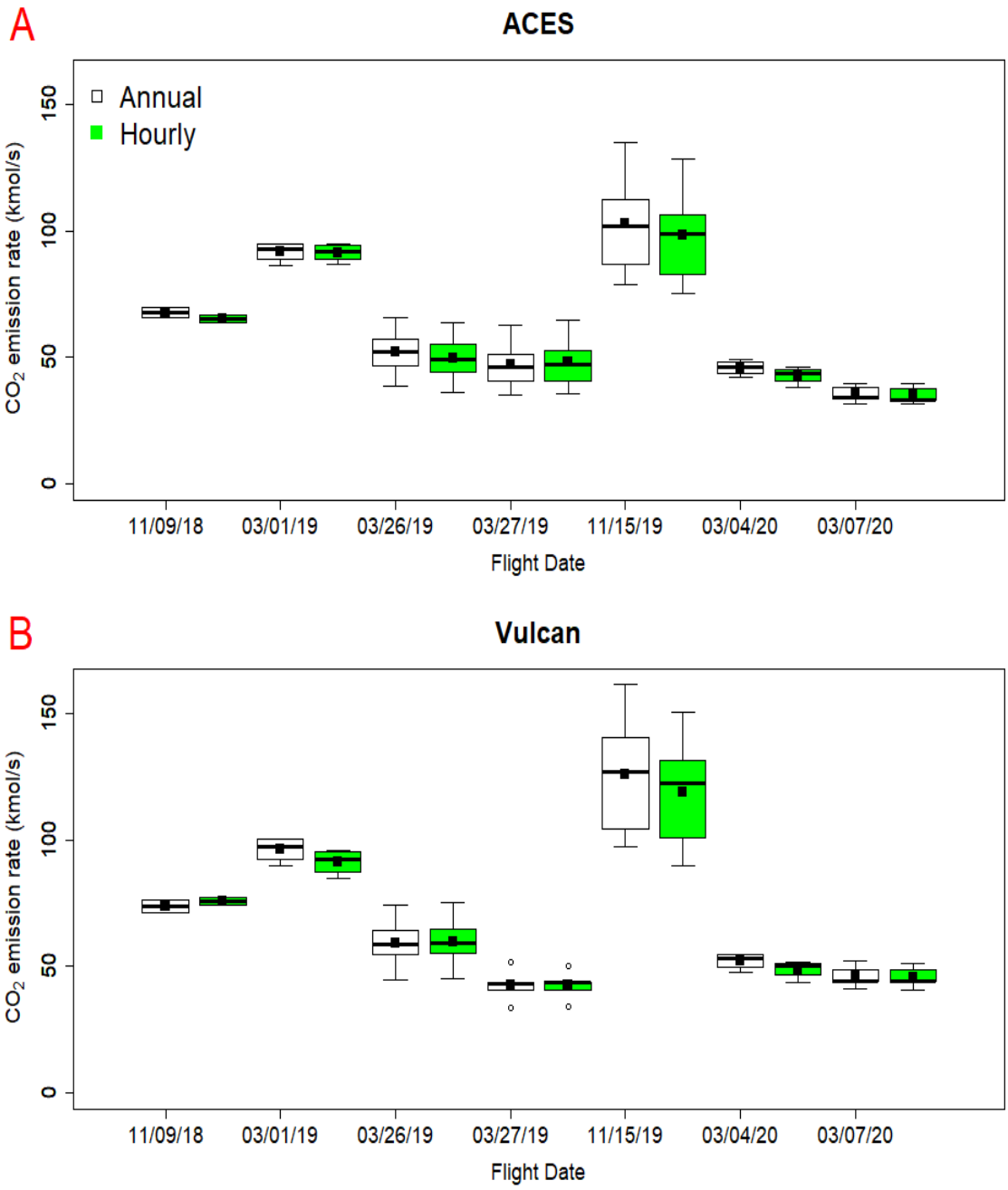

Figure 5.13. (A) ACES posterior results across flight days using both the annual and hourly priors. (B) Vulcan posterior results across flight days using both the annual and hourly priors. Bars indicate the 25th to 75th percentile, whiskers are up to 1.5 times the IQR, circles mark outliers (>1.5 x IQR), black lines represent the medians, and black squares represent the means.

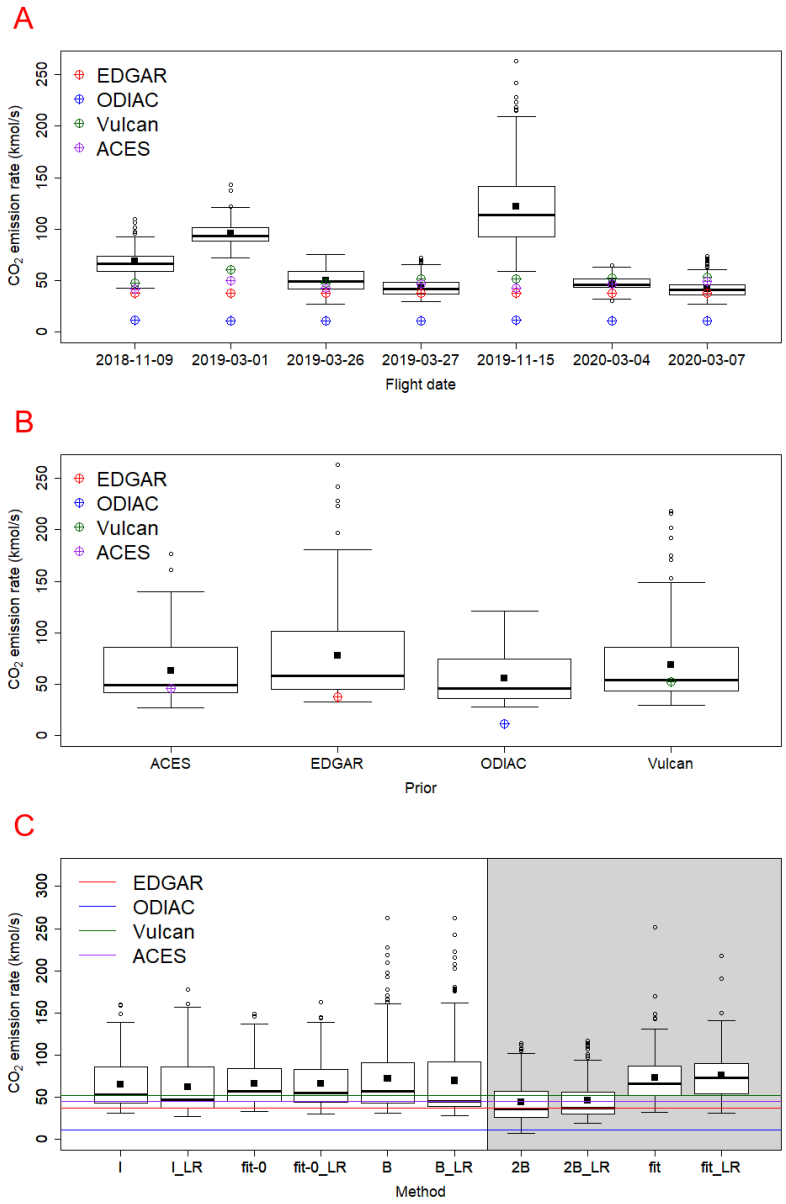

Figure 5.14. Boxplots of the ensemble of posterior CO_2 emission rates for NYC, grouped by (A) flight day, (B) prior, and (C) SF/background calculation method. Bars indicate the 25th to 75th percentile, whiskers are up to 1.5 times the IQR, circles mark outliers (>1.5 x IQR), black squares represent the means, and thick black lines the medians. Priors are also plotted as denoted by legends. Results using the linear background are labeled as _LR and the fit and 2B methods are in gray as they have been excluded from further analyses.

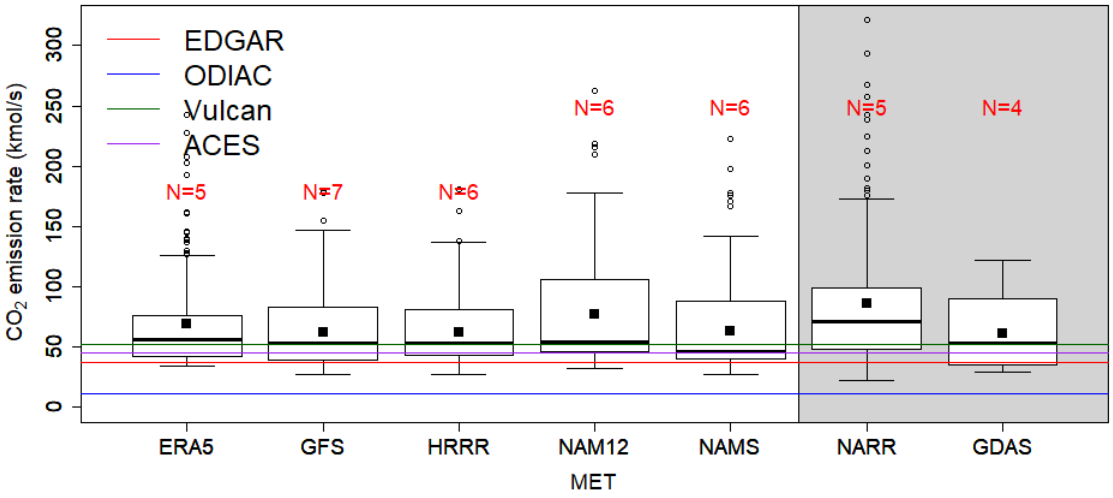

Figure 5.15. Boxplot of the posterior CO_2 emission rate for NYC grouped by MET in the same approach as Figure 5.14. N values above each box indicate how many flights included the MET, as some were excluded for particular flights and NARR and GDAS stopped being archived by NOAA midway through the campaign. NARR and GDAS are in grey as they are not used in any further analyses.

5.3.1 Emission rate variability

Although the campaign average posterior is nearly double the average across all priors, we calculated SFs that resulted in posteriors with relatively little variability with respect to prior. The average across all priors is 37 ± 18 kmol/s which is 49% variability among priors while the posterior variability with respect to prior choice is only 14% (Figure 5.14B). If looking only at Vulcan and ACES, the two bottom-up priors with high temporal and spatial resolution, the average prior emission rate is 49 kmol/s with a 13% difference between them and the percent difference in the posterior with respect to prior choice is 9%. The campaign mean posterior represents a 29% increase in the Vulcan prior, 47% increase in the ACES prior, 79% increase in the EDGAR prior, and a 499% increase in the ODIAC prior. These do not account for biospheric emissions and some error introduced by reprojection from the ACES/Vulcan projection to the latitude/longitude projection of footprints. As discussed earlier, that may explain some of this difference. It is also important to stress that the prior emissions used in this study are not estimates of the actual emissions at the time of the flights, therefore these factors do not represent a quantification of error in the prior emissions. Nevertheless, the large upscaling of the ODIAC prior (relative to the other three priors) is consistent with previous indications that ODIAC may underestimate emissions in dense cities in the northern U.S. due to nightlight saturation in urban cores [118, 154] and/or an underestimation of heating emissions that are not correlated with lighting [155].

The variability across the three SF calculation methods, including both background methods, is only 6% (Figure 5.14C). Separating the results by background method gives a campaign average of 68 kmol/s for the percentile method and 66 kmol/s for the linear method, both with 6% variability across SF methods. These results are within 1 sigma of one another, suggesting that the posterior is insensitive to the choice of background, at least in regard to these two methods and this set of flights. Excluding NARR and GDAS the variability across MET is 9% (Figure 5.15),

but this is driven largely by NAM12. The variability without NAM12 decreases to only 5%. Although NAM12 represents output from the same model as the NAMS data, we consider the additional variability it causes (which results from archiving the met data on a different temporal and vertical grid) to be a real source of transport model error in STILT. Therefore we consider the value of 9% to be representative of the variability due to transport model uncertainty.

The daily variability is 46%, making it the largest source of variability across the tested parameters (Fig 5.14A). These results are generally consistent with those calculated by Lopez-Coto et al. [107] for the Washington DC-Baltimore metropolitan area using several flights in an ensemble of inversions. Although the ensemble and methods used were different, the authors saw 33% daily variability, 7-15% variability across MET, and 11% variability across priors.

These variabilities are summarized in Table 5.3 and combined to provide overall uncertainties for the posteriors as in Lopez-Coto et al. [107]. Combining these terms assumes that they are independent sources of uncertainty, which is unlikely to be true. Additionally, the choice of ensemble members (MET, priors, etc.) could impact the ensemble spread across these parameters. Therefore, the estimated uncertainties may not represent the true method uncertainty, but they do still provide an estimate of the likely variability introduced by the various model choices. Combining these sources of uncertainty without the daily variability provides an estimate of the uncertainty for any single day's posterior estimate. If this SF approach is used over larger timescales to assess trends, then the daily variability becomes a relevant part of the posterior uncertainty, causing the uncertainty to increase considerably making it comparable to the uncertainties of mass balance approaches. While daily variability of the emissions themselves is expected, the posterior daily variability is larger than the one provided by ACES (20%) or Vulcan (20%) and thus, part of the observed posterior variability is most likely caused by sampling aliasing [107] and other sources. However, the daily variability could be reduced by averaging posterior emissions from a larger number of flights as long as sampling footprints are comparable, particularly if flights are

Table 5.3.
Sources of Variability

Source of Uncertainty	1σ (%)
Daily Variability	46
Prior Variability	14
SF and BG Variability	6
MET Variability	9
Combined Uncertainty (excluding daily variability)	18
Combined Uncertainty (including daily variability)	49

performed within a short timeframe to minimize variability in the source emissions [46, 107].

The SF ensemble approach used here avoids many of the issues faced when applying a mass balance method to calculate urban emissions, by directly relating emissions to a source area and prior using transport modeling. On the other hand, it is simpler to apply than a full inverse modelling approach making it useful for broad applications. Since the approach relies on different underlying assumptions it provides a good complement to these alternative methods. However, the SFs are very sensitive to a number of errors as shown by previous work [126] as well as here and, thus, a very careful model-data screening must be done in order to avoid large excursions in the estimations. Examples include: most SF approaches used require a high correlation between simulated and observed enhancements, any SF approach requires an accurate spatial distribution of prior emissions, and there must not be strong upwind sources outside the model domain. The ensemble approach used here can partially

minimize the influence of some of these limitations and thus it is preferred as opposed to a single SF - prior - MET combination.

Recently, however, a ∼30% bias in this approach was recognized based on evidence from comparisons to Bayesian inversion and MBE results using the same data. In addition to this unfavourable comparison, shown in Figure 5.16, the SF for the priors used was relatively high compared to recent literature that have seen broad agreement with Vulcan [107,156]. To investigate the source of this bias we ran a simple observing system simulation experiment (OSSE). Emissions were simulated from a large domain (see Figure 5.17) using annually averaged Vulcan emissions and the enhancements calculated were considered the observed dataset. Emissions were then simulated from a smaller domain (that used in this work) in the same manner and these enhancements were considered the simulated dataset. By keeping emissions constant in time, relying on the same transport model between the two datasets, and applying different known SFs to a small set of test flights we isolated the test to investigate solely the influence of upwind sources outside the domain. The calculated SFs were biased high by a comparable degree and work on addressing this is underway. Recalculating SFs using the larger domain alone did result in some improvement as can be seen in Figure 5.18, but some days so no change or even slightly higher posterior emissions. Current thoughts include attempting a nesting in which outside sources are accounted for before SFs are calculated (e.g. subtracting the simulated influence of outside sources from the measured concentrations before the analysis, including background calculation), and defining the area of interest (presently, the 5 NYC boroughs) as a larger area, likely defined based explicitly on the footprint itself. The OSSE dataset provides us with an opportunity to investigate the impact of changes like these on the performance of the SF technique.

We have assessed CO_2 emissions from NYC using aircraft observations using an SF ensemble approach based on 5 MET products, 4 priors, 2 background calculation methods, and 4 approaches to calculating the SF. Although the daily variability is too large to make a single posterior estimate from this campaign policy-relevant,

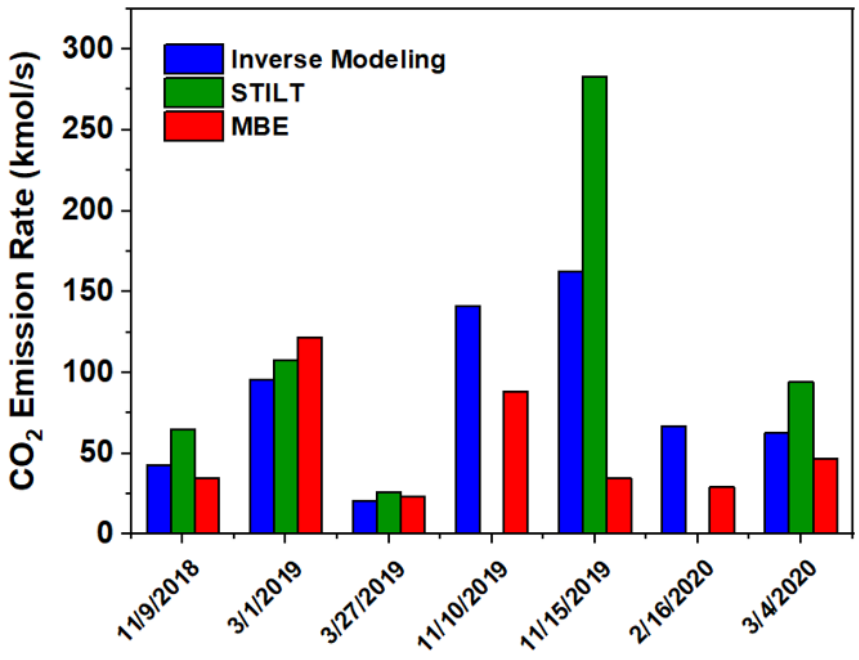

Figure 5.16. Barchart of the results across the MBE, Bayesian inversion, and SF approaches. All three approaches are calculated for a comparable footprint based on a simple accounting approach for the relevant surface emissions for the MBE results.

with a larger number of flights future campaigns may be able to reduce this variability to the point that the approach can be valuable in monitoring emission trends over time. We have explored in detail how the parameters varied in this ensemble impact the variability of posterior emissions, demonstrating the utility of this method. This also represents a set of data that can provide a solid pre-COVID anchor that will be useful in any analysis of shut-down conditions. Additional work directly comparing this approach to inversion and mass balance methods would also be of interest as these top down approaches continue to be employed and further refined. Lastly, this model-measurement approach will be particularly powerful when combined with long-term tower networks. Tower data are more heavily influenced by local emissions than airborne measurements. Flight data has a large footprint that makes it spatially representative, but it is only a snapshot of emissions representing discrete

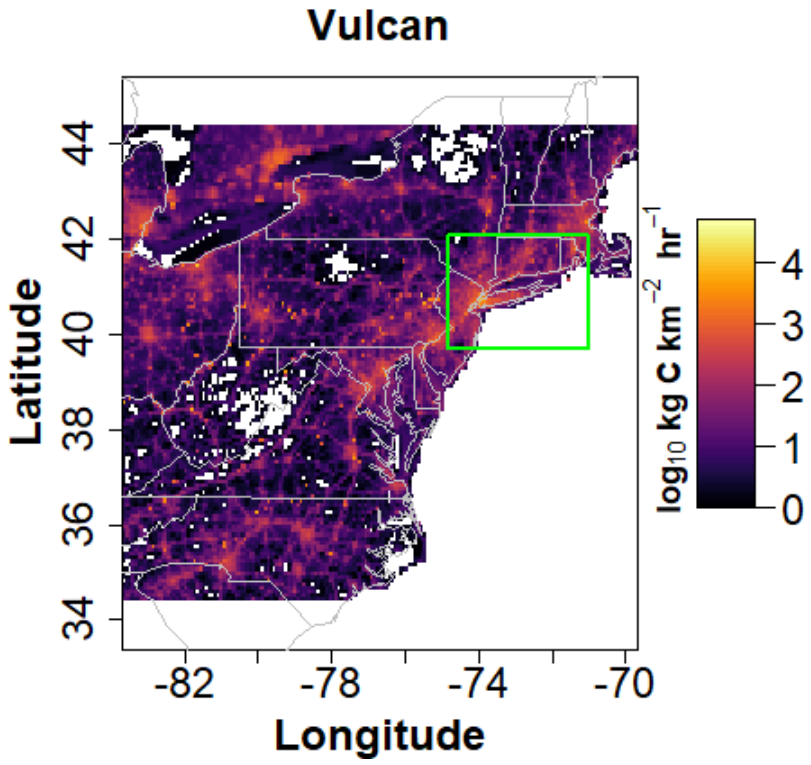

Figure 5.17. Annual Vulcan for the larger domain overlaid onto a sate map with the domain of this work highlighted in red.

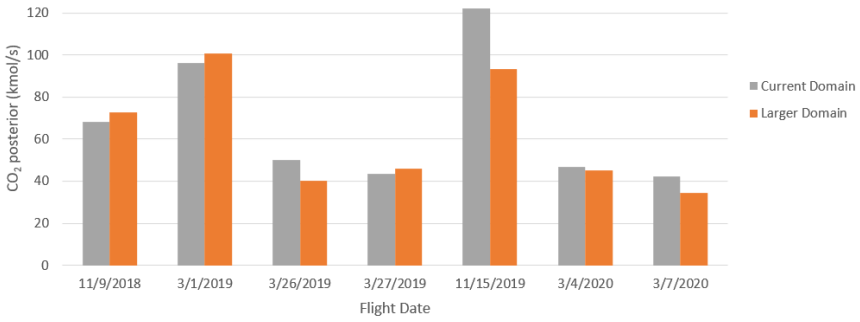

Figure 5.18. Barchart of the posterior results for the 5 boroughs of NYC using the large domain and using the domain discussed throughout this work. Some days see significant changes in posterior, but not all do.

times. Combining the two methods on days with flight observations can anchor tower networks with comparisons to ensure that tower networks do not suffer a spatial sampling bias compared to the spatially representative sampling of aircraft. Satellite data has also been used to estimate urban emissions [157–159] and could be incorporated into multi-platform analyses. Future work incorporating information from multiple sources should improve the coverage of city emissions and representativeness of results.

6. CONCLUSION & FUTURE WORKS

This thesis covers a large suite of MBEs downwind of power plants to quantify the CH_4 emissions of natural gas-fired facilities and to compare against CEMS reported CO_2 emissions, which are assumed to act as a semi-true value against which we assessed both the accuracy and precision of the MBE technique. Finally, NYC CO_2 emissions were quantified and component uncertainties investigated using a dispersion modeling scaling factor approach using flight data. Aircraft sampling enabled easy access to the often relatively remote power plants and ensured large, spatially representative sampling of the NYC urban area as shown in Figure 6.1.

The problem with airborne analyses, like most mobile platforms, is the infrequency of measurements. Aircraft typically measure in campaigns with only a handful of flights in close succession for the entire year. Each individual flight provides a snapshot view of that day's emissions, but tower and satellite platforms are able to measure far more frequently year-round. Furthermore, to ensure the assumption of atmospheric "stationarity" during sampling, most of the data produced by aircraft cover a period not wider than 11:00 am to 5:00 pm. Tower measurement systems are expensive to develop and operate so they are rarely developed into dense networks and they can have a relatively small footprint, i.e. they are more heavily influenced from nearby sources than airborne measurements. Then there are satellite measurements that often only provide a once-a-day measurement that are dependent on weather (cloud cover) and may have limited capabilities in terms of resolution and precision for complex urban domains [160]. Combining multiple measurement platforms in modeling approaches can not only add data to constrain results, but also allow some of these advantages and disadvantages to offset one another [160]. Satellites are also

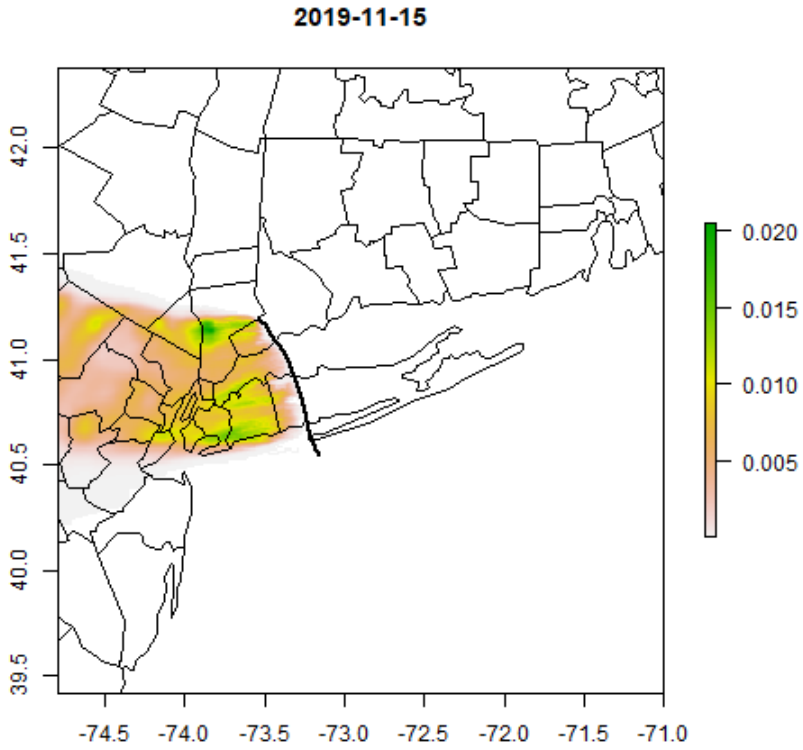

Figure 6.1. Example footprint from a single transect downwind of NYC. The thick black line is the transect path, and thin black lines represent county boundaries. Footprint units are ppm ($m^2s/\mu mol$). The average wind speed was 6.2 $\pm$ 1.3 m/s and the median altitude was 572 m.

quickly and continuously progressing to meet new demands. The current suite of CH_4 measuring satellites and those scheduled for launch is provided in Figure 6.2, although many of these measure a significantly larger suite of gases (e.g. TROPOMI measures nitrogen and sulfur dioxide, O_3, formaldehyde, CO, CH_4, etc.). As the number of satellites grow, there become opportunities for different niches. As shown in the lower panel of Figure 6.2, some satellites like GHGSat are designed for smaller areas, but high enough resolution to estimate point source emissions [161–163]. Other satellites provide a larger swath, but are of poorer resolution making quantification

limited to only large sources [164]. For example, TEMPO will be able to monitor daily variations in ozone, nitrogen dioxide, and other key elements of air pollution from the Atlantic to the Pacific, as a geostationary satellite focused on North America, as shown in Figure 6.3. The instrument will resolve pollution levels with a horizontal resolution of several square miles—far better than existing limits of about 100 square miles [165].

Satellite measurements can provide global data with relatively fast cycles (e.g. $\sim$1 day for TROPOMI to circle the globe) that can complement the surface measurement networks, particularly in developing regions with fewer measurement sites. This enables regional to global inversion analyses that can assimilate satellite measurements over the course of years, in some cases incorporating surface measurements as well to better constrain emissions across regions or to compare against satellite results [166]. Higher resolution satellite retrievals have even allowed for direct quantification of individual sources or source regions as summarized in Varon et al. [162]. Identifying an individual source can be difficult depending on noise and emission strength, as shown in Figure 6.4. The four methods currently available to calculate ERs are 1) a gaussian plume inversion approach that fits a gaussian plume model to the column enhancements, 2) a source pixel approach that uses column enhancements directly over the source in combination with the wind speed, 3) a cross sectional flux method that is comparable to the MBE approach used in this thesis, relying on a "transect" drawn through the plume with the ability to average results across multiple drawn transects, and 4) an integrated mass enhancement approach that uses the total size of the plume and wind speed [162]. Recent studies suggest that the latter two are more appropriate for high resolution column measurements as simulated data analyses showed that instantaneous plumes are too small to follow Gaussian behavior well and wind variability along with horizontal turbulent diffusion cause errors in the source pixel approach, although these are less relevant with coarser data as shown in Figure 6.5 [162]. This will continue to become a more viable approach as data coverage improves with both low resolution, large coverage satellites that can identify areas

of interest and high resolution, low coverage satellites that can quantify emissions, as summarized in Figure 6.2.

The majority of this thesis focuses on CO_2 measurements made in winter, to minimize the impact of biospheric uptake. However, respiration during the winter may also be non-negligible with estimates as large as 20% of for an urban region [124,152]. The biosphere, whether through respiration or uptake, complicates many analysis techniques as the edges may not provide an appropriate background any longer. Biosphere signal is unlikely to be comparable downwind of a large urban center and outside of said urban center, particularly for cities like Indianapolis that is surrounded by agricultural fields. The most common way to address this complicating effect, other than modeling the biosphere (which comes with its own additional uncertainties), is to use isotopic measurements of ^{14}C that can clearly distinguish fossil CO_2 [169]. Although seasonal biosphere uptake is not a concern for CH_4, distinguishing fossil sources (natural gas) from biogenic sources (landfills, wastewater treatment plants, etc.) is. Isotopes can be used for the same effect as with CO_2, but certain tracers (e.g. C_2H_6) can also be used to distinguish fossil fuel related CH_4 [170,171]. Certain CO_2 sources can similarly be distinguished using co-emitted tracers such as CO to identify combustion from on-road vehicles or particulates/black carbon to identify combustion from diesel vehicles [172].

The NYC SF analysis is currently being reanalyzed using additional methods. Two other members of the Shepson lab are analyzing the same set of flights using the MBE method, as discussed throughout this thesis, and using an inversion as briefly described in Chapter 5. Although all three methods are commonly used, comparisons across these approaches are still scarce [126]. Upon completion, the calculated posterior emissions and their variability can be directly compared across the inversion and SF approach in a straightforward manner. Comparing the MBE approach can be done, but is less straightforward. As mentioned in Chapter 5, defining the region being measured during an MBE is non-trivial. Currently, the intent is to use the footprints calculated for the SF method and inversion work to identify the

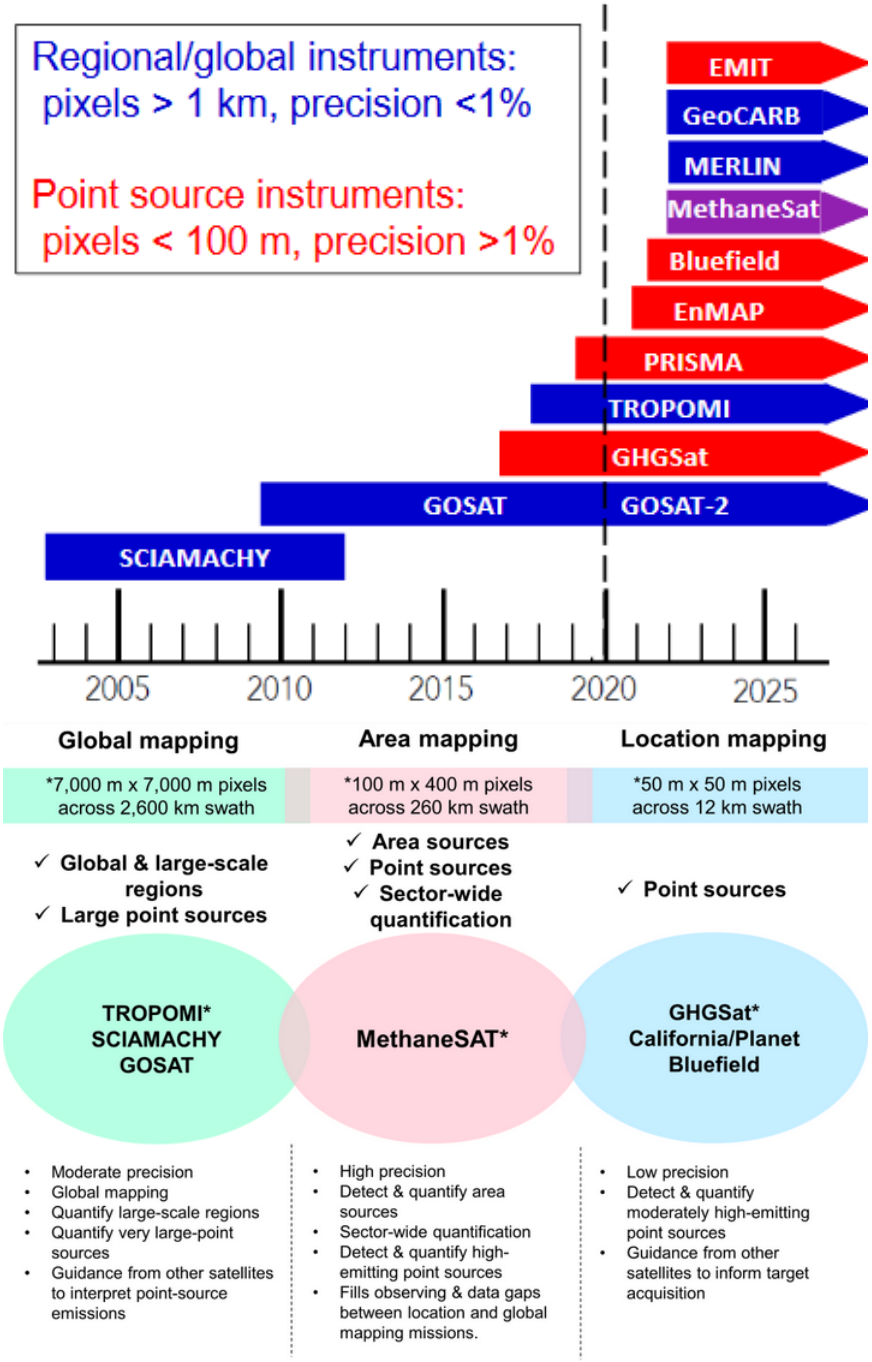

Figure 6.2. Timeline of current and scheduled satellites capable of CH_4 measurements. Figure from `http://acmg.seas.harvard.edu/presentations/2020/ams_methane.pdf` [167]. Below is a description of the capabilities of several of these satellites. Figure from `https://www.methanesat.org/fit-with-other-missions/` [168]

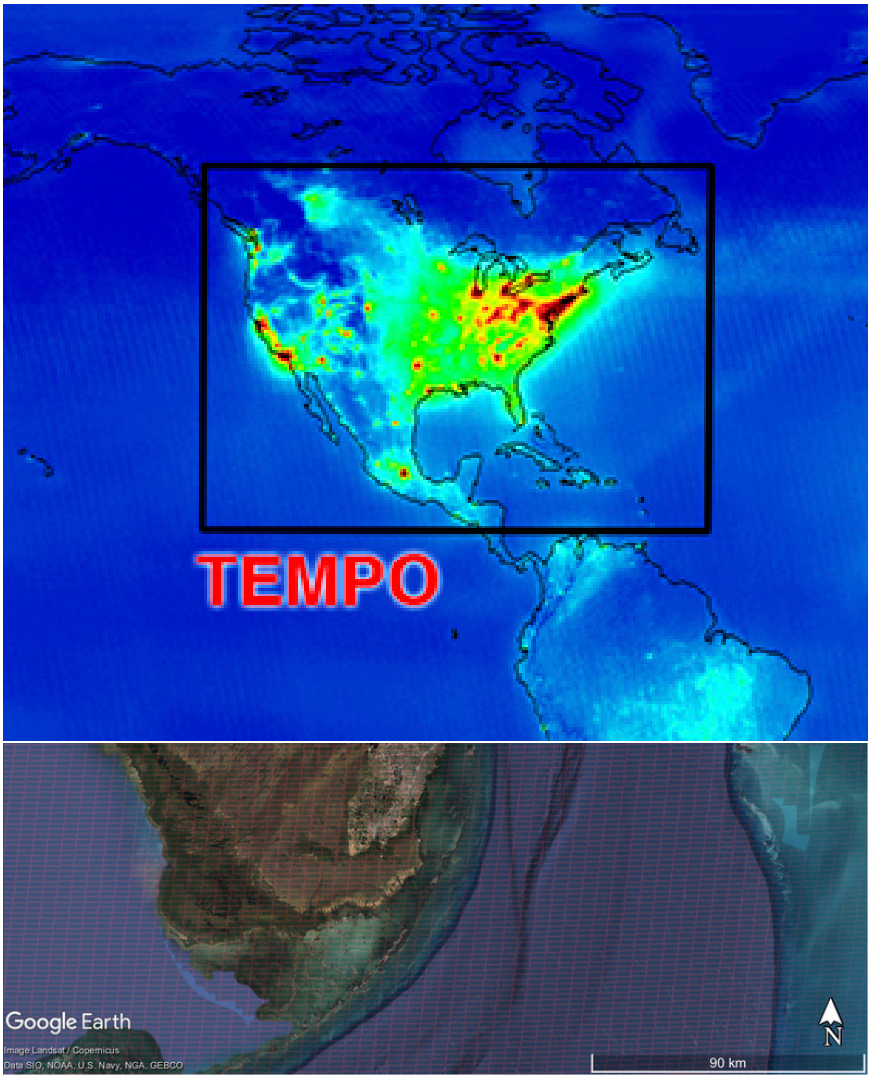

Figure 6.3. Image of TEMPO coverage and a visualization of the pixel size that it measures overlaid on a Google Earth Image (thin red lines) [165]

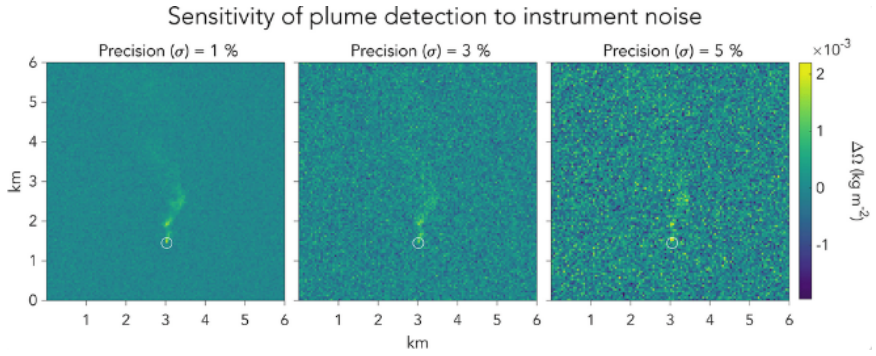

Figure 6.4. Column enhancements in a modeled point source of 1 ton/hr with varying instrumental precision. Figure 1 from Varon et al. [162].

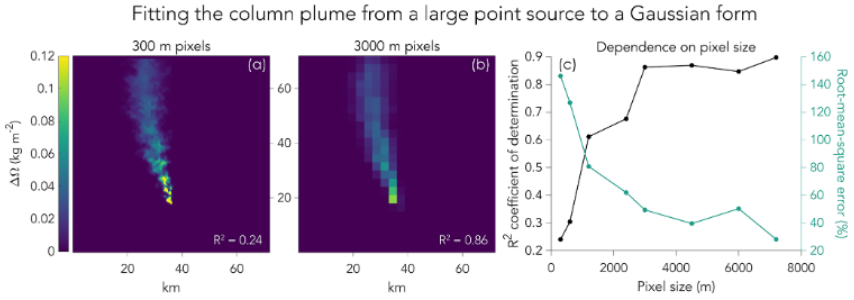

Figure 6.5. CO_2 column enhancements relative to a background for a 3.75 kton CO_2/hr simulated power plant plume at (A) 300 m resolution, and (B) averaged down to 3000 m resolution. (C) the R^2 and root mean square error (RMSE) of the ability to fit each plume to a Gaussian form. These show that the coarser dataset better fits a Gaussian dispersion. Figure 2 from Varon et al. [162].

region of high influence for the measurements. Once defined, the SF and inversion approaches can be recalculated for a different region rather easily. This process will likely need to be repeated for each flight day as the footprints are always significantly influenced by NYC, but different surrounding areas will be relevant depending on the wind speed and direction.

Similarly, this dataset, albeit unintentionally, represents a pre-COVID-19 baseline that can be used for recent studies aiming to understand the impact that COVID-

19 shutdown conditions have on emissions of CH_4 and CO_2. A collaborative effort analyzing DC-Baltimore and NYC involving three aircraft (University of Maryland, NOAA, and ALAR) began in April 2020, shortly after the shutdown began. This data is currently being analyzed using SF approaches comparable to those of Chapter 5 with possible inversion analyses being discussed.

REFERENCES

[1] Roland B. Stull. *An Introduction to Boundary Layer Meteorology*. Springer, Dordrecht, softcover reprint of the original 1st ed. 1988 edition, July 1988. viii, 1, 2, 4, 37, 82

[2] Lorraine Boissoneault. The Deadly Donora Smog of 1948 Spurred Environmental Protection—But Have We Forgotten the Lesson? 2

[3] Anne M. Thompson. The oxidizing capacity of the earths atmosphere: Probable past and future changes. *Science*, 256(5060):1157–1165, 1992. 4

[4] IPCC, 2018: Annex I: Glossary. *Global Warming of 1.5°C. An IPCC Special Report on the impacts of global warming of 1.5°C above pre-industrial levels and related global greenhouse gas emission pathways, in the context of strengthening the global response to the threat of climate change, sustainable development, and efforts to eradicate poverty*, (In Press). 5

[5] UNFCCC. `https://unfccc.int/`. 5, 25, 26

[6] Andrew A. Lacis, Gavin A. Schmidt, David Rind, and Reto A. Ruedy. Atmospheric CO_2: Principal Control Knob Governing Earth's Temperature. *Science*, 330(6002):356, October 2010. 6, 13

[7] Climate Change 2013: The Physical Science Basis. Contribution of Working Group I to the Fifth Assessment Report of the Intergovernmental Panel on Climate Change. Technical report, Cambridge University Press, Cambridge, United Kingdom and New Yok, NY, USA. vii, viii, ix, x, 6, 7, 8, 9, 12, 13, 16, 17, 18, 19, 20, 21, 49, 89

[8] Henning Rodhe, Robert Charlson, and Elisabeth Crawford. Svante Arrhenius and the Greenhouse Effect. *Ambio*, 26(1):2–5, 1997. 6

[9] K. von Schuckmann, L. Cheng, M. D. Palmer, J. Hansen, C. Tassone, V. Aich, S. Adusumilli, H. Beltrami, T. Boyer, F. J. Cuesta-Valero, D. Desbruyères, C. Domingues, A. García-García, P. Gentine, J. Gilson, M. Gorfer, L. Haimberger, M. Ishii, G. C. Johnson, R. Killick, B. A. King, G. Kirchengast, N. Kolodziejczyk, J. Lyman, B. Marzeion, M. Mayer, M. Monier, D. P. Monselesan, S. Purkey, D. Roemmich, A. Schweiger, S. I. Seneviratne, A. Shepherd, D. A. Slater, A. K. Steiner, F. Straneo, M.-L. Timmermans, and S. E. Wijffels. Heat stored in the Earth system: Where does the energy go? *Earth System Science Data*, 12(3):2013–2041, 2020. ix, 6, 10

[10] The Cataclysmic 1991 Eruption of Mount Pinatubo, Philippines, Fact Sheet 113-97. https://pubs.usgs.gov/fs/1997/fs113-97/#:~:text=Nearly%2020%20million%20tons%20of%20sulfur%20dioxide%20were,central%20Luzon%2C%20home%20to%20about%203%20million%20people. 6

[11] C. Donald Ahrens. *Essentials of Meteorology: An Invitation to the Atmosphere*. Thomson Brooks/Cole, fifth edition. ix, 11

[12] Climate Science Investigations South Florida - Energy: The Driver of Climate. ix, 11

[13] F. Joos, R. Roth, J. S. Fuglestvedt, G. P. Peters, I. G. Enting, W. von Bloh, V. Brovkin, E. J. Burke, M. Eby, N. R. Edwards, T. Friedrich, T. L. Frölicher, P. R. Halloran, P. B. Holden, C. Jones, T. Kleinen, F. T. Mackenzie, K. Matsumoto, M. Meinshausen, G.-K. Plattner, A. Reisinger, J. Segschneider, G. Shaffer, M. Steinacher, K. Strassmann, K. Tanaka, A. Timmermann, and A. J. Weaver. Carbon dioxide and climate impulse response functions for the computation of greenhouse gas metrics: A multi-model analysis. *Atmospheric Chemistry and Physics*, 13(5):2793–2825, 2013. 13

[14] NOAA US Department of Commerce. Global Monitoring Laboratory - Carbon Cycle Greenhouse Gases. https://www.esrl.noaa.gov/gmd/ccgg/trends_ch4/. ix, 14

[15] NOAA US Department of Commerce. NOAA/ESRL Global Monitoring Laboratory - THE NOAA ANNUAL GREENHOUSE GAS INDEX (AGGI). https://www.esrl.noaa.gov/gmd/aggi/aggi.html. ix, 15

[16] The Keeling Curve. x, 16, 18

[17] P. P. Tans, A. F. M. De Jong, and W. G. Mook. Natural atmospheric 14C variation and the Suess effect. *Nature*, 280(5725):826–828, August 1979. 16

[18] NOAA US Department of Commerce. Global Monitoring Laboratory - Carbon Cycle Greenhouse Gases. https://www.esrl.noaa.gov/gmd/outreach/isotopes/c14tellsus.html. 16

[19] D. M. Etheridge, L. P. Steele, R. J. Francey, and R. L. Langenfelds. Atmospheric methane between 1000 A.D. and present: Evidence of anthropogenic emissions and climatic variability. *Journal of Geophysical Research: Atmospheres*, 103(D13):15979–15993, 1998. 16

[20] Tracking fossil fuel emissions with carbon-14 - Welcome to NOAA Research. https://research.noaa.gov/article/ArtMID/587/ArticleID/2631/Fingerprinting-fossil-fuel-emissions-with-carbon-14#:~:text=%22Bottom-up%22%20estimates%2C%20such%20as%20those%20used%20in%20the,the%20surface%20source%20regions%20with%20the%20measurement%20locations. 19

[21] U.S. EPA. Overview of Greenhouse Gases. https://www.epa.gov/ghgemissions/overview-greenhouse-gases, December 2015. 19, 49

[22] Ramón A. Alvarez, Daniel Zavala-Araiza, David R. Lyon, David T. Allen, Zachary R. Barkley, Adam R. Brandt, Kenneth J. Davis, Scott C. Herndon, Daniel J. Jacob, Anna Karion, Eric A. Kort, Brian K. Lamb, Thomas Lauvaux, Joannes D. Maasakkers, Anthony J. Marchese, Mark Omara, Stephen W. Pacala, Jeff Peischl, Allen L. Robinson, Paul B. Shepson, Colm Sweeney, Amy Townsend-Small, Steven C. Wofsy, and Steven P. Hamburg. Assessment of methane emissions from the U.S. oil and gas supply chain. *Science*, page eaar7204, June 2018. 19, 21, 50, 58

[23] Timothy L. Vaughn, Clay S. Bell, Cody K. Pickering, Stefan Schwietzke, Garvin A. Heath, Gabrielle Pétron, Daniel J. Zimmerle, Russell C. Schnell, and Dag Nummedal. Temporal variability largely explains top-down/bottom-up difference in methane emission estimates from a natural gas production region. *Proceedings of the National Academy of Sciences*, 115(46):11712–11717, 2018. 21

[24] OAR US EPA. Climate Change Indicators: Lyme Disease. `https://www.epa.gov/climate-indicators/climate-change-indicators-lyme-disease`, July 2016. 22

[25] Biodiversity and Health. `https://www.who.int/news-room/fact-sheets/detail/biodiversity-and-health`. 22

[26] Climate change and health. `https://www.who.int/news-room/fact-sheets/detail/climate-change-and-health`. 22

[27] Climate Change 2014: Impacts, Adaptation, and Vulnerability. Part A: Global and Sectoral Aspects. Contribution of Working Group II to the Fifth Assessment Report of the Intergovernmental Panel on Climate Change. Technical report, Cambridge University Press, Cambridge, United Kingdom and New Yok, NY, USA. vii, 23

[28] Observations: Atmosphere and Surface. In Climate Change 2013: The Physical Science Basis. Contribution of Working Group I to the Fifth Assessment Report of the Intergovernmental Panel on Climate Change. Technical report, Cambridge University Press, Cambridge, United Kingdom and New Yok, NY, USA. x, 24

[29] Thomas Knutson, Suzana J. Camargo, Johnny C. L. Chan, Kerry Emanuel, Chang-Hoi Ho, James Kossin, Mrutyunjay Mohapatra, Masaki Satoh, Masato Sugi, Kevin Walsh, and Liguang Wu. Tropical Cyclones and Climate Change Assessment: Part II: Projected Response to Anthropogenic Warming. *Bulletin of the American Meteorological Society*, 101(3):E303–E322, March 2020. 22, 24

[30] Paul L. Lucas, Detlef P. van Vuuren, Jos G.J. Olivier, and Michel G.J. den Elzen. Long-term reduction potential of non-CO2 greenhouse gases. *Environmental Science & Policy*, 10(2):85–103, 2007. 24, 25

[31] Thomas Lauvaux, Natasha L. Miles, Aijun Deng, Scott J. Richardson, Maria O. Cambaliza, Kenneth J. Davis, Brian Gaudet, Kevin R. Gurney, Jianhua Huang, Darragh O'Keefe, Yang Song, Anna Karion, Tomohiro Oda, Risa Patarasuk, Igor Razlivanov, Daniel Sarmiento, Paul Shepson, Colm Sweeney, Jocelyn Turnbull, and Kai Wu. High-resolution atmospheric inversion of urban CO_2 emissions during the dormant season of the Indianapolis Flux Experiment (INFLUX). *Journal of Geophysical Research: Atmospheres*, 121(10):5213–5236, May 2016. 26, 90, 91

[32] K. E. Garman, K. A. Hill, P. Wyss, M. Carlsen, J. R. Zimmerman, B. H. Stirm, T. Q. Carney, R. Santini, and P. B. Shepson. An Airborne and Wind Tunnel Evaluation of a Wind Turbulence Measurement System for Aircraft-Based Flux Measurements. *Journal of Atmospheric and Oceanic Technology*, 23(12):1696–1708, December 2006. 28, 76, 92

[33] Karl E. Garman, Phil Wyss, Mark Carlsen, James R. Zimmerman, Brian H. Stirm, Thomas Q. Carney, Robert Santini, and Paul B. Shepson. The Contribution of Variability of Lift-induced Upwash to the Uncertainty in Vertical Winds Determined from an Aircraft Platform. *Boundary-Layer Meteorology*, 126(3):461–476, March 2008. 28, 76, 92

[34] Karl Edwin Garman. *Precision of airborne wind measurement for atmospheric flight research*. Ph.D. Thesis, Purdue University, United States – Indiana, 2009. 28, 47

[35] E. R. Crosson. A cavity ring-down analyzer for measuring atmospheric levels of methane, carbon dioxide, and water vapor. *Applied Physics B*, 92(3):403–408, September 2008. x, 28, 31, 32, 33, 76, 92

[36] Tara I. Yacovitch, Scott C. Herndon, Joseph R. Roscioli, Cody Floerchinger, Ryan M. McGovern, Michael Agnese, Gabrielle Pétron, Jonathan Kofler, Colm Sweeney, Anna Karion, Stephen A. Conley, Eric A. Kort, Lars Nähle, Marc Fischer, Lars Hildebrandt, Johannes Koeth, J. Barry McManus, David D. Nelson, Mark S. Zahniser, and Charles E. Kolb. Demonstration of an Ethane Spectrometer for Methane Source Identification. *Environmental Science & Technology*, 48(14):8028–8034, July 2014. 29

[37] J.B. McManus, J.H. Shorter, D.D. Nelson, M.S. Zahniser, D.E. Glenn, and R.M. McGovern. Pulsed quantum cascade laser instrument with compact design for rapid, high sensitivity measurements of trace gases in air. *Applied Physics B*, 92(3):387–392, September 2008. x, 29, 30

[38] Jeremy J. Harrison, Nicholas D.C. Allen, and Peter F. Bernath. Infrared absorption cross sections for ethane (C2H6) in the 3 μm region. *Journal of Quantitative Spectroscopy and Radiative Transfer*, 111(3):357–363, February 2010. 29

[39] Isobel J. Simpson, Mads P. Sulbaek Andersen, Simone Meinardi, Lori Bruhwiler, Nicola J. Blake, Detlev Helmig, F. Sherwood Rowland, and Donald R. Blake. Long-term decline of global atmospheric ethane concentrations and implications for methane. *Nature*, 488(7412):490–494, August 2012. 29

[40] B. D. Hall, G. S. Dutton, and J. W. Elkins. The NOAA nitrous oxide standard scale for atmospheric observations. *Journal of Geophysical Research*, 112(D9), May 2007. 30

[41] Ethane. https://webbook.nist.gov/cgi/cbook.cgi?ID=C74840&Type=IR-SPEC&Index=0. x, 31

[42] Accurate Greenhouse Gas Measurements in Humid Gas Streams Using the G1301 Carbon Dioxide / Methane / Water Vapor Gas Concentration Analyzer - G1301 — Picarro. https://www.picarro.com/support/library/documents/accurate_greenhouse_gas_measurements_in_humid_gas_streams_using_the_g1301. 31

[43] Picarro. https://www.picarro.com/company/technology/crds. xi, 34

[44] Tegan N. Lavoie, Paul B. Shepson, Maria O. L. Cambaliza, Brian H. Stirm, Anna Karion, Colm Sweeney, Tara I. Yacovitch, Scott C. Herndon, Xin Lan, and David Lyon. Aircraft-Based Measurements of Point Source Methane Emissions in the Barnett Shale Basin. *Environmental Science & Technology*, 49(13):7904–7913, July 2015. 37, 50, 52, 75

[45] D. Y. Ahn, J. R. Hansford, S. T. Howe, X. R. Ren, R. J. Salawitch, N. Zeng, M. D. Cohen, B. Stunder, O. E. Salmon, P. B. Shepson, K. R. Gurney, T. Oda, I. Lopez-Coto, J. Whetstone, and R. R. Dickerson. Fluxes of Atmospheric Greenhouse-Gases in Maryland (FLAGG-MD): Emissions of Carbon Dioxide in the Baltimore, MD-Washington, D.C. Area. *Journal of Geophysical Research: Atmospheres*, 125(9):e2019JD032004, 2020. 37, 38, 42, 75, 76, 77, 91

[46] Alexie M. F. Heimburger, Rebecca M. Harvey, Paul B. Shepson, Brian H. Stirm, Chloe Gore, Jocelyn Turnbull, Maria O. L. Cambaliza, Olivia E. Salmon, Anna-Elodie M. Kerlo, Tegan N. Lavoie, Kenneth J. Davis, Thomas Lauvaux, Anna Karion, Colm Sweeney, W. Alan Brewer, R. Michael Hardesty, and Kevin R. Gurney. Assessing the optimized precision of the aircraft mass balance method for measurement of urban greenhouse gas emission rates through averaging. *Elem Sci Anth*, 5(0):26, June 2017. 37, 38, 39, 76, 77, 91, 92, 105, 122

[47] Joseph Pitt, Grant Allen, Stéphane Bauguitte, Martin Gallagher, James Lee, Will Drysdale, Bethany Nelson, Alistair Manning, and Paul Palmer. Assessing London CO_2, CH_4 and CO emissions using aircraft measurements and dispersion modelling. *Atmospheric Chemistry and Physics Discussions*, pages 1–22, October 2018. 37, 41, 90, 91

[48] Anna Karion, Colm Sweeney, Eric A. Kort, Paul B. Shepson, Alan Brewer, Maria Cambaliza, Stephen A. Conley, Ken Davis, Aijun Deng, Mike Hardesty, Scott C. Herndon, Thomas Lauvaux, Tegan Lavoie, David Lyon, Tim Newberger, Gabrielle Pétron, Chris Rella, Mackenzie Smith, Sonja Wolter, Tara I. Yacovitch, and Pieter Tans. Aircraft-Based Estimate of Total Methane Emissions from the Barnett Shale Region. *Environmental Science & Technology*, 49(13):8124–8131, July 2015. 37, 42, 50, 75

[49] Kelly L. Mays, Paul B. Shepson, Brian H. Stirm, Anna Karion, Colm Sweeney, and Kevin R. Gurney. Aircraft-Based Measurements of the Carbon Footprint of Indianapolis. *Environmental Science & Technology*, 43(20):7816–7823, October 2009. 37, 52, 75, 76

[50] M. O. L. Cambaliza, P. B. Shepson, D. R. Caulton, B. Stirm, D. Samarov, K. R. Gurney, J. Turnbull, K. J. Davis, A. Possolo, A. Karion, C. Sweeney, B. Moser, A. Hendricks, T. Lauvaux, K. Mays, J. Whetstone, J. Huang, I. Razlivanov, N. L. Miles, and S. J. Richardson. Assessment of uncertainties of an aircraft-based mass balance approach for quantifying urban greenhouse gas emissions. *Atmospheric Chemistry and Physics*, 14(17):9029–9050, September 2014. 37, 38, 39, 44, 46, 52, 75, 76, 86, 90, 91, 92

[51] M. O. L. Cambaliza, P. B. Shepson, J. Bogner, D. R. Caulton, B. Stirm, C. Sweeney, S. A. Montzka, K. R. Gurney, K. Spokas, O. E. Salmon, T. N. Lavoie, A. Hendricks, K. Mays, J. Turnbull, B. R. Miller, T. Lauvaux, K. Davis, A. Karion, B. Moser, C. Miller, C. Obermeyer, J. Whetstone, K. Prasad, N. Miles, and S. Richardson. Quantification and source apportionment of the methane emission flux from the city of Indianapolis. *Elem Sci Anth*, 3(0), January 2015. 37, 52, 75, 76

[52] Alexie M. F. Heimburger, Rebecca M. Harvey, Paul B. Shepson, Brian H. Stirm, Chloe Gore, Jocelyn Turnbull, Maria O. L. Cambaliza, Olivia E. Salmon, Anna-Elodie M. Kerlo, Tegan N. Lavoie, Kenneth J. Davis, Thomas Lauvaux, Anna Karion, Colm Sweeney, W. Alan Brewer, R. Michael Hardesty, and Kevin R. Gurney. Assessing the optimized precision of the aircraft mass balance method for measurement of urban greenhouse gas emission rates through averaging. *Elem Sci Anth*, 5(0):26, June 2017. 38, 53, 75, 86

[53] Xinrong Ren, Olivia E. Salmon, Jonathan R. Hansford, Doyeon Ahn, Dolly Hall, Sarah E. Benish, Phillip R. Stratton, Hao He, Sayantan Sahu, Courtney Grimes, Alexie M. F. Heimburger, Cory R. Martin, Mark D. Cohen, Barbara Stunder, Ross J. Salawitch, Sheryl H. Ehrman, Paul B. Shepson, and Russell R. Dickerson. Methane Emissions From the Baltimore-Washington Area Based on Airborne Observations: Comparison to Emissions Inventories. *Journal of Geophysical Research: Atmospheres*, 123(16):8869–8882, 2018. 38, 75, 77, 91

[54] Dezhang Chu. The GLOBEC Kriging Software Package - EasyKrig3. `http://globec.whoi.edu/software/kriging/easy_krig/easy_krig.html`. The Woods Hole Oceanographic Institution. vii, 39, 44, 46

[55] Stephen Conley, Ian Faloona, Shobhit Mehrotra, Maxime Suard, Donald H. Lenschow, Colm Sweeney, Scott Herndon, Stefan Schwietzke, Gabrielle Pétron, Justin Pifer, Eric A. Kort, and Russell Schnell. Application of Gauss's theorem to quantify localized surface emissions from airborne measurements of wind and trace gases. *Atmospheric Measurement Techniques*, 10(9):3345–3358, September 2017. 41, 53, 55, 75, 76

[56] Ju-Mee Ryoo, Laura T. Iraci, Tomoaki Tanaka, Josette E. Marrero, Emma L. Yates, Inez Fung, Anna M. Michalak, Jovan Tadić, Warren Gore, T. Paul Bui, Jonathan M. Dean-Day, and Cecilia S. Chang. Quantification of CO_2 and CH_4 emissions over Sacramento, California, based on divergence theorem using aircraft measurements. *Atmospheric Measurement Techniques*, 12(5):2949–2966, May 2019. 41, 75

[57] Diethelm Wuertz, Tobias Setz, and Yohan Chalabi. *fBasics: Rmetrics - Markets and Basic Statistics*. 2017. vii, 44, 46

[58] Tony Plate and Richard Heiberger. *abind: Combine Multidimensional Arrays*. 2016. vii, 44, 46

[59] Douglas Nychka, Dorit Hammerling, Stephan Sain, and Nathan Lenssen. *LatticeKrig: Multiresolution Kriging Based on Markov Random Fields*. University Corporation for Atmospheric Research, Boulder, CO, USA, 2016. vii, 44, 46

[60] U.S. EIA. Review of Emerging Resources: U.S. Shale Gas and Shale Oil Plays. `https://www.eia.gov/analysis/studies/usshalegas/`, July 2011. 49

[61] Robert W. Howarth. A bridge to nowhere: methane emissions and the greenhouse gas footprint of natural gas. *Energy Science & Engineering*, 2(2):47–60, June 2014. 49, 52

[62] U.S. EIA. Electricity Data Browser - Net Generation for Electric Power. `https://www.eia.gov/electricity/data/browser/#/topic/0?agg=2,0,1&fuel=9&geo=g&sec=008&linechart=ELEC.GEN.COW-US-98.A~ELEC.GEN.NG-US-98.A&columnchart=ELEC.GEN.COW-US-98.A&map=ELEC.GEN.COW-US-98.A&freq=A&ctype=linechart&ltype=pin&rtype=s&maptype=0&rse=0&pin=`. xi, 49, 50

[63] U.S. EIA. Carbon Dioxide Emissions Coefficients by Fuel. `https://www.eia.gov/environment/emissions/co2_vol_mass.php`. 49

[64] U.S. EPA. GHGRP Yearly Overview. `https://www.epa.gov/ghgreporting/ghgrp-yearly-overview`, July 2015. 49

[65] U.S. EPA. GHGRP Reported Data. `https://www.epa.gov/ghgreporting/ghgrp-reported-data`, August 2016. 49

[66] Climate Change 2013: The Physical Science Basis. Contribution of Working Group I to the Fifth Assessment Report of the Intergovernmental Panel on Climate Change. Technical report, Cambridge University Press, Cambridge, United Kingdom and New Yok, NY, USA. 49

[67] A. R. Brandt, G. A. Heath, E. A. Kort, F. O'Sullivan, G. Pétron, S. M. Jordaan, P. Tans, J. Wilcox, A. M. Gopstein, D. Arent, S. Wofsy, N. J. Brown, R. Bradley, G. D. Stucky, D. Eardley, and R. Harriss. Methane Leaks from North American Natural Gas Systems. *Science*, 343(6172):733–735, February 2014. 50, 52

[68] Ramón A. Alvarez, Stephen W. Pacala, James J. Winebrake, William L. Chameides, and Steven P. Hamburg. Greater focus needed on methane leakage from natural gas infrastructure. *Proceedings of the National Academy of Sciences*, 109(17):6435–6440, April 2012. 50, 52

[69] Shobhit Mehrotra, Ian Faloona, Maxime Suard, Stephen Conley, and Marc L. Fischer. Airborne Methane Emission Measurements for Selected Oil and Gas Facilities Across California. *Environmental Science & Technology*, 51(21):12981–12987, November 2017. 50

[70] Brian K. Lamb, Maria O. L. Cambaliza, Kenneth J. Davis, Steven L. Edburg, Thomas W. Ferrara, Cody Floerchinger, Alexie M. F. Heimburger, Scott Herndon, Thomas Lauvaux, Tegan Lavoie, David R. Lyon, Natasha Miles, Kuldeep R. Prasad, Scott Richardson, Joseph Robert Roscioli, Olivia E. Salmon, Paul B. Shepson, Brian H. Stirm, and James Whetstone. Direct and Indirect Measurements and Modeling of Methane Emissions in Indianapolis, Indiana. *Environmental Science & Technology*, 50(16):8910–8917, August 2016. 50

[71] Stefan Schwietzke, Gabrielle Pétron, Stephen Conley, Cody Pickering, Ingrid Mielke-Maday, Edward J. Dlugokencky, Pieter P. Tans, Tim Vaughn, Clay Bell, Daniel Zimmerle, Sonja Wolter, Clark W. King, Allen B. White, Timothy Coleman, Laura Bianco, and Russell C. Schnell. Improved Mechanistic Understanding of Natural Gas Methane Emissions from Spatially Resolved Aircraft Measurements. *Environmental Science & Technology*, 51(12):7286–7294, June 2017. 50

[72] Daniel Zavala-Araiza, Ramón A Alvarez, David R. Lyon, David T. Allen, Anthony J. Marchese, Daniel J. Zimmerle, and Steven P. Hamburg. Super-emitters in natural gas infrastructure are caused by abnormal process conditions. *Nature Communications*, 8:14012, January 2017. 50

[73] Tegan N. Lavoie, Paul B. Shepson, Chloe A. Gore, Brian H. Stirm, Robert Kaeser, Bernard Wulle, David Lyon, and Joseph Rudek. Assessing the Methane Emissions from Natural Gas-Fired Power Plants and Oil Refineries. *Environmental Science & Technology*, 51(6):3373–3381, March 2017. 50, 52, 53, 55, 56, 59, 71, 75, 77

[74] David R. Lyon, Ramón A. Alvarez, Daniel Zavala-Araiza, Adam R. Brandt, Robert B. Jackson, and Steven P. Hamburg. Aerial Surveys of Elevated Hydrocarbon Emissions from Oil and Gas Production Sites. *Environmental Science & Technology*, 50(9):4877–4886, May 2016. 50

[75] J. Peischl, T. B. Ryerson, J. S. Holloway, D. D. Parrish, M. Trainer, G. J. Frost, K. C. Aikin, S. S. Brown, W. P. Dubé, H. Stark, and F. C. Fehsenfeld. A top-down analysis of emissions from selected Texas power plants during TexAQS 2000 and 2006. *Journal of Geophysical Research*, 115(D16), August 2010. 50, 74, 76

[76] Marc L. Fischer, Wanyu Rengie Chan, Woody Delp, Seongeun Jeong, Vi H. Rapp, and Zhimin Zhu. An Estimate of Natural Gas Methane Emissions from California Homes. *Environmental Science & Technology*, August 2018. 50, 64

[77] Paul Balcombe, Kris Anderson, Jamie Speirs, Nigel Brandon, and Adam Hawkes. The Natural Gas Supply Chain: The Importance of Methane and Carbon Dioxide Emissions. *ACS Sustainable Chemistry & Engineering*, 5(1):3–20, January 2017. 50

[78] U.S. EIA. Form EIA-860, Annual Electric Generator Report. `https://www.eia.gov/electricity/annual/html/epa_08_02.html`. 51, 53, 54

[79] U.S. EPA. Air Markets Program Data. `https://ampd.epa.gov/ampd/`. 51, 52, 53, 54, 72

[80] Code of Federal Regulations Title 40 - Protection of Environment. https://www.gpo.gov/fdsys/pkg/CFR-2017-title40-vol23/xml/CFR-2017-title40-vol23-part98-subpartC.xml, July 2017. 52

[81] U.S. EPA. Facility Level Information on Greenhouse Gases Tool. http://ghgdata.epa.gov/ghgp/main.do. 52

[82] Volume 2 Energy. In S. Eggelston, B. Leandro, K. Miwa, T. Ngara, and K. Tanabe, editors, *2006 IPCC Guidelines for National Greenhouse Gas Inventories*, page 2.16. Institute for Global Environmental Strategies for the IPCC. 52

[83] Volume 2 Energy. In S. Eggelston, B. Leandro, K. Miwa, T. Ngara, and K. Tanabe, editors, *2006 IPCC Guidelines for National Greenhouse Gas Inventories*, page 2.25. Institute for Global Environmental Strategies for the IPCC. 52

[84] U.S. EPA. Inventory of U.S. Greenhouse Gas Emissions and Sinks: 1990-2016. https://www.epa.gov/ghgemissions/inventory-us-greenhouse-gas-emissions-and-sinks-1990-2016, January 2018. 52

[85] U.S. EPA. Chapter 3: Stationary Internal Combustion Sources. In *Compilation of Air Pollutant Emissions Factors*, volume 1 of *AP 42*, page 11. 5 edition. 52, 72

[86] Dana R. Caulton, Paul B. Shepson, Renee L. Santoro, Jed P. Sparks, Robert W. Howarth, Anthony R. Ingraffea, Maria O. L. Cambaliza, Colm Sweeney, Anna Karion, Kenneth J. Davis, Brian H. Stirm, Stephen A. Montzka, and Ben R. Miller. Toward a better understanding and quantification of methane emissions from shale gas development. *Proceedings of the National Academy of Sciences*, 111(17):6237–6242, April 2014. 52

[87] K. E. Garman, K. A. Hill, P. Wyss, M. Carlsen, J. R. Zimmerman, B. H. Stirm, T. Q. Carney, R. Santini, and P. B. Shepson. An Airborne and Wind Tunnel Evaluation of a Wind Turbulence Measurement System for Aircraft-Based Flux Measurements. *Journal of Atmospheric and Oceanic Technology*, 23(12):1696–1708, December 2006. 52

[88] E. R. Crosson. A cavity ring-down analyzer for measuring atmospheric levels of methane, carbon dioxide, and water vapor. *Applied Physics B*, 92(3):403–408, September 2008. 52

[89] U.S. EIA. Form EIA-860, Annual Electric Generator Report. https://www.eia.gov/electricity/annual/html/epa_04_03.html. 53

[90] Dana R. Caulton, Paul B. Shepson, Maria O. L. Cambaliza, David McCabe, Ellen Baum, and Brian H. Stirm. Methane Destruction Efficiency of Natural Gas Flares Associated with Shale Formation Wells. *Environmental Science & Technology*, 48(16):9548–9554, August 2014. 55

[91] Alexander Gvakharia, Eric A. Kort, Adam Brandt, Jeff Peischl, Thomas B. Ryerson, Joshua P. Schwarz, Mackenzie L. Smith, and Colm Sweeney. Methane, Black Carbon, and Ethane Emissions from Natural Gas Flares in the Bakken Shale, North Dakota. *Environmental Science & Technology*, 51(9):5317–5325, May 2017. 55

[92] A. Schneider. GPS Visualizer. http://www.gpsvisualizer.com/. 56

[93] Google Earth, March 2018. xii, 57

[94] Richard Wehr and Scott R. Saleska. The long-solved problem of the best-fit straight line: application to isotopic mixing lines. *Biogeosciences*, 14(1):17–29, January 2017. 56

[95] Igor Pro. WaveMetrics, Inc. 56

[96] O. E. Salmon, P. B. Shepson, X. Ren, H. He, D. L. Hall, R. R. Dickerson, B. H. Stirm, S. S. Brown, D. L. Fibiger, E. E. McDuffie, T. L. Campos, K. R. Gurney, and J. A. Thornton. Top-Down Estimates of NOx and CO Emissions From Washington, D.C.-Baltimore During the WINTER Campaign. *Journal of Geophysical Research: Atmospheres*, 123(14):7705–7724, 2018. 56, 79

[97] U.S. EIA. What are Ccf, Mcf, Btu, and therms? How do I convert natural gas prices in dollars per Ccf or Mcf to dollars per Btu or therm? https://www.eia.gov/tools/faqs/faq.php?id=45&t=8. 58

[98] U.S. EIA. Heat Content of Natural Gas Consumed by Electric Power Sector. https://www.eia.gov/dnav/ng/ng_cons_heat_a_EPG0_VEUH_btucf_a.htm. 58

[99] Wärstilä. Gas Turbine for Power Generation: Introduction. https://www.wartsila.com/energy/learning-center/technical-comparisons/gas-turbine-for-power-generation-introduction. 58, 67

[100] Weather Underground. Weather Forecast & Reports - Long Range & Local. https://www.wunderground.com/. 60

[101] IUPAC. Task Group on Atmospheric Chemical Kinetic Data Evaluation. http://iupac.pole-ether.fr/display_pressure_independent.php. 67

[102] U.S. EIA. Natural Gas Prices. https://www.eia.gov/dnav/ng/ng_pri_sum_dcu_nus_a.htm, April 2019. 72

[103] United Nations Department of Economic and Social Affairs Population Division. *World Urbanization Prospects: The 2018 Revision*. United Nations, New York, 2019. 75, 89

[104] International Energy Agency. *World Energy Outlook 2013.* OECD Publishing, Paris, 2013. 75, 89

[105] 100% Commitments in Cities, Counties, & States. https://www.sierraclub.org/ready-for-100/commitments, January 2016. 75, 89

[106] Kristian D. Hajny, Olivia E. Salmon, Joseph Rudek, David R. Lyon, Andrew A. Stuff, Brian H. Stirm, Robert Kaeser, Cody R. Floerchinger, Stephen Conley, Mackenzie L. Smith, and Paul B. Shepson. Observations of Methane Emissions from Natural Gas-Fired Power Plants. *Environmental Science & Technology*, 53(15):8976–8984, August 2019. 75, 76, 77, 79, 105

[107] Israel Lopez-Coto, Xinrong Ren, Olivia E. Salmon, Anna Karion, Paul B. Shepson, Russell R. Dickerson, Ariel Stein, Kuldeep Prasad, and James R. Whetstone. Wintertime CO2, CH4, and CO Emissions Estimation for the Washington, DC–Baltimore Metropolitan Area Using an Inverse Modeling Technique. *Environmental Science & Technology*, 54(5):2606–2614, March 2020. 75, 91, 105, 121, 122, 123

[108] Global Covenant of Mayors. `https://www.globalcovenantofmayors.org/`. 89

[109] C40. `https://www.c40.org/`. 89

[110] Todd Kaminsky. Climate Leadership Community Protection Act. `https://www.nysenate.gov/legislation/bills/2019/s6599`, June 2019. 89

[111] Cventure LLC, Cathy Pasion, Christianah Oyenuga, and Kate Gouin. City of New York Inventory of New York City's Greenhouse Gas Emissions. *Mayor's Office of Sustainbility, New York*, page 56, April 2017. 89

[112] Council to Vote on Climate Mobilization Act ahead of Earth Day. `https://council.nyc.gov/press/2019/04/18/1730/`, April 2019. 89

[113] S M Gourdji, V Yadav, A Karion, K L Mueller, S Conley, T Ryerson, T Nehrkorn, and E A Kort. Reducing errors in aircraft atmospheric inversion estimates of point-source emissions: The Aliso Canyon natural gas leak as a natural tracer experiment. *Environmental Research Letters*, 13(4):045003, April 2018. 90

[114] Jocelyn C. Turnbull, Anna Karion, Kenneth J. Davis, Thomas Lauvaux, Natasha L. Miles, Scott J. Richardson, Colm Sweeney, Kathryn McKain, Scott J. Lehman, Kevin R. Gurney, Risa Patarasuk, Jianming Liang, Paul B. Shepson, Alexie Heimburger, Rebecca Harvey, and James Whetstone. Synthesis of Urban CO_2 Emission Estimates from Multiple Methods from the Indianapolis Flux Project (INFLUX). *Environmental Science & Technology*, 53(1):287–295, January 2019. 90

[115] C. K. Gately and L. R. Hutyra. Large Uncertainties in Urban-Scale Carbon Emissions: Uncertainties in Urban Carbon Emissions. *Journal of Geophysical Research: Atmospheres*, 122(20):11,242–11,260, October 2017. 90

[116] Kevin R. Gurney, Daniel L. Mendoza, Yuyu Zhou, Marc L. Fischer, Chris C. Miller, Sarath Geethakumar, and Stephane de la Rue du Can. High Resolution Fossil Fuel Combustion CO_2 Emission Fluxes for the United States. *Environmental Science & Technology*, 43(14):5535–5541, July 2009. 90

[117] Kevin R. Gurney, Igor Razlivanov, Yang Song, Yuyu Zhou, Bedrich Benes, and Michel Abdul-Massih. Quantification of Fossil Fuel CO_2 Emissions on the Building/Street Scale for a Large U.S. City. *Environmental Science & Technology*, 46(21):12194–12202, November 2012. 90

[118] Kevin R. Gurney, J. Liang, D. O'Keeffe, R. Patarasuk, M. Hutchins, J. Huang, P. Rao, and Y. Song. Comparison of Global Downscaled Versus Bottom-Up Fossil Fuel CO_2 Emissions at the Urban Scale in Four U.S. Urban Areas. *Journal of Geophysical Research: Atmospheres*, 124(5):2823–2840, March 2019. 90, 120

[119] Tomohiro Oda, Shamil Maksyutov, and Robert J. Andres. The Open-source Data Inventory for Anthropogenic CO_2, version 2016 (ODIAC2016): A global monthly fossil fuel CO_2 gridded emissions data product for tracer transport simulations and surface flux inversions. *Earth System Science Data*, 10(1):87–107, January 2018. 90

[120] Greet Janssens-Maenhout, Monica Crippa, Diego Guizzardi, Marilena Muntean, Edwin Schaaf, Frank Dentener, Peter Bergamaschi, and Valerio Pagliari. EDGAR v4.3.2 Global Atlas of the three major Greenhouse Gas Emissions for the period 1970-2012. *Open Access*, page 55, 2017. 90

[121] Brian K. Lamb, Maria O. L. Cambaliza, Kenneth J. Davis, Steven L. Edburg, Thomas W. Ferrara, Cody Floerchinger, Alexie M. F. Heimburger, Scott Herndon, Thomas Lauvaux, Tegan Lavoie, David R. Lyon, Natasha Miles, Kuldeep R. Prasad, Scott Richardson, Joseph Robert Roscioli, Olivia E. Salmon, Paul B. Shepson, Brian H. Stirm, and James Whetstone. Direct and Indirect Measurements and Modeling of Methane Emissions in Indianapolis, Indiana. *Environmental Science & Technology*, 50(16):8910–8917, August 2016. 90

[122] Benjamin Fasoli, John C. Lin, David R. Bowling, Logan Mitchell, and Daniel Mendoza. Simulating atmospheric tracer concentrations for spatially distributed receptors: Updates to the Stochastic Time-Inverted Lagrangian Transport model's R interface (STILT-R version 2). *Geoscientific Model Development*, 11(7):2813–2824, July 2018. 90, 101, 104

[123] J. C. Lin, C. Gerbig, S. C. Wofsy, A. E. Andrews, B. C. Daube, K. J. Davis, and C. A. Grainger. A near-field tool for simulating the upstream influence of atmospheric observations: The Stochastic Time-Inverted Lagrangian Transport (STILT) model. *Journal of Geophysical Research: Atmospheres*, 108(D16), 2003. 90, 100, 104

[124] Maryann Sargent, Yanina Barrera, Thomas Nehrkorn, Lucy R. Hutyra, Conor K. Gately, Taylor Jones, Kathryn McKain, Colm Sweeney, Jennifer Hegarty, Brady Hardiman, Jonathan A. Wang, and Steven C. Wofsy. Anthropogenic and biogenic CO_2 fluxes in the Boston urban region. *Proceedings of the National Academy of Sciences*, 115(29):7491, July 2018. 90, 91, 114, 130

[125] Kathryn McKain, Adrian Down, Steve M. Raciti, John Budney, Lucy R. Hutyra, Cody Floerchinger, Scott C. Herndon, Thomas Nehrkorn, Mark S. Zahniser, Robert B. Jackson, Nathan Phillips, and Steven C. Wofsy. Methane emissions from natural gas infrastructure and use in the urban region of Boston, Massachusetts. *Proceedings of the National Academy of Sciences*, 112(7):1941, February 2015. 90, 91

[126] Anna Karion, Thomas Lauvaux, Israel Lopez Coto, Colm Sweeney, Kimberly Mueller, Sharon Gourdji, Wayne Angevine, Zachary Barkley, Aijun Deng, Arlyn Andrews, Ariel Stein, and James Whetstone. Intercomparison of atmospheric trace gas dispersion models: Barnett Shale case study. *Atmospheric Chemistry and Physics*, 19(4):2561–2576, February 2019. 90, 91, 122, 130

[127] Sebastian J. O'Shea, Grant Allen, Zoë L. Fleming, Stephane J.-B. Bauguitte, Carl J. Percival, Martin W. Gallagher, James Lee, Carole Helfter, and Eiko Nemitz. Area fluxes of carbon dioxide, methane, and carbon monoxide derived from airborne measurements around Greater London: A case study during summer 2012. *Journal of Geophysical Research: Atmospheres*, 119(8):4940–4952, 2014. 91

[128] J. Brioude, W. M. Angevine, R. Ahmadov, S.-W. Kim, S. Evan, S. A. McKeen, E.-Y. Hsie, G. J. Frost, J. A. Neuman, I. B. Pollack, J. Peischl, T. B. Ryerson, J. Holloway, S. S. Brown, J. B. Nowak, J. M. Roberts, S. C. Wofsy, G. W. Santoni, T. Oda, and M. Trainer. Top-down estimate of surface flux in the Los Angeles Basin using a mesoscale inverse modeling technique: Assessing anthropogenic emissions of CO, NO_x and CO_2 and their impacts. *Atmospheric Chemistry and Physics*, 13(7):3661–3677, April 2013. 91

[129] Yaoxian Huang, Eric A. Kort, Sharon Gourdji, Anna Karion, Kimberly Mueller, and John Ware. Seasonally Resolved Excess Urban Methane Emissions from the Baltimore/Washington, DC Metropolitan Region. *Environmental Science & Technology*, 53(19):11285–11293, October 2019. 91

[130] A. Stohl, P. Seibert, J. Arduini, S. Eckhardt, P. Fraser, B. R. Greally, C. Lunder, M. Maione, J. Mühle, S. O'Doherty, R. G. Prinn, S. Reimann, T. Saito, N. Schmidbauer, P. G. Simmonds, M. K. Vollmer, R. F. Weiss, and Y. Yokouchi. An analytical inversion method for determining regional and global emissions of greenhouse gases: Sensitivity studies and application to halocarbons. *Atmospheric Chemistry and Physics*, 9(5):1597–1620, March 2009. 91

[131] Anna M. Michalak, Lori Bruhwiler, and Pieter P. Tans. A geostatistical approach to surface flux estimation of atmospheric trace gases. *Journal of Geophysical Research: Atmospheres*, 109(D14), 2004. 91

[132] Kim L. Mueller, Sharon M. Gourdji, and Anna M. Michalak. Global monthly averaged CO2 fluxes recovered using a geostatistical inverse modeling approach: 1. Results using atmospheric measurements. *Journal of Geophysical Research: Atmospheres*, 113(D21), 2008. 91

[133] Lewis Kunik, Derek V. Mallia, Kevin R. Gurney, Daniel L. Mendoza, Tomohiro Oda, and John C. Lin. Bayesian inverse estimation of urban CO_2 emissions: Results from a synthetic data simulation over Salt Lake City, UT. *Elem Sci Anth*, 7(1):36, September 2019. 91

[134] Sha Feng, Thomas Lauvaux, Klaus Keller, Kenneth J. Davis, Peter Rayner, Tomohiro Oda, and Kevin R. Gurney. A Road Map for Improving the Treatment of Uncertainties in High-Resolution Regional Carbon Flux Inverse Estimates. *Geophysical Research Letters*, 46(22):13461–13469, November 2019. 91

[135] A. J. Turner, P. Köhler, T. S. Magney, C. Frankenberg, I. Fung, and R. C. Cohen. A double peak in the seasonality of California's photosynthesis as observed from space. *Biogeosciences*, 17(2):405–422, 2020. 92, 114

[136] SIF – Solar Induced Chlorophyll Fluorescence. `https://s5p-troposif.noveltis.fr/`. 92

[137] J.P. Veefkind, I. Aben, K. McMullan, H. Förster, J. de Vries, G. Otter, J. Claas, H.J. Eskes, J.F. de Haan, Q. Kleipool, M. van Weele, O. Hasekamp, R. Hoogeveen, J. Landgraf, R. Snel, P. Tol, P. Ingmann, R. Voors, B. Kruizinga, R. Vink, H. Visser, and P.F. Levelt. TROPOMI on the ESA Sentinel-5 Precursor: A GMES mission for global observations of the atmospheric composition for climate, air quality and ozone layer applications. *Remote Sensing of Environment*, 120:70–83, 2012. xiv, 93, 94

[138] Department of City Planning (DCP). Borough Boundaries (Water Areas Included). `https://data.cityofnewyork.us/City-Government/Borough-Boundaries-Water-Areas-Included-/tv64-9x69`. xiv, 95, 112

[139] Cory R. Martin, N. Zeng, A. Karion, K. Mueller, S. Ghosh, I. Lopez-Coto, K. R. Gurney, T. Oda, K. Prasad, Y. Liu, R. R. Dickerson, and J. Whetstone. Investigating sources of variability and error in simulations of carbon dioxide in an urban region. *Atmospheric Environment*, 199:55–69, February 2019. 96

[140] Copernicus Climate Change Service (C3S) (2017): ERA5: Fifth generation of ECMWF atmospheric reanalyses of the global climate. `https://cds.climate.copernicus.eu/cdsapp/#!/home`. vii, 100, 101

[141] READY - Gridded Data Archives. `https://ready.arl.noaa.gov/archives.php`. vii, 100, 101

[142] Conor Gately. In preparation. 102

[143] Kevin Robert Gurney, Yang Song, Jianming Liang, and Geoffrey Roest. Toward Accurate, Policy-Relevant Fossil Fuel CO $_2$ Emission Landscapes. *Environmental Science & Technology*, 54(16):9896–9907, August 2020. 102

[144] Oda Oda, Tomohiro and Shamil Maksyutov. ODIAC Fossil Fuel CO_2 Emissions Dataset ODIAC2019. *Center for Global Environmental Research, National Institute for Environmental Studies*. 102

[145] EDGAR v5.0 Global Greenhouse Gas Emissions. *European Commission*, October 2017. 102

[146] M Crippa, G Oreggioni, D Guizzardi, M Muntean, E Schaaf, E Lo Vullo, E Solazzo, F Monforti-Ferrario, J.G.J Olivier, E Vignati, European Commission, and Joint Research Centre. *Fossil CO2 and GHG Emissions of All World Countries: 2019 Report.* 2019. 102

[147] Ray Nassar, Louis Napier-Linton, Kevin R. Gurney, Robert J. Andres, Tomohiro Oda, Felix R. Vogel, and Feng Deng. Improving the temporal and spatial distribution of CO_2 emissions from global fossil fuel emission data sets: SCALING OF FOSSIL FUEL CO_2 EMISSIONS. *Journal of Geophysical Research: Atmospheres*, 118(2):917–933, January 2013. 103

[148] I. G Enting. *Inverse Problems in Atmospheric Constituent Transport*. Cambridge University Press, Cambridge; New York, 2002. 111

[149] Albert Tarantola. *Inverse Problem Theory and Methods for Model Parameter Estimation*. Other Titles in Applied Mathematics. Society for Industrial and Applied Mathematics, January 2005. 111

[150] A. C. Lorenc. Analysis methods for numerical weather prediction. *Quarterly Journal of the Royal Meteorological Society*, 112(474):1177–1194, 1986. 112

[151] Alexander J. Turner, Phillipp Kohler, Troy S. Magney, Christian Frankenberg, Inez Fung, and Ronald C. Cohen. Extreme Events Driving Year-to-Year Differences in Gross Primary Productivity Across the US [Manuscript submitted for publication]. *Geophysical Research Letters*, September 2020. 114

[152] John B. Miller, Scott J. Lehman, Kristal R. Verhulst, Charles E. Miller, Riley M. Duren, Vineet Yadav, Sally Newman, and Christopher D. Sloop. Large and seasonally varying biospheric CO2 fluxes in the Los Angeles megacity revealed by atmospheric radiocarbon. *Proceedings of the National Academy of Sciences*, 2020. 114, 130

[153] Data Search — National Centers for Environmental Information (NCEI). 114

[154] Noam Levin and Yishai Duke. High spatial resolution night-time light images for demographic and socio-economic studies. *Remote Sensing of Environment*, 119:1–10, April 2012. 120

[155] Jingwen Chen, Fang Zhao, Ning Zeng, and Tomohiro Oda. Comparing a global high-resolution downscaled fossil fuel CO2 emission dataset to local inventory-based estimates over 14 global cities. *Carbon Balance and Management*, 15(1):9, December 2020. 120

[156] Sourish Basu, Scott J. Lehman, John B. Miller, Arlyn E. Andrews, Colm Sweeney, Kevin R. Gurney, Xiaomei Xu, John Southon, and Pieter P. Tans. Estimating US fossil fuel CO $_2$ emissions from measurements of ^{14} C in atmospheric CO $_2$. *Proceedings of the National Academy of Sciences*, 117(24):13300–13307, June 2020. 123

[157] Xinxin Ye, Thomas Lauvaux, Eric A. Kort, Tomohiro Oda, Sha Feng, John C. Lin, Emily G. Yang, and Dien Wu. Constraining Fossil Fuel CO2 Emissions From Urban Area Using OCO-2 Observations of Total Column CO2. *Journal of Geophysical Research: Atmospheres*, 125(8):e2019JD030528, 2020. 126

[158] Jacob K. Hedelius, Junjie Liu, Tomohiro Oda, Shamil Maksyutov, Coleen M. Roehl, Laura T. Iraci, James R. Podolske, Patrick W. Hillyard, Jianming Liang, Kevin R. Gurney, Debra Wunch, and Paul O. Wennberg. Southern California megacity CO $_2$, CH $_4$, and CO flux estimates using ground- and space-based remote sensing and a Lagrangian model. *Atmospheric Chemistry and Physics*, 18(22):16271–16291, November 2018. 126

[159] Emily G. Yang, Eric A. Kort, Dien Wu, John C. Lin, Tomohiro Oda, Xinxin Ye, and Thomas Lauvaux. Using Space-Based Observations and Lagrangian Modeling to Evaluate Urban Carbon Dioxide Emissions in the Middle East. *Journal of Geophysical Research: Atmospheres*, 125(7):e2019JD031922, 2020. 126

[160] Yu Yan Cui, Abhilash Vijayan, Matthias Falk, Ying-Kuang Hsu, Dazhong Yin, Xue Meng Chen, Zhan Zhao, Jeremy Avise, Yanju Chen, Kristal Verhulst, Riley Duren, Vineet Yadav, Charles Miller, Ray Weiss, Ralph Keeling, Jooil Kim, Laura T. Iraci, Tomoaki Tanaka, Matthew S. Johnson, Eric A. Kort, Laura Bianco, Marc L. Fischer, Kenneth Stroud, Jorn Herner, and Bart Croes. A Multiplatform Inversion Estimation of Statewide and Regional Methane Emissions in California during 2014–2016. *Environmental Science & Technology*, 53(16):9636–9645, August 2019. 127

[161] D. J. Varon, J. McKeever, D. Jervis, J. D. Maasakkers, S. Pandey, S. Houweling, I. Aben, T. Scarpelli, and D. J. Jacob. Satellite discovery of anomalously large methane point sources from Oil/Gas production. *Geophysical Research Letters*, 46(22):13507–13516, 2019. 128

[162] D. J. Varon, D. J. Jacob, J. McKeever, D. Jervis, B. O. A. Durak, Y. Xia, and Y. Huang. Quantifying methane point sources from fine-scale satellite observations of atmospheric methane plumes. *Atmospheric Measurement Techniques*, 11(10):5673–5686, 2018. xvii, 128, 129, 133

[163] Daniel J. Varon, Daniel J. Jacob, Dylan Jervis, and Jason McKeever. Quantifying Time-Averaged Methane Emissions from Individual Coal Mine Vents with GHGSat-D Satellite Observations. *Environmental Science & Technology*, 54(16):10246–10253, August 2020. 128

[164] Eric A. Kort, Christian Frankenberg, Keeley R. Costigan, Rodica Lindenmaier, Manvendra K. Dubey, and Debra Wunch. Four corners: The largest US methane anomaly viewed from space. *Geophysical Research Letters*, 41(19):6898–6903, 2014. 129

[165] TEMPO Mission Overview. `http://tempo.si.edu/overview.html`. xvii, 129, 132

[166] F. Chevallier, M. Remaud, C. W. O'Dell, D. Baker, P. Peylin, and A. Cozic. Objective evaluation of surface- and satellite-driven carbon dioxide atmospheric inversions. *Atmospheric Chemistry and Physics*, 19(22):14233–14251, 2019. 129

[167] Daniel J Jacob. Using satellite observations to quantify methane sources and trends from the global scale down to point sources. `http://acmg.seas.harvard.edu/presentations/2020/ams_methane.pdf`. xvii, 131

[168] Fit with other missions. `https://www.methanesat.org/fit-with-other-missions/`. xvii, 131

[169] Jocelyn C. Turnbull, Colm Sweeney, Anna Karion, Timothy Newberger, Scott J. Lehman, Pieter P. Tans, Kenneth J. Davis, Thomas Lauvaux, Natasha L. Miles, Scott J. Richardson, Maria Obiminda Cambaliza, Paul B. Shepson, Kevin Gurney, Risa Patarasuk, and Igor Razlivanov. Toward quantification and source sector identification of fossil fuel CO2 emissions from an urban area: Results from the INFLUX experiment. *Journal of Geophysical Research: Atmospheres*, 120(1):292–312, 2015. 130

[170] Genevieve Plant, Eric A. Kort, Cody Floerchinger, Alexander Gvakharia, Isaac Vimont, and Colm Sweeney. Large Fugitive Methane Emissions From Urban Centers Along the U.S. East Coast. *Geophysical Research Letters*, 46(14):8500–8507, July 2019. 130

[171] Cody Floerchinger, Paul Shepson, Kristian Hajny, Bruce Daube, Brian Stirm, Colm Sweeney, and Steven Wofsy. Measurement of the Fraction of Methane Emissions Derived from Natural Gas for Seven U. S. Cities. *Submitted to Elementa: Science of the Anthropocene*. 130

[172] Makoto Kelp, Timothy Gould, Elena Austin, Julian D. Marshall, Michael Yost, Christopher Simpson, and Timothy Larson. Sensitivity analysis of area-wide, mobile source emission factors to high-emitter vehicles in Los Angeles. *Atmospheric Environment*, 223:117212, 2020. 130

VITA

Kristian Daniel Hajny was born on June 5, 1993 to Connie and John Hajny. He grew up in Nassau County on Long Island, NY until middle school, at which point his immediate family moved to NC with his immediate family, a younger sister (Megan) and two younger brothers (Kevin and Connor). In High School he was encouraged to pursue his scientific interests by Mrs. Davidson and Ms. Sullivan. He did a senior project (entirely open-ended topic) working with scientists at the David H. Murdock research center and researching nanotechnology thanks to these teachers' input and connections. He went to Furman University with the aim of a degree in Chemistry but joined a first-year program focused on environmental science and was quickly convinced to double major, regardless of the advanced planning required to meet the diverse course requirements. While at Furman he did research every summer and worked not only with a different professor, but in a different department each time. Freshman summer he worked on an organic synthesis and learned methods and techniques from a masters student, Sophomore summer involved a month in Guatemala followed by processing survey results to understand the relationships between health, economics, and sanitation in a growing rural area, and his Junior summer was spent analyzing spring waters in rural South Carolina to understand any relationship between fault lines and chemical tracers. He jumped projects often as he knew he wanted to work on a project that combined his chemical and environmental interests. After graduating he didn't know the school he'd go to, but was encouraged by one of his environmental science professors to talk with a Purdue professor, Dr. Jon Harbor. Once accepted to Purdue he reviewed many potential projects that would incorporate both of his interests, and shortly after arriving visited Dr. Shepson. Under the

direction of Dr. Shepson he learned coding to work with large datasets, finding an unexpected interest in it, and quantified emissions of greenhouse gases downwind of both cities and power plants with a focus on method assessment and development. A colleague, now Dr., Cody Floerchinger from Harvard joined the lab briefly for a cooperative experiment and several years later at a conference invited Kris to visit Harvard, learn from Dr. Steve Wofsy, and work on a modeling project in a lab with experienced colleagues around for support. Surprisingly, a year-long stay at Harvard was as simple as this with Dr. Shepson and Dr. Floerchinger acting as joint PIs on a final modeling project. Kris enjoyed entering the modeling world, learning to play with method development, and as such looks forward to a postdoc with Dr. Shepson working with NIST on similar, more advanced modeling efforts.

PUBLICATIONS

Environmental Science & Technology

Article

Cite This: Environ. Sci. Technol. 2019, 53, 8976−8984

pubs.acs.org/est

Observations of Methane Emissions from Natural Gas-Fired Power Plants

Kristian D. Hajny,[†] Olivia E. Salmon,[†,¶] Joseph Rudek,[‡] David R. Lyon,[‡] Andrew A. Stuff,[†] Brian H. Stirm,[§] Robert Kaeser,[†] Cody R. Floerchinger,[∥] Stephen Conley,[⊥] Mackenzie L. Smith,[⊥] and Paul B. Shepson*[,†,#]

[†]Purdue University, Department of Chemistry, West Lafayette, Indiana 47907, United States

[‡]Environmental Defense Fund, Austin, Texas 78701, United States

[§]Purdue University, School of Aviation and Transportation Technology, West Lafayette, Indiana 47906, United States

[∥]Harvard University, Department of Earth and Planetary Sciences, Cambridge, Massachusetts 02138, United States

[⊥]Scientific Aviation, Inc., Boulder, Colorado 80301, United States

[#]Stony Brook University, School of Marine and Atmospheric Sciences, Stony Brook, New York 11794, United States

Supporting Information

ABSTRACT: Current research efforts on the atmospheric impacts of natural gas (NG) have focused heavily on the production, storage/transmission, and processing sectors, with less attention paid to the distribution and end use sectors. This work discusses 23 flights at 14 natural gas-fired power plants (NGPPs) using an aircraft-based mass balance technique and methane/carbon dioxide enhancement ratios ($\Delta CH_4/\Delta CO_2$) measured from stack plumes to quantify the unburned fuel. By comparing the $\Delta CH_4/\Delta CO_2$ ratio measured in stack plumes to that measured downwind, we determined that, within uncertainty of the measurement, all observed CH_4 emissions were stack-based, that is, uncombusted NG from the stack rather than fugitive sources. Measured CH_4 emission rates (ER) ranged from 8 (±5) to 135 (±27) kg CH_4/h (±1σ), with the fractional CH_4 throughput lost (loss rate) ranging from −0.039% (±0.076%) to 0.204% (±0.054%). We attribute negative values to partial combustion of ambient CH_4 in the power plant. The average calculated emission factor (EF) of 5.4 (+10/−5.4) g CH_4/million British thermal units (MMBTU) is within uncertainty of the Environmental Protection Agency (EPA) EFs. However, one facility measured during startup exhibited substantially larger stack emissions with an EF of 440 (+660/−440) g CH_4/MMBTU and a loss rate of 2.5% (+3.8/−2.5%).

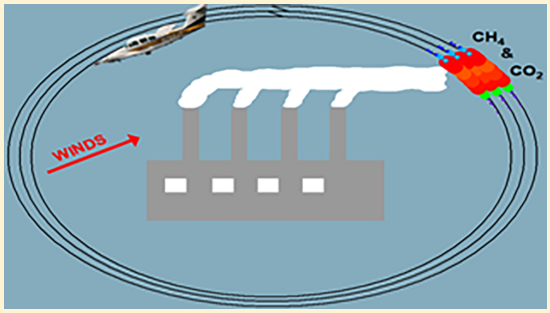

INTRODUCTION

Natural gas (NG) usage has been growing since the large-scale implementation of hydraulic fracturing and horizontal drilling technologies to take advantage of shale resources.[1,2] Along with market factors and stricter environmental regulations, this has led to a near doubling of the U.S. electricity generation from NG since 2008, with electricity generation matching or surpassing that of coal since 2016.[3] NG offers improved efficiency and availability and only produces 56% the amount of carbon dioxide (CO_2) per unit energy as coal, making it a potential "bridge fuel" in the transition toward renewable energy.[4] However, NG is primarily composed of methane (CH_4), the second most important anthropogenic greenhouse gas (GHG) accounting for 9% of all U.S. GHG emissions in 2017[5] based on its 100-year Global Warming Potential (GWP) (calculations are detailed in the SI). CH_4 is also a short-lived gas with a GWP of 84 over a 20-year period compared to a GWP of 28 over a 100-year period.[6] When using the 20-year GWP, CH_4 emissions are equivalent to 22% of annual U.S. GHG emissions (calculation detailed in SI). The short-term impact of reducing CH_4 emissions makes it an important focus of climate change mitigation efforts.

Over 50% of global CH_4 emissions are related to human activity, and losses from the energy sector are the largest anthropogenic source in the U.S.[7] On the basis of a recent synthesis of CH_4 emissions from well to end user, Alvarez et al.[8] estimated that 2.3% of U.S. gross production of NG is emitted to the atmosphere. At this loss rate, supply chain CH_4 emissions nearly double the short-term climate impact of the combustion of NG for energy. Therefore, quantifying losses along the NG supply chain from production to end use is essential. To realize

Received: March 28, 2019
Revised: June 14, 2019
Accepted: June 24, 2019
Published: June 24, 2019

Table 1. Key Parameters Describing the NGPPs Studied[a]

ID	state	firing method	max capacity (MW)	operation type	commercial operating date
P1	UT	combined cycle	560	intermediate	2005
P2	UT	combined cycle	1180	intermediate	2007, 2014
P3	IL	combined cycle	1310	baseload	2002
P4	IL	combined cycle	680	peaking	2002
P5	IN	combined cycle	730	baseload	2002
P6	FL	combined cycle	3530	baseload	2009, 2011
P7	FL	simple thermal	1070	baseload	2013
P8	FL	combined cycle	1190	baseload	2014
P9	FL	combustion turbine	790	intermediate	2002
P10	FL	50% combined cycle, 50% combustion turbine	2100	intermediate	2003, 2009
P11	OH	combined cycle	760	baseload	2012
P12	OH	combined cycle	590	baseload	2012
P13	OH	combined cycle	940	baseload	2003
P14	MI	50% combined cycle, 50% combustion turbine	1000	baseload	2001, 2002

[a]Operation types are based on the most active units (e.g., a plant with 1 baseload and 3 intermediate units is labeled baseload). Maximum capacities are calculated from the maximum hourly heat input from AMPD,[23] and the heat rate from the U.S. Energy Information Administration.[22] Commercial operating dates are from AMPD data and news articles for the plants. Multiple years are listed when additional units were added, and conversion dates are used if plants were converted to gas.

the climate benefit of NG, it must be efficiently handled and combusted.

There have been multiple studies focused on the production, storage, and processing of NG, but there has been little work on end users, such as natural gas-fired power plants (NGPP).[8−21] Lavoie et al.[17] studied three NGPPs and saw emissions of unburned CH_4 from the stacks and relatively large CH_4 leaks attributed to nonstack sources on-site. The Lavoie et al. study was based on a small sample size of 3 combined cycle power plants (CC), which use the combustion gases to turn a turbine. Excess heat is then used to generate steam to turn a second turbine. CC plants are the most efficient NGPPs, producing 46% more energy per energy content of fuel consumed than a simple combustion turbine.[22] Because of this higher efficiency, CC facilities are the most common type of NGPP, providing 89% of the electricity produced by NG.[23] As such, we focus largely on CC NGPP emissions in this study.

We expand on the work of Lavoie et al. by sampling a larger set of NGPPs to thoroughly investigate the prevalence of on-site CH_4 leaks and to gather more robust emissions data to compare to the Environmental Protection Agency (EPA) estimates. We studied 14 NGPPs, but only 5 showed downwind ΔCH_4, while all showed ΔCO_2 downwind. This suggests CH_4 emissions were too low to be detected above atmospheric variability at most NGPPs. This work focuses on the 5 NGPPs that showed downwind ΔCH_4. We calculate $\Delta CH_4/\Delta CO_2$ (ppm/ppm) ratios when flying through the stack emission plumes with/against the mean wind direction or circling near the stacks. We quantify the facility (nonstack) CH_4 leaks by comparing this to the same ratio from downwind aircraft-based mass balance experiments (MBE), which would capture all plant emissions.

Although the EPA calculates CH_4 emissions from NGPPs, it does so using emission factors (EF) that have not been well-tested and may underestimate emissions based on previous work in the NG sector.[2,9,10,17] The EPA requires that facilities report hourly averaged CO_2 emissions through the Air Markets Program Data (AMPD) using Continuous Emissions Monitoring Systems (CEMS) as described in Title 42 of the U.S. Code of Federal Regulations.[23,24] As for CH_4, the Greenhouse Gas Reporting Program (GHGRP), a reporting program for GHG point sources, uses an EF of 1 g CH_4 per million British thermal units (MMBTU) for all NGPPs based on the Intergovernmental Panel on Climate Change (IPCC) recommendations.[24−26] The Greenhouse Gas Inventory (GHGI), a comprehensive bottom-up inventory used to estimate national emissions by source category, instead uses an EF of 3.9 g CH_4/MMBTU for CC and combustion turbine NGPPs based on both the IPCC and the EPA's Compilation of Air Pollutant Emission Factors (AP-42).[27−29] In this work, we present statistically meaningful results from 5 NGPPs and discuss the magnitude and variability of stack emissions. A companion paper is being prepared to investigate the measured CO_2 emission rates (ERs) as compared to AMPD reported CO_2 ERs.[30]

MATERIALS AND METHODS

Instrumentation. Flights were conducted using Purdue's Airborne Laboratory for Atmospheric Research (ALAR),[11,31−34] which is a modified twin-engine Beechcraft Duchess aircraft. ALAR is outfitted with a global positioning and inertial navigation system, a Best Air Turbulence probe for high precision 3-dimensional wind measurements,[35] and a model G2301-m Picarro Cavity Ring Down Spectrometer designed for 0.5 Hz airborne measurements of CO_2, CH_4, and H_2O.[36] We conducted multiple three-point calibrations each flight using NOAA-certified standard cylinders containing CO_2 and CH_4, with concentrations that bracket the range of typical observations. A direct absorption ethane (C_2H_6) spectrometer designed by Aerodyne Research and modified at Harvard University was added to ALAR for a subset of flights (see SI for instrument details).

Flight Design and Site Selection. We conducted a total of 23 flights at 14 NGPPs to quantify NGPP CH_4 emissions. Combined, these plants represent 3.4% and 1.5% of NG and total U.S. nameplate capacity, respectively.[37] A principal goal of this study was to produce a representative data set; thus, NGPPs were chosen to include a variety of regions, firing methods, maximum capacities, ages, and operation types, as shown in Table 1.[17] These NGPPs are relatively new, but this is to be expected as ∼70% of NGPP capacity comes from units ≤20 years old.[37] Operation type refers to a unit's typical generation and is defined here as baseload units operating >70% of the year,

DOI: 10.1021/acs.est.9b01875
Environ. Sci. Technol. 2019, 53, 8976−8984

Table 2. Conditions and Date of Each Mass Balance Flight[a]

ID	date (MM/DD/YY)	time (local)	wind direction (deg)	wind speed (m/s)	flight method
P6	11/12/16	13:50−15:40	145 ± 70	2 ± 1	DT[d]
P6	11/13/16	14:35−15:33	130 ± 10	4.1 ± 0.9	DT
P6	11/19/16	13:14−15:14	335 ± 30	4 ± 2	DT
P8	11/14/16	14:05−14:50	250 ± 10	3.2 ± 0.7	DT
P8	11/17/16	13:12−14:19	38 ± 8	8 ± 2	DT
P4	6/14/17	12:40−13:11	220 ± 13	7 ± 1	spiral[d]
P4	6/21/17	14:50−15:40	250 ± 20	4 ± 1	spiral
P4	7/24/17	16:05−17:26	50 ± 10	4.2 ± 0.9	DT
P3	5/18/17	13:46−15:44	260 ± 10	13 ± 3	DT
P3	7/7/17	14:40−15:16	340 ± 10	11 ± 1	DT
P3	7/24/17	12:01−13:38	30 ± 20	5.5 ± 2	DT[e]
P2	10/12/17[c]	13:26−13:53	290 ± 50	2 ± 1	DT[f]
P2	10/13/17[c]	12:23−12:51	NA[b]	3[b]	spiral

[a]Uncertainties are 1σ. DT = downwind transects. [b]Complex wind conditions, see SI for details. [c]AMPD data shows the facility to be in startup, having begun producing within the past 4 h. [d]CH_4 emissions were too low to be quantified. [e]Emissions cannot be quantified because of contamination from an upwind source. [f]Emissions could not be quantified due to incomplete plume capture downwind.

intermediate units operating 30−70%, and peaking units operating <30% of the year based on AMPD data.[23]

We performed MBEs during each flight to quantify ERs and stack measurements of $\Delta CH_4/\Delta CO_2$ ratios. Flights also included either a circle around the NGPP or an upwind horizontal transect to determine if other sources could influence downwind measurements. MBEs were conducted by flying multiple horizontal transects, typically in 250 ft intervals, at a fixed distance (~3 km) downwind of the site from as low to the ground as is safe to the highest altitude where emissions could be seen, often with a vertical spiral through the downwind plume (see Figure S3). The transects extend sufficiently beyond the edges of the plume so that GHG concentrations return to background concentrations. A standard linear regression is fit through this background concentration to estimate the transect's background.[38] MBE ERs of CH_4 are then calculated according to eq 1.

$$\text{MBE ER} = \int_0^{Z_i} \int_{-x}^{x} ([C] - [C]_b) \times U_\perp \, dx \, dz \tag{1}$$

In eq 1, the CH_4 enhancement ($[C] - [C]_b$) is calculated as the difference between the instantaneous measurement and the background. This enhancement (mol/m^3) is multiplied by the 10 s rolling-averaged perpendicular component of the wind speed, $U_\perp$ (m/s). These pointwise fluxes (mol/m^{2}s) are then interpolated to a two-dimensional gridded surface by kriging[39] and integrated horizontally across the length of the plume ($-x$ to x) and vertically from the surface to the top of the boundary layer (0 to Z_i) to provide ERs (mol/s) that are converted to kilograms per hour for consistency with AMPD values (uncertainty calculation is detailed in the SI). Low wind conditions increase the ER uncertainty as transects are less likely to capture all emissions with meandering winds, so several flights use the stacked closed-path method discussed by Conley et al.[40] to obtain an ER, as it is more likely to capture all emissions in such conditions. The uncertainty estimates for this method are described in detail by Conley et al.[40] and include uncertainties associated with wind speed and direction, precision of the chemical species monitor, and the circle-to-circle variability in calculated horizontal fluxes, caused by stochastic turbulence.

Calculation of EFs and Stack ERs. To quantify the impact of nonstack emissions, stack $\Delta CH_4/\Delta CO_2$ ratios are multiplied by the measured CO_2 ER to calculate a theoretical CH_4 ER (stack ER) according to eq 2. Stack ratios were calculated in a similar manner to previous studies[17,41,42] with details provided in the SI. Any MBE ERs that are substantially greater than the stack ER would indicate potential facility-scale CH_4 leaks.

$$\text{average stack ratio} \times \text{MBE } CO_2 \text{ ER} \times \text{mol wt. ratio}\left(\frac{16}{44}\right) = \text{stack } CH_4 \text{ ER} \tag{2}$$

A recent life cycle analysis of the NG supply chain estimated the current supply chain loss rate at 2.3% of U.S. gross production, ~60% larger than EPA estimates.[8] However, the study authors were unable to update local distribution and end user emissions due to insufficient information. To help address this lack of information, we have also calculated loss rates for our end user data using eqs 3 and 4. Equation 3 shows the calculation of the CH_4 throughput using the AMPD reported heat input, the density of NG, the heat content of NG,[43,44] and the assumption that NG is 95% CH_4. Equation 4 shows the calculation of loss rates, and eq 5 shows the calculation of the throughput-based EF. Both calculations rely on a theoretical CH_4 ER (AMPD stack ER) calculated according to eq 2 using the AMPD CO_2 ER instead of the MBE CO_2 ER to avoid incorporating any potential biases of the MBE ERs.

$$\text{throughput}\left(\text{kg}\,\frac{CH_4}{\text{h}}\right) = \text{heat input}\left(\frac{\text{MMBTU}}{\text{h}}\right) \times \frac{1\ \text{MCF}}{1.033\ \text{MMBTU}} \times \frac{18.9\ \text{kg}\ CH_4}{1\ \text{MCF}} \times 0.95 \tag{3}$$

$$\text{loss rate (\%)} = \frac{\text{AMPD stack ER}\left(\text{kg}\frac{CH_4}{\text{h}}\right)}{\text{throughput}\left(\text{kg}\frac{CH_4}{\text{h}}\right)} \times 100 \tag{4}$$

$$\text{EF}\left(\frac{\text{g}}{\text{MMBTU}}\right) = \frac{\text{AMPD stack ER}\left(\text{g}\frac{CH_4}{\text{h}}\right)}{\text{heat input}\left(\frac{\text{MMBTU}}{\text{h}}\right)} \tag{5}$$

DOI: 10.1021/acs.est.9b01875
Environ. Sci. Technol. 2019, 53, 8976−8984

Table 3. MBE ERs, Stack Ratios, and Stack ERs[a]

ID	date	average stack ratio (CH_4/CO_2, mol/mol)	CH_4 MBE ER (kg/h) (eq 1)	CH_4 stack ER (kg/h) (eq 2)
P6	11/12/16	$-3\ (\pm7) \times 10^{-4}$	NA[b]	-70 ± 150
			NA[b]	-60 ± 120
P6	11/13/16	$2\ (\pm1) \times 10^{-4}$	74 ± 15	53 ± 36
			71 ± 18	46 ± 32
P6	11/19/16	$1\ (\pm3) \times 10^{-4}$	89 ± 20	30 ± 96
			135 ± 27	40 ± 140
P8	11/14/16	$2\ (\pm1) \times 10^{-4}$	56 ± 22	21 ± 16
P8	11/17/16	$3\ (\pm3) \times 10^{-4}$	8 ± 5	21 ± 13
			13 ± 5	16 ± 14
P4	6/14/17	$-0.7\ (\pm6) \times 10^{-5}$	NA[b]	-0.5 ± 4
P4	6/21/17	NA	80 ± 30	NA
P4	7/24/17	$1.8\ (\pm0.4) \times 10^{-3}$	113 ± 22	99 ± 29
			42 ± 12	91 ± 28
P3	5/18/17	$3\ (\pm2) \times 10^{-4}$	NA[b]	22 ± 17
			15.6 ± 8.6	24 ± 18
P3	7/7/17	$3\ (\pm3) \times 10^{-4}$	36.6 ± 7.5	70 ± 78
P2	10/13/17	$2\ (+3/-2) \times 10^{-2}$	22 ± 47	$350 + 660/-350$

[a]All uncertainties are 1σ. Uncertainty lower limits are set to 0 for P2 as stack data were highly variable but consistently positive. [b]CH_4 emissions were too low to quantify.

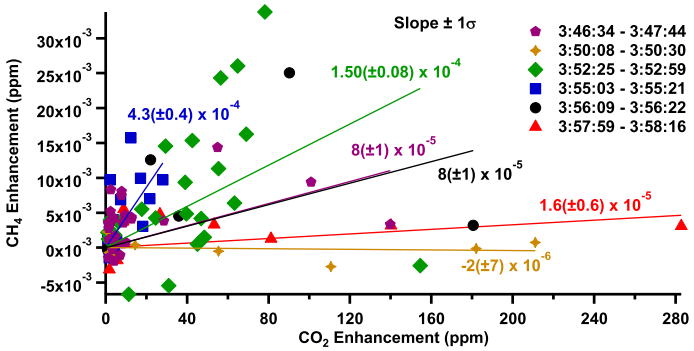

Figure 1. Stack samples from P3 measured from 3:46 to 3:59 local time on 5/18/2017. Each stack sample was measured by flying directly over the stacks with/against the mean winds. As such, some plumes were followed further downwind, up to a maximum distance of 5 km. The large variability in the slope, equivalent to the $\Delta CH_4/\Delta CO_2$ stack ratio, over short time scales can be seen. This leads to large uncertainties in the flight averaged stack ratios in many cases. That should not be confused with uncertainty in the individual slopes.

RESULTS AND DISCUSSION

Analysis of Stack Emissions. Although all flights showed ΔCO_2, only 5 of the 14 NGPPs examined showed ΔCH_4 above atmospheric variability in the downwind transects, consisting of 10 flights and 15 MBEs. Each flight's meteorological conditions are described in Table 2. P6 was successfully sampled on 11/12/2016, 11/13/2016, and 11/19/2016. P3, previously sampled by Lavoie et al.,[17] was sampled on three separate occasions, but the third (7/24/17) showed evidence of an intermittent source upwind of the plant and has thus not been used for MBE ER quantification. P2, also sampled by Lavoie et al.,[17] was sampled on 10/12/2017 and 10/13/2017, but the 10/12 flight has been considered unusable as incomplete plume capture would make uncertainties in the MBE ERs large. P8 was sampled on 11/14/2016 and 11/17/2016, and P4 was sampled on 6/14/2017, 6/21/2017, and 7/24/2017, although we were unable to measure stack plumes on 6/21/2017. However, the flight at P6 on 11/12/2016, one of the MBEs at P3 on 5/18/2017, and the flight at P4 on 6/14/2017 all showed no downwind ΔCH_4.

We used eq 2 to compare stack ERs to downwind MBE ERs and found no statistically significant difference. MBE ERs calculated according to eq 1, stack ratios, and stack ERs calculated according to eq 2 are provided in Table 3. In all cases, there is agreement within uncertainty between stack ERs and MBE ERs, although many flights exhibit large variability in stack

DOI: 10.1021/acs.est.9b01875
Environ. Sci. Technol. 2019, 53, 8976−8984

ratios leading to large uncertainties in stack ERs. This suggests that all CH_4 emissions measured were uncombusted fuel CH_4.

Our flights have shown highly variable $\Delta CH_4/\Delta CO_2$ stack ratios for individual power plants even over the short time scale from one pass over the stack to the next. The flight at P3 on 5/18/2017 included significant stack measurements to investigate the extent to which CH_4 emissions were from the stack as compared to equipment on-site, and to more thoroughly investigate the high variability in $\Delta CH_4/\Delta CO_2$ stack ratios. Figure 1 highlights the temporal variability in unburned CH_4 observed in the stack emissions for P3, covering just one 13 min window. In that 13 min period, the slopes spanned a range of ~25, not including the one case with a negative slope (discussed below). The data plotted in Figure 1 represents $\Delta CH_4/\Delta CO_2$ for short-term simultaneous spikes in CH_4 and CO_2, which are background-subtracted using a linear regression through the data immediately pre- and post-plume as shown in Figure S5. Thus, we believe the observed variability is not influenced by variability in background values. Each stack plume measured is regressed in a similar manner as in Figure 1, and the slope represents the $\Delta CH_4/\Delta CO_2$ ratio for that individual plume, hereafter referred to as a stack sample. Figure 2 shows a

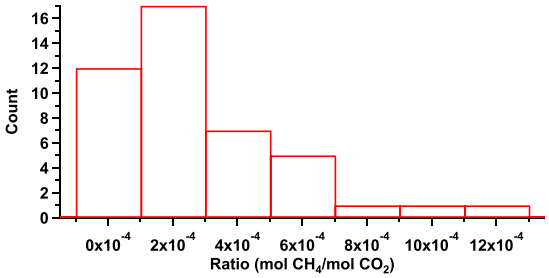

Figure 2. Histogram of all stack samples from P3 across all 3 flight days, excluding data with evidence of an upwind source on 7/24/17. $N = 44$, mean = 2.9×10^{-4}, and median = 2.4×10^{-4}.

histogram of stack samples for P3 across three different flight days. For comparison, a histogram of all stack samples across all CC facilities is shown in Figure 3. The median corresponds to an unburned CH_4 fraction of 0.01% in Figure 3 compared to 0.024% in Figure 2. These highlight the high combustion

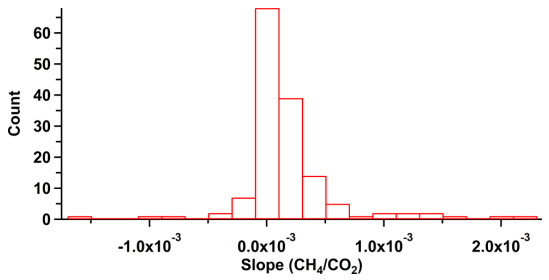

Figure 3. Histogram of all CC stack samples from all flights excluding P2 (discussed separately in Figure 6), including those without CH_4 enhancements and those with CH_4 depletions. $N = 149$, mean = 2×10^{-4}, and median = 1×10^{-4}. The majority of samples show a near 0 $\Delta CH_4/\Delta CO_2$ stack ratio highlighting the high combustion efficiency of these plants.

efficiency of these plants, high enough that in some cases there is less CH_4 in the exhaust than in the intake air.

Unexpectedly, at a small number of facilities, we measured CH_4 depletions during stack sampling. Figure 4 shows an

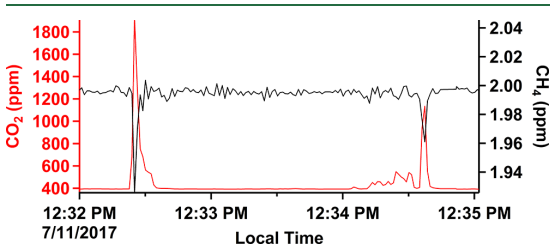

Figure 4. Example negative ΔCH_4 stack measurements from the 7/11/2017 flight at P12. We suggest that this represents partial consumption of intake air's background CH_4.

extreme case that we observed, and Figure 5 shows the regressions for multiple stack samples with statistically significant negative slopes. Because such signals are then diluted and dispersed downwind, we have not observed any statistically significant depletions of CH_4 during downwind MBEs. We hypothesize that the most likely cause for this phenomenon is a highly efficient combustion process that consumes all fuel CH_4 and a small fraction of ambient CH_4 from the combustion turbine's intake air. A similar hypothesis was provided by Fischer et al.[20] when similar depletions were observed while studying household appliances. Although we collected C_2H_6 data for a small number of stack samples that showed CH_4 depletions, none show a clear ΔC_2H_6. One of the largest CH_4 depletions was 3.7% depleted relative to background. This would correspond to a 0.037 ppb theoretical C_2H_6 depletion from the 1 ppb background, assuming equal percent background depletion. This is within atmospheric variability and just above instrumental precision. The Picarro measures H_2O concentrations and reports real-time dry CO_2 and CH_4 concentrations which have been used in all analyses. All stack CH_4 data was also corrected for the dilution impacts of CO_2 given the large CO_2 concentrations measured, but this is a minor impact at only 0.1 ppb for a 1500 ppm ΔCO_2 and 70 ppb ΔCH_4.

One NGPP (P2) exhibited large CH_4 emissions on two separate flights, both of which included C_2H_6 measurements. On 10/12/2017, there were no stack measurements, and the vertical extent of the plume was not well captured; therefore, the flight could not be confidently used to calculate an MBE ER. However, the flight shows clear downwind ΔCH_4 and ΔC_2H_6 of up to 470 and 15 ppb, respectively, with ΔCO_2 of $\leq$2 ppm, which is much smaller than typically seen. The flight on 10/13/2017 showed stack $\Delta CH_4/\Delta CO_2$ ratios that were up to 3 orders of magnitude (to 13% indicated CH_4) larger than those observed at all other NGPPs, with concurrent emissions of CH_4, CO_2, and C_2H_6 throughout the flight, as shown in Figure 6A. Some stack samples even showed CH_4 and C_2H_6 concentrations above the dynamic range of the ethane analyzer but with CO_2 signals comparable to those observed at other facilities (Figure S1). AMPD data for both P2 flights show that the facility was within 4 h of starting up, suggesting these may be emissions associated with the startup condition. To ensure that all measured CH_4 was from NG in this city environment we compared the $\Delta C_2H_6/\Delta CH_4$ ratio to pipeline reports (Figure S2). Both flights show a ratio ~25% lower than pipeline data but also show a highly linear

DOI: 10.1021/acs.est.9b01875
Environ. Sci. Technol. 2019, 53, 8976−8984

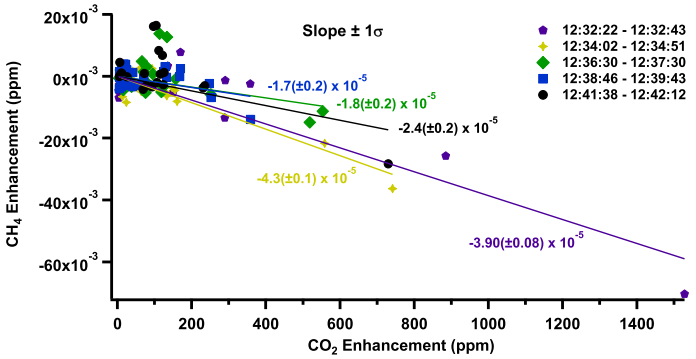

Figure 5. Stack samples on 7/11/2017 for P12 that show consistent anticorrelated ΔCH_4. This shows that the anticorrelation is consistent throughout the dips.

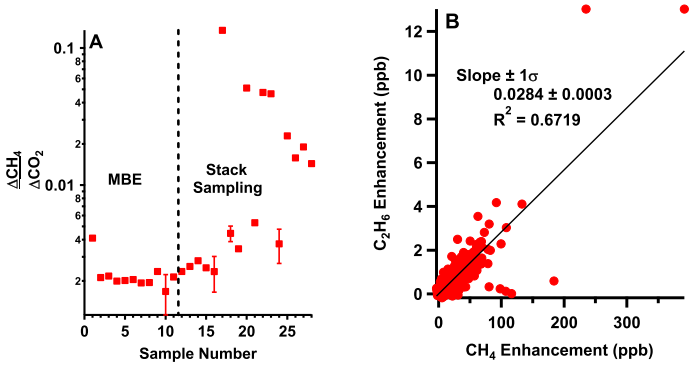

Figure 6. (A) Log scale showing the ratio of $\Delta CH_4/\Delta CO_2$ in each plume (both stack and MBE) from P2 on 10/13/2017. Samples 1−11 are from the MBE. These ratios are at least an order of magnitude larger than those seen at other facilities, although they are also much more variable. (B) Regression of ΔC_2H_6 versus ΔCH_4 for all plumes with usable C_2H_6 data for 10/13/2017. The linearity of the data suggests a single thermogenic source of CH_4.

ΔC_2H_6 versus ΔCH_4 relationship as shown in Figures 6B and S2, which suggests all emissions are from a thermogenic source. This discrepancy in $\Delta C_2H_6/\Delta CH_4$ may be caused by a combustion skew as the rate constant for CH_4 oxidation by OH radicals is ∼20% as large as that for the C_2H_6−OH reaction at 1600 °C.[45,46]

Natural Gas Power Plants as CH_4 Emitters. We used eqs 3−5 to convert the stack $\Delta CH_4/\Delta CO_2$ ratio into useful metrics in understanding NG leaks. The AMPD stack ERs, throughputs, loss rates, EFs, and reported AMPD CO_2 ERs are presented in Table 4. The EFs are directly compared to the EPA EFs of 1 g/MMBTU (GHGRP) and 3.9 g/MMBTU (GHGI) in Figure 7.

Although the average EF is consistent with EPA EFs, two plants show noticeably higher EFs (Table 4). P4, the only peaking facility studied, shows a slightly negative stack ratio for one flight and high stack ratios relative to the EPA EFs for the other two. The only other noteworthy aspect of P4 is the slightly lower load relative to the maximum capacity which was ∼60% across all flights as compared to 70−80% at all other CH_4 emitting facilities, excluding P2. AMPD reported CO_2 ERs were similar across the three flights with 170 Mg/h on 6/14 and 180 Mg/h both other flight days. Including CC plants that did not show downwind ΔCH_4, but excluding P4 and P2, the average loss rate is 0.014 (+0.021/−0.014)% (see Table S1) which is consistent with Lavoie et al.[17] who reported stack loss rates of 0.05 (±0.06)%. The average stack EF calculated using all CC stack data other than P2 is 5.4 (+10/-5.4) g/MMBTU (see Table S1). Because of the significant variability in stack samples (Figures 1 and 6) and to some degree cases with depleted CH_4 (Figures 4 and 5), propagated uncertainties are large, but we are representing them with a 0 lower limit given our data does not indicate negative emissions at the scales a symmetric uncertainty would suggest.

P2 is the only facility measured during startup and it showed a substantially higher EF than other facilities, as shown in Figure 6A. As P2 is the only facility that was sampled during startup, we do not know if our observations are broadly representative of startup emissions. EPA's AP-42[29] explains that EFs are based on efficient combustion under high operating conditions (≥80% of max capacity) and that emissions during lower operating conditions or frequently changing loads such as startup are likely larger. If the large loss rate measured for P2 is common during startup it could have important implications for the climate benefits of NGPPs. Peaking facilities that are designed for faster startups and more flexible loads may show different startup emissions.

Our EFs were used to estimate annual national CH_4 emissions from CC NGPPs with and without accounting for the large startup emissions. To account for startup emissions, we calculated the average duration of startup across the CC plants

DOI: 10.1021/acs.est.9b01875
Environ. Sci. Technol. 2019, 53, 8976−8984

Table 4. Calculated Emissions Data Based on the Average Stack $\Delta CH_4/\Delta CO_2$ Ratio and AMPD Data[a]

ID	date	AMPD CO_2 ER (Mg/h)	AMPD stack ER (kg CH_4/h)	stack EF (g/MMBTU)	throughput (kg CH_4/h)	loss rate (%)
P6	11/12/16	710 ± 100	−90 ± 180	−7 ± 13	230 000	−0.04 ± 0.08
P6	11/13/16	850 ± 120	51 ± 32	3.2 ± 2.0	275 000	0.018 ± 0.012
P6	11/19/16	970 ± 140	30 ± 110	1.9 ± 6.2	311 000	0.011 ± 0.035
P8	11/14/16	200 ± 30	17 ± 10	4.6 ± 2.8	64 000	0.026 ± 0.016
P8	11/17/16	240 ± 30	30 ± 26	6.6 ± 5.7	78 000	0.038 ± 0.033
P4	6/14/17	170 ± 20	−0.5 ± 4	−0.2 ± 1.2	54 000	−0.0009 ± 0.0067
P4	6/21/17	180 ± 20	NA	23.6 ± 8.4[b]	57 000	0.136 ± 0.048[b]
P4	7/24/17	180 ± 20	117 ± 31	35.5 ± 9.3	57 000	0.204 ± 0.054
P3	5/18/17	420 ± 60	43 ± 30	5.5 ± 3.9	136 000	0.031 ± 0.022
P3	7/7/17	440 ± 60	41 ± 43	5.0 ± 5.2	143 000	0.029 ± 0.030
P3	7/24/17	430 ± 60	63 ± 63	7.8 ± 7.9	138 000	0.045 ± 0.045
P2	10/13/17	62 ± 9	510 + 760/−510	440 + 660/−440	20 000	2.5 + 3.8/−2.5

[a]Uncertainties represent 1σ based largely on the propagated uncertainty of the stack ratios. AMPD uncertainties are 14% based on the calculation discussed by Peischl et al.[19] All data shown other than for 6/21 is unrelated to the MBE ER data and as such unaffected by any potential bias in the MBE method. [b]No stack data was collected for this flight, so the MBE ER was used as the numerator in eqs 4 and 5 instead. Propagated uncertainties include the MBE uncertainty instead of the variability of stack samples throughout the day for this flight.

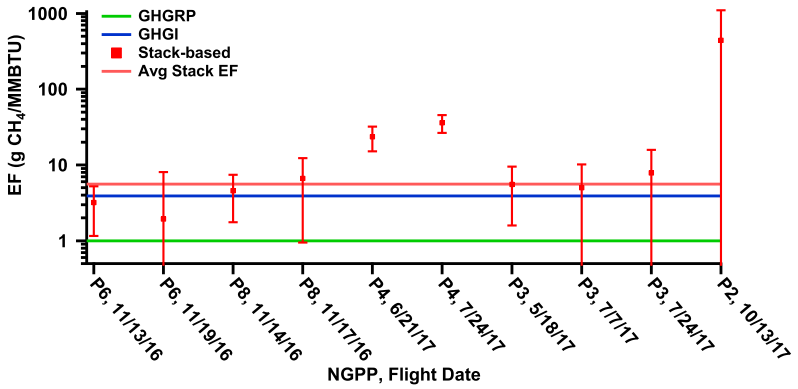

Figure 7. Log plot of EFs calculated from stack data from each flight. 1σ uncertainties are based on the variability across all stack samples that flight. The GHGRP and GHGI EFs of 1 g/MMBTU and 3.9 g/MMBTU respectively are shown for comparison. The average EF includes all CC stack data except for P2, regardless of downwind CH_4 emissions. Uncertainty bounds that are near or <0 are not shown. The measured EFs and the EPA EFs for most flights are statistically indistinguishable, with most EFs lying closer to the GHGI value, compared to the GHGRP value.

studied (4 h) and use this to calculate the heat input consumed during startup for all CC facilities in 2017 (3.519%, calculations detailed in the SI). P2's EF was then applied to 3.519% of 2017 CC heat input[23] and the average stack EF of 5.4 (+10/−5.4) g/MMBTU was applied to the remainder. When incorporating startup emissions like this, we calculate 170 (+200/−170) Gg CH_4 emitted as uncombusted CH_4 compared to 44 (+81/−44) Gg without accounting for startup (calculations detailed in SI). On the basis of $3.52/thousand ft^3 of NG,[47] these emissions are equivalent to 9 (+16/−9) million dollars of CH_4 lost or 33 (+40/−33) million dollars if including startup losses (calculations detailed in SI). For comparison, CC NGPPs purchased 29.0 billion dollars' worth of NG CH_4 in 2017 (calculation provided in the SI). The U.S. GHGI estimates 2016 CH_4 emissions from NG systems as 6.54 Tg. Therefore, emissions from NGPPs contribute in the range of 0.7−2.6% to the total CH_4 emissions from NG systems, depending strongly on the impact of startup conditions.

End users of NG, such as NGPPs, have been poorly studied and our work suggests that they could play a meaningful role in supply chain CH_4 emissions, particularly if the measured startup emissions are common. Although highly variable, startup emissions were up to several orders of magnitude larger than continuous operation emissions and warrant further study. Future work should also further investigate peaking NGPPs as they have more variable loads and startup more often but also more quickly. Additionally, shutdown emissions were not observed in this work but may show high emissions similar to startup given shutdown also involves quickly changing, low loads. Airborne measurements provided a useful snapshot of emissions in this work but continuous measurement systems like CEMS, given the variability seen, would likely prove more informative in the future. As such, cooperation with facilities is vital. Further improving our understanding of NGPP emissions will help fill a gap in the understanding of supply chain losses and could lead to changes in utility operations to minimize startup emissions.

■ ASSOCIATED CONTENT

Supporting Information

The Supporting Information is available free of charge on the ACS Publications website at DOI: 10.1021/acs.est.9b01875.

Qualitative plot of large CH_4 and C_2H_6 observed from P2, a comparison of P2 stack data to pipeline data, a detailed description of the C_2H_6 analyzer, a plot of a typical flight

DOI: 10.1021/acs.est.9b01875
Environ. Sci. Technol. 2019, 53, 8976−8984

path, a description of an off-lake breeze seen on the 10/13/17 flight at P2, a discussion of the LOD approach used to calculate stack ratios for flights without CH_4 in the stacks, a detailed discussion of the uncertainty calculation for MBE results, and detailed discussions of the calculations for stack emission ratios, national annual emissions with different GWPs, national annual emissions based on measurements, and the cost of national annual emissions (PDF)

AUTHOR INFORMATION

Corresponding Author

*Phone: (765) 496-2404. Fax: (765) 494-0239. E-mail: paul.shepson@stonybrook.edu.

ORCID

Kristian D. Hajny: 0000-0003-3249-7157

Stephen Conley: 0000-0001-6753-8962

Present Address

¶O.E.S.: Lake Michigan Air Directors Consortium, 101 S. Webster St., Madison, WI 53703.

Author Contributions

The manuscript was written through contributions of all authors. All authors have given approval to the final version of the manuscript.

Notes

The authors declare no competing financial interest.

ACKNOWLEDGMENTS

This work was funded by the Environmental Defense Fund (EDF). Funding for EDF's methane research series, including this work, is provided by the Alfred P. Sloan Foundation, and the Brunckhorst Foundation. The authors would like to thank air traffic control in the various cities for their support with our flight patterns and the Jonathan Amy Facility for Chemical Instrumentation at Purdue University for continued assistance in maintaining equipment in ALAR.

ABBREVIATIONS

NGPP, natural gas-fired power plant; CH_4, methane; CO_2, carbon dioxide; ER, emission rate; EF, emission factor; EPA, Environmental Protection Agency; GHGI, greenhouse gas inventory; GHGRP, greenhouse gas reporting program; GHG, greenhouse gas; GWP, global warming potential; SI, Supporting Information; CC, combined cycle; MBE, mass balance experiment; AMPD, air markets program data; CEMS, continuous emissions monitoring systems; MMBTU, million British thermal units; IPCC, Intergovernmental Panel on Climate Change; C_2H_6, ethane; ALAR, Airborne Laboratory for Atmospheric Research; NG, natural gas

REFERENCES

(1) U.S. EIA. Review of Emerging Resources: U.S. Shale Gas and Shale Oil Plays. https://www.eia.gov/analysis/studies/usshalegas/ (accessed May 6, 2018).

(2) Howarth, R. W. A Bridge to Nowhere: Methane Emissions and the Greenhouse Gas Footprint of Natural Gas. *Energy Sci. Eng.* **2014**, *2* (2), 47−60 https://doi.org/10.1002/ese3.35. .

(3) U.S. EIA. Electricity Data Browser—Net Generation for Electric Power. https://www.eia.gov/electricity/data/browser/#/topic/0?agg=2,0,1&fuel=9&geo=g&sec=008&linechart=ELEC.GEN.COW-US-98.A~ELEC.GEN.NG-US-98.A&columnchart=ELEC.GEN.COW-US-98.A&map=ELEC.GEN.COW-US-98.A&freq=A&ctype=linechart&ltype=pin&rtype=s&maptype=0&rse=0&pin= (accessed May 10, 2019).

(4) U.S. EIA. Carbon Dioxide Emissions Coefficients by Fuel. https://www.eia.gov/environment/emissions/co2_vol_mass.php (accessed May 6, 2018).

(5) U.S. EPA. GHGRP Yearly Overview. https://www.epa.gov/ghgreporting/ghgrp-yearly-overview (accessed Apr 16, 2018).

(6) *Climate Change 2013: The Physical Science Basis. Contribution of Working Group I to the Fifth Assessment Report of the Intergovernmental Panel on Climate Change*; Stocker, T. F., Qin, D., Plattner, G. K., Tignor, M., Allen, S. K., Boschung, J., Nauels, A., Xia, Y., Bex, V., Midgley, P. M., Eds.; IPCC, Cambridge University Press: Cambridge, United Kingdom, 2013.

(7) U.S. EPA. Overview of Greenhouse Gases. https://www.epa.gov/ghgemissions/overview-greenhouse-gases (accessed May 20, 2018).

(8) Alvarez, R. A.; Zavala-Araiza, D.; Lyon, D. R.; Allen, D. T.; Barkley, Z. R.; Brandt, A. R.; Davis, K. J.; Herndon, S. C.; Jacob, D. J.; Karion, A.; Kort, E. A.; Lamb, B. K.; Lauvaux, T.; Maasakkers, J. D.; Marchese, A. J.; Omara, M.; Pacala, S. W.; Peischl, J.; Robinson, A. L.; Shepson, P. B.; Sweeney, C.; Townsend-Small, A.; Wofsy, S. C.; Hamburg, S. P. Assessment of Methane Emissions from the U.S. Oil and Gas Supply Chain. *Science* **2018**, eaar7204.

(9) Brandt, A. R.; Heath, G. A.; Kort, E. A.; O'Sullivan, F.; Pétron, G.; Jordaan, S. M.; Tans, P.; Wilcox, J.; Gopstein, A. M.; Arent, D.; Wofsy, S.; Brown, N. J.; Bradley, R.; Stucky, G. D.; Eardley, D.; Harriss, R. Methane Leaks from North American Natural Gas Systems. *Science* **2014**, *343* (6172), 733−735.

(10) Alvarez, R. A.; Pacala, S. W.; Winebrake, J. J.; Chameides, W. L.; Hamburg, S. P. Greater Focus Needed on Methane Leakage from Natural Gas Infrastructure. *Proc. Natl. Acad. Sci. U. S. A.* **2012**, *109* (17), 6435−6440.

(11) Lavoie, T. N.; Shepson, P. B.; Cambaliza, M. O. L.; Stirm, B. H.; Karion, A.; Sweeney, C.; Yacovitch, T. I.; Herndon, S. C.; Lan, X.; Lyon, D. Aircraft-Based Measurements of Point Source Methane Emissions in the Barnett Shale Basin. *Environ. Sci. Technol.* **2015**, *49* (13), 7904−7913.

(12) Mehrotra, S.; Faloona, I.; Suard, M.; Conley, S.; Fischer, M. L. Airborne Methane Emission Measurements for Selected Oil and Gas Facilities Across California. *Environ. Sci. Technol.* **2017**, *51* (21), 12981−12987.

(13) Karion, A.; Sweeney, C.; Kort, E. A.; Shepson, P. B.; Brewer, A.; Cambaliza, M.; Conley, S. A.; Davis, K.; Deng, A.; Hardesty, M.; Herndon, S. C.; Lauvaux, T.; Lavoie, T.; Lyon, D.; Newberger, T.; Pétron, G.; Rella, C.; Smith, M.; Wolter, S.; Yacovitch, T. I.; Tans, P. Aircraft-Based Estimate of Total Methane Emissions from the Barnett Shale Region. *Environ. Sci. Technol.* **2015**, *49* (13), 8124−8131.

(14) Lamb, B. K.; Cambaliza, M. O. L.; Davis, K. J.; Edburg, S. L.; Ferrara, T. W.; Floerchinger, C.; Heimburger, A. M. F.; Herndon, S.; Lauvaux, T.; Lavoie, T.; Lyon, D. R.; Miles, N.; Prasad, K. R.; Richardson, S.; Roscioli, J. R.; Salmon, O. E.; Shepson, P. B.; Stirm, B. H.; Whetstone, J. Direct and Indirect Measurements and Modeling of Methane Emissions in Indianapolis, Indiana. *Environ. Sci. Technol.* **2016**, *50* (16), 8910−8917.

(15) Schwietzke, S.; Pétron, G.; Conley, S.; Pickering, C.; Mielke-Maday, I.; Dlugokencky, E. J.; Tans, P. P.; Vaughn, T.; Bell, C.; Zimmerle, D.; Wolter, S.; King, C. W.; White, A. B.; Coleman, T.; Bianco, L.; Schnell, R. C. Improved Mechanistic Understanding of Natural Gas Methane Emissions from Spatially Resolved Aircraft Measurements. *Environ. Sci. Technol.* **2017**, *51* (12), 7286−7294.

(16) Zavala-Araiza, D.; Alvarez, R. A.; Lyon, D. R.; Allen, D. T.; Marchese, A. J.; Zimmerle, D. J.; Hamburg, S. P. Super-Emitters in Natural Gas Infrastructure Are Caused by Abnormal Process Conditions. *Nat. Commun.* **2017**, *8*, 14012.

(17) Lavoie, T. N.; Shepson, P. B.; Gore, C. A.; Stirm, B. H.; Kaeser, R.; Wulle, B.; Lyon, D.; Rudek, J. Assessing the Methane Emissions from Natural Gas-Fired Power Plants and Oil Refineries. *Environ. Sci. Technol.* **2017**, *51* (6), 3373−3381.

(18) Lyon, D. R.; Alvarez, R. A.; Zavala-Araiza, D.; Brandt, A. R.; Jackson, R. B.; Hamburg, S. P. Aerial Surveys of Elevated Hydrocarbon

DOI: 10.1021/acs.est.9b01875
Environ. Sci. Technol. 2019, 53, 8976−8984

Emissions from Oil and Gas Production Sites. *Environ. Sci. Technol.* **2016**, *50* (9), 4877−4886.
(19) Peischl, J.; Ryerson, T. B.; Holloway, J. S.; Parrish, D. D.; Trainer, M.; Frost, G. J.; Aikin, K. C.; Brown, S. S.; Dubé, W. P.; Stark, H.; Fehsenfeld, F. C. A Top-down Analysis of Emissions from Selected Texas Power Plants during TexAQS 2000 and 2006. *J. Geophys. Res.* **2010**, *115* (D16), D16303.
(20) Fischer, M. L.; Chan, W. R.; Delp, W.; Jeong, S.; Rapp, V. H.; Zhu, Z. An Estimate of Natural Gas Methane Emissions from California Homes. *Environ. Sci. Technol.* **2018**, *52*, 10205.
(21) Balcombe, P.; Anderson, K.; Speirs, J.; Brandon, N.; Hawkes, A. The Natural Gas Supply Chain: The Importance of Methane and Carbon Dioxide Emissions. *ACS Sustainable Chem. Eng.* **2017**, *5* (1), 3−20.
(22) U.S. EIA. Form EIA-860, Annual Electric Generator Report. https://www.eia.gov/electricity/annual/html/epa_08_02.html (accessed May 20, 2018).
(23) U.S. EPA. Air Markets Program Data https://ampd.epa.gov/ampd/ (accessed Apr 15, 2018).
(24) Code of Federal Regulations Title 40—Protection of Environment. https://www.gpo.gov/fdsys/pkg/CFR-2017-title40-vol23/xml/CFR-2017-title40-vol23-part98-subpartC.xml (accessed May 6, 2018).
(25) U.S. EPA. Facility Level Information on Greenhouse Gases Tool. http://ghgdata.epa.gov/ghgp/main.do (accessed Apr 15, 2018).
(26) Vol. 2: Energy. In *2006 IPCC Guidelines for National Greenhouse Gas Inventories*; Eggelston, S., Leandro, B., Miwa, K., Ngara, T., Tanabe, K., Eds.; Institute for Global Environmental Strategies for the IPCC, 2006; p 2.16.
(27) Vol. 2: Energy. In *2006 IPCC Guidelines for National Greenhouse Gas Inventories*; Eggelston, S., Leandro, B., Miwa, K., Ngara, T., Tanabe, K., Eds.; Institute for Global Environmental Strategies for the IPCC, 2006; p 2.25.
(28) U.S. EPA. Inventory of U.S. Greenhouse Gas Emissions and Sinks: 1990−2016. https://www.epa.gov/ghgemissions/inventory-us-greenhouse-gas-emissions-and-sinks-1990-2016 (accessed Apr 16, 2018).
(29) U.S. EPA. Chapter 3: Stationary Internal Combustion Sources. In *Compilation of Air Pollutant Emissions Factors, AP 42*; U.S. EPA, 1995; Vol. *1*, p 11.
(30) Hajny, K.; Shepson, P.; Kaeser, R.; Stirm, B.; Stuff, A.; Wulle, B.; Rudek, J.; Lyon, D. Assessing the Accuracy and Precision of the Airborne Mass Balance Technique. Manuscript in Preparation, 2019.
(31) Cambaliza, M. O. L.; Shepson, P. B.; Caulton, D. R.; Stirm, B.; Samarov, D.; Gurney, K. R.; Turnbull, J.; Davis, K. J.; Possolo, A.; Karion, A.; Sweeney, C.; Moser, B.; Hendricks, A.; Lauvaux, T.; Mays, K.; Whetstone, J.; Huang, J.; Razlivanov, I.; Miles, N. L.; Richardson, S. J. Assessment of Uncertainties of an Aircraft-Based Mass Balance Approach for Quantifying Urban Greenhouse Gas Emissions. *Atmos. Chem. Phys.* **2014**, *14* (17), 9029−9050.
(32) Cambaliza, M. O. L.; Shepson, P. B.; Bogner, J.; Caulton, D. R.; Stirm, B.; Sweeney, C.; Montzka, S. A.; Gurney, K. R.; Spokas, K.; Salmon, O. E.; Lavoie, T. N.; Hendricks, A.; Mays, K.; Turnbull, J.; Miller, B. R.; Lauvaux, T.; Davis, K.; Karion, A.; Moser, B.; Miller, C.; Obermeyer, C.; Whetstone, J.; Prasad, K.; Miles, N.; Richardson, S. Quantification and Source Apportionment of the Methane Emission Flux from the City of Indianapolis. *Elem Sci. Anth* **2015**, *3*, 000037.
(33) Caulton, D. R.; Shepson, P. B.; Santoro, R. L.; Sparks, J. P.; Howarth, R. W.; Ingraffea, A. R.; Cambaliza, M. O. L.; Sweeney, C.; Karion, A.; Davis, K. J.; Stirm, B. H.; Montzka, S. A.; Miller, B. R. Toward a Better Understanding and Quantification of Methane Emissions from Shale Gas Development. *Proc. Natl. Acad. Sci. U. S. A.* **2014**, *111* (17), 6237−6242.
(34) Mays, K. L.; Shepson, P. B.; Stirm, B. H.; Karion, A.; Sweeney, C.; Gurney, K. R. Aircraft-Based Measurements of the Carbon Footprint of Indianapolis. *Environ. Sci. Technol.* **2009**, *43* (20), 7816−7823.
(35) Garman, K. E.; Hill, K. A.; Wyss, P.; Carlsen, M.; Zimmerman, J. R.; Stirm, B. H.; Carney, T. Q.; Santini, R.; Shepson, P. B. An Airborne and Wind Tunnel Evaluation of a Wind Turbulence Measurement System for Aircraft-Based Flux Measurements. *J. Atmospheric Ocean. Technol.* **2006**, *23* (12), 1696−1708.
(36) Crosson, E. R. A Cavity Ring-down Analyzer for Measuring Atmospheric Levels of Methane, Carbon Dioxide, and Water Vapor. *Appl. Phys. B: Lasers Opt.* **2008**, *92* (3), 403−408.
(37) U.S. EIA. Form EIA-860, Annual Electric Generator Report. https://www.eia.gov/electricity/annual/html/epa_04_03.html (accessed May 6, 2018).
(38) Heimburger, A. M. F.; Harvey, R. M.; Shepson, P. B.; Stirm, B. H.; Gore, C.; Turnbull, J.; Cambaliza, M. O. L.; Salmon, O. E.; Kerlo, A.-E. M.; Lavoie, T. N.; Davis, K. J.; Lauvaux, T.; Karion, A.; Sweeney, C.; Brewer, W. A.; Hardesty, R. M.; Gurney, K. R. Assessing the Optimized Precision of the Aircraft Mass Balance Method for Measurement of Urban Greenhouse Gas Emission Rates through Averaging. *Elem Sci. Anth* **2017**, *5* (0), 26.
(39) Chu, D. The GLOBEC Kriging Software Package—EasyKrig3. http://globec.whoi.edu/software/kriging/easy_krig/easy_krig.html (accessed Aug 16, 2018).
(40) Conley, S.; Faloona, I.; Mehrotra, S.; Suard, M.; Lenschow, D. H.; Sweeney, C.; Herndon, S.; Schwietzke, S.; Pétron, G.; Pifer, J.; Kort, E. A.; Schnell, R. Application of Gauss's Theorem to Quantify Localized Surface Emissions from Airborne Measurements of Wind and Trace Gases. *Atmospheric Meas. Technol. Discuss.* **2017**, 1−29.
(41) Caulton, D. R.; Shepson, P. B.; Cambaliza, M. O. L.; McCabe, D.; Baum, E.; Stirm, B. H. Methane Destruction Efficiency of Natural Gas Flares Associated with Shale Formation Wells. *Environ. Sci. Technol.* **2014**, *48* (16), 9548−9554.
(42) Gvakharia, A.; Kort, E. A.; Brandt, A.; Peischl, J.; Ryerson, T. B.; Schwarz, J. P.; Smith, M. L.; Sweeney, C. Methane, Black Carbon, and Ethane Emissions from Natural Gas Flares in the Bakken Shale, North Dakota. *Environ. Sci. Technol.* **2017**, *51* (9), 5317−5325.
(43) U.S. EIA. What are Ccf, Mcf, Btu, and therms? How do I convert natural gas prices in dollars per Ccf or Mcf to dollars per Btu or therm? https://www.eia.gov/tools/faqs/faq.php?id=45&t=8 (accessed Aug 20, 2018).
(44) U.S. EIA. Heat Content of Natural Gas Consumed by Electric Power Sector. https://www.eia.gov/dnav/ng/ng_cons_heat_a_EPG0_VEUH_btucf_a.htm (accessed Jun 10, 2019).
(45) IUPAC. Task Group on Atmospheric Chemical Kinetic Data Evaluation. http://iupac.pole-ether.fr/display_pressure_independent.php (accessed May 22, 2019).
(46) Wärstilä. Gas Turbine for Power Generation: Introduction. https://www.wartsila.com/energy/learning-center/technical-comparisons/gas-turbine-for-power-generation-introduction (accessed May 22, 2019).
(47) U.S. EIA. Natural Gas Prices. https://www.eia.gov/dnav/ng/ng_pri_sum_dcu_nus_a.htm (accessed Sep 18, 2018).

DOI: 10.1021/acs.est.9b01875
Environ. Sci. Technol. 2019, 53, 8976−8984